2020

Iron in Urban Air Pollution

Joseph R. Salazar

Iron in Urban Air Pollution

A Dissertation

Presented to

the Faculty of the College of Natural Sciences and Mathematics

University of Denver

In Partial Fulfillment

of the Requirements for the Degree

Doctor of Philosophy

by

Joseph R. Salazar

March 2020

Advisor: Brian Majestic

Author: Joseph R. Salazar
Title: Iron in Urban Air Pollution
Advisor: Brian Majestic
Degree Date: March 2020

Abstract

The processes by which iron is solubilized are largely unknown. There are three hypotheses on how iron is soluble: 1) iron is thought to undergo an acid based solubilization process, 2) iron undergoes an oxidation/reduction process and reduces iron(III) to the more soluble iron(II), and 3) iron is bound to organic molecules, which solubilizes it. The 3 hypotheses on iron water-solubilized are explored by presenting two individual studies.

The first study investigates iron directly from car exhaust. Exhaust particles were collected from 32 vehicles. Iron solubility in these samples ranged from 0%-82% with the average iron solubility being 30%. X-ray absorption near edge structure (XANES) spectroscopy showed that Fe(III) was the primary oxidation state of iron. Water-soluble iron was not correlated to sulfates, which are frequently found in aerosols as an acidic species. Last, correlation of iron was explored with respect to intermediate volatility organic compounds (IVOCs) and naphthalene and resulting R^2 as high as 0.56. A bench top study verified the results by showing an increasing water-solubility iron by a factor of 5.5. Thus, a hypothesis was developed that, during the extraction process, the organic components of the PM become oxidized and chelate the iron into water.

The observation from the car exhaust led to the investigation of PM and iron in the ambient atmosphere known as the Platte River Air Pollution and Photochemistry

Experiment (PRAPPE). The samples from PRAPPE were collected for a 24-hour period during summer (August 2017) and winter (December 2016 - March 2017). Here we compared $PM_{2.5}$ from 3 different sites including Denver (an urban), Jackson Lake State Park (a rural), and Platteville (a mixed site). The speciation of the iron component of the PM was also investigated. It was found the almandine ($Fe_3Al_2Si_3O_{12}$) was the most abundant iron complex follow by magnetite (Fe_3O_4) then Fe(III)dextran. Last, no correlation to iron oxidation and iron solubility was found.

The two studies showed that water-soluble iron is not correlated to sulfates. Iron oxidation state was not a factor in the resulting water-soluble Iron. Iron water-solubility was a result of iron organic interaction.

Acknowledgements

The Author would like to acknowledge Brain Majestic for his amazing support and guidance though his PhD processes. The author also would like to thank University of Colorado's engineering department for the collaboration on the PRAPPE project: David Pfotenhauer and Frank Leresche for the amazing advice, collaboration, sample collection and expertise though the years, Fernando Rosario-Ortiz and Michael Hannigan for their great leadership and mentorship during the PRAPPE project, the California Air Resource Board (CARB) for the use of the facility for exhaust sample collection, Greg Drozd and Benton Cartledge for sample collection at CARB, Greg Drozd for the organic speciation and his guidance on the vehicle exhaust project, Allen Robinson and Allen Goldstein for the help and support on the vehicle exhaust analysis and publication, John Haynes for the bench top studies with naphthalene and iron, Sirine Fakra for the guidance and instruction of XANES works, Rachel York-Marini for the help with XANES data collection and data work-up, and finally, all the graduate researchers John Haynes, Rachel York-Marini, Heather Runberg, Benton Cartledge and Nitika Dewan and the undergraduate research assistance Mooji Boldbaatar and Elise Palombella for their help with the everyday lab work. Last to all my previous teachers, mentors friends and family for all the wonderful support given.

Table of Contents

List of Figures

List of Abbreviations and Common Terms

PM: particulate matter

$PM_{2.5}$: particulate matter with aerodynamic diameter less than 2.5 μm

PM_{10}: particulate matter with aerodynamic diameter less than 2.5 μm

XANES: x-ray absorption near edge structure

ROS: reactive oxygen species

XRF: x-ray fluorescence

ICP-MS: inductively coupled plasma mass spectrometry

EC: elemental carbon

OC: organic carbon

SRA: single ring aromatic

IVOC: intermediate volatility organic compounds

SVOC: secondary volatility organic compounds

UC: Unified California

CVS: constant volume sample

PAHs: polycyclic aromatic hydrocarbons

HPLC: high performance liquid chromptogaphy

LCF: Least-square linear combination fitting

SRM: standard reference material

Chapter One: Iron and Particulate Matter

1.1 Particulate Matter

Particulate matter (PM) describes solid or liquid particles that exist in the atmosphere. These particles typically range from 0.001 to 100 µm. PM is classified by ultrafine particles, $PM_{2.5}$, coarse particles, and PM_{10}. Ultrafine particles are particles whose aerodynamic diameter (AD) is smaller than 0.1 µm. $PM_{2.5,}$ or fine particles, are particles with an AD of less than 2.5 µm. Coarse particles are particles with AD greater than 2.5 micrometers. PM_{10} particles have an AD less than 10 micrometers.

1.1.1 PM Composition

PM is largely constructed of elemental carbon, organic carbon, sulfates, nitrates, crustal materials, or metals (Vedal et al., 2009). PM composition can vary by source and city. In Denver, $PM_{2.5}$ composition is largely composed of organic carbon followed by sulfates and nitrates then elemental carbon and the smallest is composed of metals (Figure 2.1). $PM_{2.5}$ can very slightly from region and season but the typical trend is $PM_{2.5}$ is composition is dominated by organic carbon, sulfates and nitrates (Figure 1.2) (Bell et al., 2007).

The present study will focus on the trace metals components of PM contained in $PM_{2.5}$ with most of the emphasis on iron. Iron is the most abundant transition metal in the atmosphere and undergoes a unique chemical reaction called Fenton chemistry.

1.1.2 Sources of PM

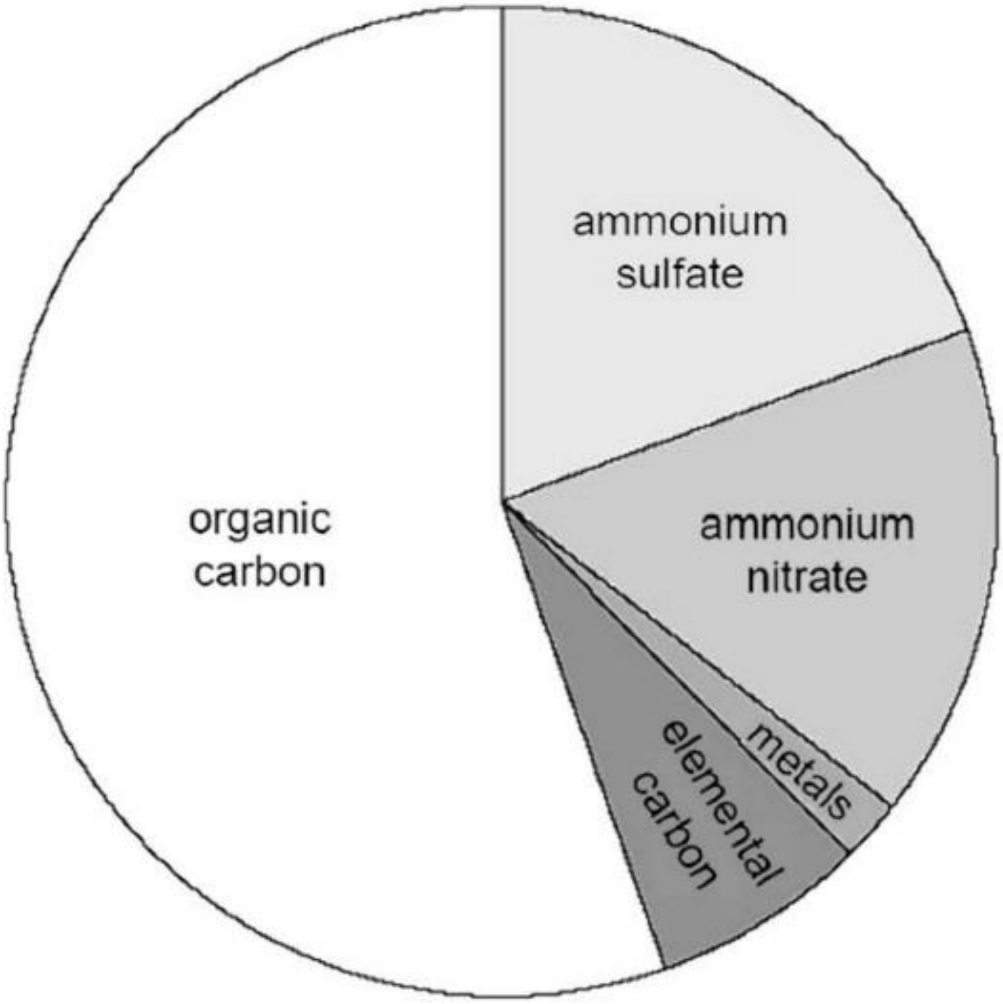

Figure 1.1: Average composition of $PM_{2.5}$ in Denver, Colorado (Vedal et al., 2009)

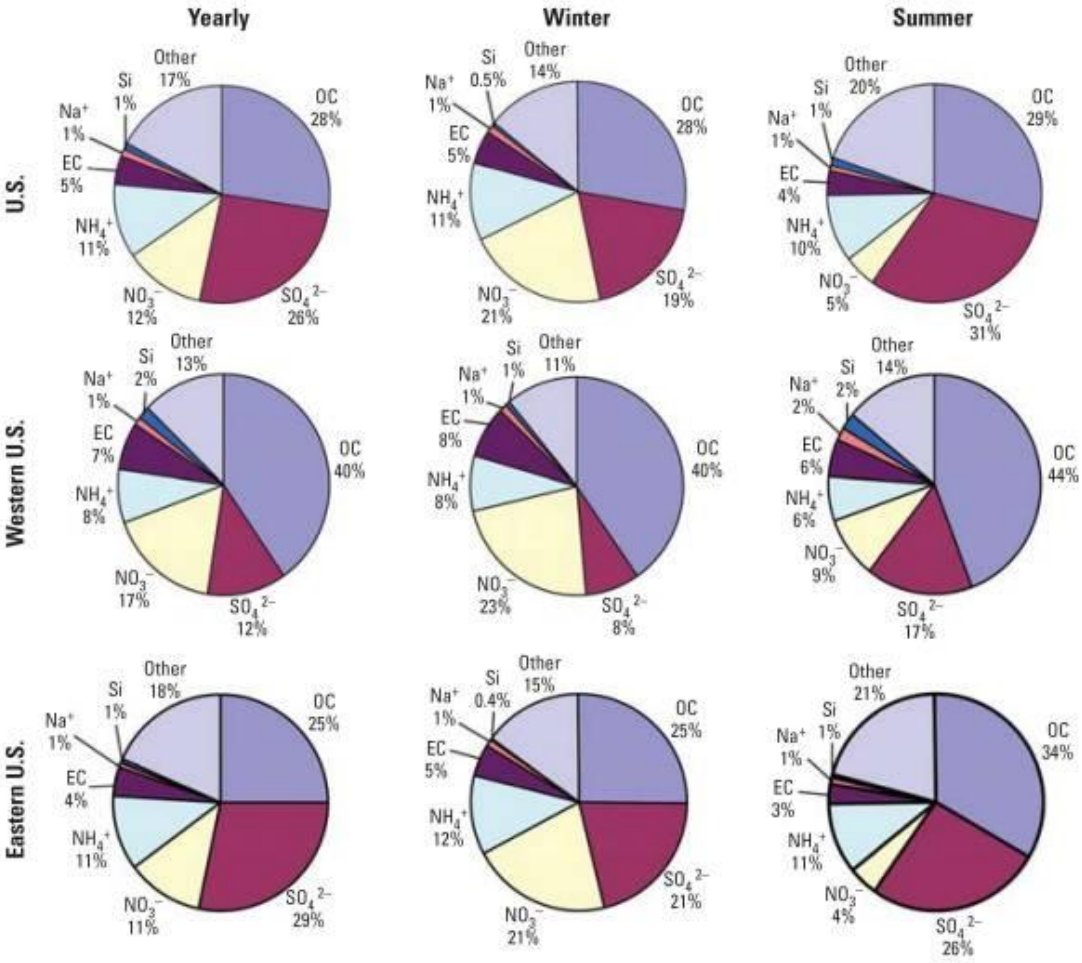

Figure 1.2: Composition of PM by region, season, and year (Bell et al., 2007)

$PM_{2.5}$ and ultrafine particles generally originate from combustion sources, while coarse particles are typically found from mechanical abrasions (Chow and Watson, 2002). Anthropogenic sources of coarse particles come from different kinds of construction abrasion. Examples of coarse, natural aerosols includes sea spray and windblown dust (Finlayson-Pitts and Pitts, 2000). Some natural sources of $PM_{2.5}$ includes resuspension of soil, wild fires, and volcanic eruptions (Xie et al., 2012). Anthropogenic sources of $PM_{2.5}$ differ from natural sources, as most anthropogenic $PM_{2.5}$ comes from combustion process including vehicle combustion, coal combustion, and biomass burning (Karagulian et al., 2015).

1.1.3 PM Effects on Health

PM has been shown to have strong adverse health effects (Hei, 2002; Iii et al., 2012; Landreman et al., 2008; Li et al., 2018). $PM_{2.5}$ enters deep into the lungs and is suspected to be the primary cause of various health complications (Kelly, 2003). Ongoing research has shown that these complications can range from minor inflammation to major neurological disorders and cardiovascular diseases (Fiordelisi et al., 2017; Fu et al., 2019; Hamad et al., 2016; Iii et al., 2012). However, the extent of these health effects can vary greatly and strongly depend on location (Hei, 2002; Lippmann et al., 2003). Insight into these health concerns led the Environmental Protection Agency (EPA) to create the National Ambient Air Quality Standards (NAAQS) for $PM_{2.5}$ in 1971 (Lippmann et al., 2003). Later, stronger correlations were made to mortality rates and $PM_{2.5}$ concentrations (Dockery et al., 1993). A more recent study, Denver Aerosol Sources and Health (DASH) study monitored and assessed the PM concentration in Denver's urban environment and

found a correlation between the increase in daily $PM_{2.5}$ and daily mortality rates (Kim et al., 2015), verifying the need to understand the chemistry of $PM_{2.5}$.

1.2 Iron (Fe)

Each year, 56.6 Tg of iron enters the atmosphere and impact health and environmental geochemical cycles (Luo et al., 2008); this makes iron the most abundant transition metal in the atmosphere. Iron contained in $PM_{2.5}$ can contribute to the health of communities and is a limiting reagent for phytoplankton. Iron is known to come from different sources that can be either crustal or anthropogenic. Depending on those sources, iron differs in oxidation state, solubility or speciation. Of these, the water-soluble iron has been suspected to be the cause of health effects resulting from radical oxidation species (ROS) production and assessable to phytoplankton as a limiting nutrient.

1.2.1 Sources of Iron

Biomass burning and/or combustion play a large role in the addition of soluble iron into the environment (Luo et al., 2008). Many sources are known to input iron into the atmosphere from combustion products including wildfires, motor vehicles, smelting plants, cook stove burning, and trash burning. Of these, motor vehicles are of interest because they are a major contributor to the release of combustion PM in the atmosphere in urban environments (Chuang et al., 2005; Luo et al., 2008; Sholkovitz et al., 2009). In 2018, 9.32 million barrels of gas per day were burned in the USA, thereby releasing PM containing water-soluble iron into the atmosphere (US Energy Information Administration). The water-soluble iron contained in PM may result from the breakdown of vehicle steel, motor oil, and trace concentrations already present in the fuel (Lawrence

et al., 2013; Liati et al., 2015; Santos et al., 2011). Chapter 2 of this dissertation will explore the water-soluble iron concentration contained in vehicle exhaust.

1.2.2 Iron Oxidation States

Iron is found in PM with 3 different oxidation states Fe(II) ,Fe(III) and Fe(0). while Fe(0) has been observed, it is the least common of the three oxidation states. Each of these oxidation states can have unique reactions. Fe(0) is known to be the largest producer of ROS, and Fe(II) is the second major producer out of the three different iron oxidation states (Auffan et al., 2008). Fe(II) is the most water-soluble of all the iron oxidation states, thereby allowing it to be more readily available for reactions in cloud-droplets, for phytoplankton, and allowing it to enter lung fluid. Fe(III) is the most common form of iron in the atmosphere (Hta et al., 2006; Oakes et al., 2012a). Fe(III), by itself, is insoluble in water, but can react with sunlight to reduce and form Fe(II) (Rubio-Clemente et al., 2014). Oxidation states do not provide sufficient information to fully explain iron chemistry in the atmosphere, therefore it is important to examine iron complexation and other metrics.

1.2.3 Identification of Iron Complexes

Iron is found in many different crustal complexes. Iron-aluminum-silicates is the most common form of iron found in $PM_{2.5}$ and PM_{10} samples, but is also found as iron oxides and iron-organic complexes (Petroselli et al., 2018). The majority of iron particles are from crustal sources, mostly windblown dust. There are multiple forms of iron oxide found in PM. The most common iron oxides are magnetite (Fe_3O_4) and hematite (Fe_2O_3); these have been shown to be either anthropogenic or crustal. Magnetite is a mixed

oxidation state iron oxide and has been shown to result from diesel exhaust (Abdul-Razzaq and Gautam, 2001). Hematite is an Fe(III) oxide and results from natural iron found in rock formations. Fe-organic complexes consist of iron bound to organic molecules. Oxalate compounds are commonly found and are suspected to chelate iron and water-solubilize it (Paris et al., 2011; Paris and Desboeufs, 2013). These organic-iron complexes are suspected to account for the water-soluble iron found in PM (Ito, 2015).

1.2.4 Resulting Health Effect Related to Iron

Water-soluble iron is strongly correlated with the resulting health effects of $PM_{2.5}$, which results from the water-soluble iron contained in the PM, thereby contributing to the production of ROS (Prahalad et al., 2001; See et al., 2007; Valavanidis et al., 2000). Oxidative stress is triggered by high levels of ROS. This is thought to be one cause of adverse health effects with aerosols. Oxidative stress can lead to oxidation of DNA cells and tissue (Kelly, 2003). This ROS production results in oxidative stress on the respiratory system, and appears to be one of the causes of health effects in $PM_{2.5}$.

1.2.5 Environmental Effects of Iron

Water-soluble iron has been shown to have a profound environmental effect. Water-soluble iron has shown to promote growth for phytoplankton in most of the Southern Ocean, equatorial regions of the Pacific Ocean, and subarctic regions of the Pacific Ocean (Coale et al., 1996; Division et al., 2013). Water-soluble iron in these regions is limited by the ligand concentration present in the ocean and is a limiting nutrient for phytoplankton growth (Figure 2). The inputs of water-soluble iron from windblown dust increases the availability of water-soluble iron and stimulates

phytoplankton growth. The increase in phytoplankton growth is shown experimentally where water-soluble iron was enriched in these oceans and developed large enough phytoplankton blooms to be seen from space (Tagliabue et al., 2017). Phytoplankton importance is involved in CO_2 uptake and nitrogen fixing (Jickells et al., 2005a). Models have shown this increase of phytoplankton growth resulting from increased inputs of iron could reduce CO_2 atmospheric concentration by 60-100 ppm (Tagliabue et al., 2017). This interaction between CO_2, nitrogen, and iron is essential to understanding the earth's oceans and atmospheric interactions.

1.3 Solubilization of Iron

PM contains a variety of chemical species which can water-solubilize iron. The iron collected in urban environments has a fractional solubility of 22-50%, contrasted with 0.2-1% found in crustal iron (Bonnet, 2004; Majestic et al., 2007; Petroselli et al., 2018; Sholkovitz et al., 2012). Currently, it is unclear which factors influence the water-solubility of iron in urban environments. There are three prevailing hypotheses on how iron is solubilized: 1) water-soluble iron developed from an interactions of organics and Fe from urban chemical species, 2) chemical reactions result in higher solubilized iron during dust transportation and 3) Iron undergoes a reduction processes from Fe(III) to Fe(II) and is water-solubilized (Cartledge et al., 2015; Ito, 2015).

1.3.1 Iron and Ligands

Ligand bound iron is known to aid in the solubility of iron. There are many organic ligands that are known and used to water-solubilize iron. Ethylenediaminetetraacetic acid

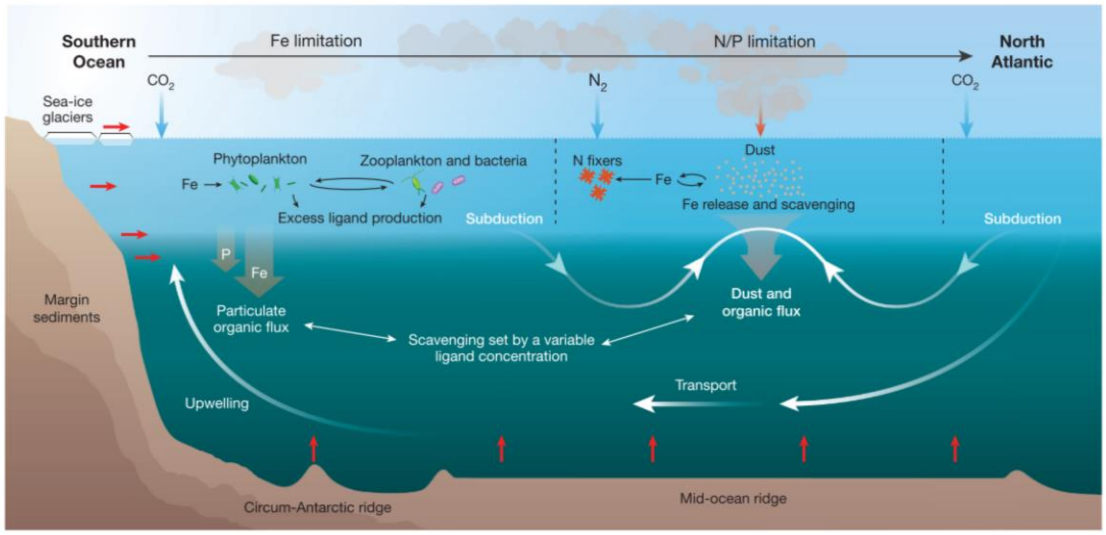

Figure 1.3: A diagram of major iron oceans processes in the Southern Ocean (Tagliabue et al., 2017).

(EDTA) is a common organic ligand with nitrogen and oxygen and is used to solubilize iron for plant nutrition. Siderophores are a class an organic molecules that water-solubilize iron for its own nutrition (Kraemer, 2004). Urban sources have multiple organic species that accompany iron. Oxalate is a common organic molecule that has been known to bind to iron and aid in its solubility. It has been shown that oxalate, malonate, tartrate, and humic acids can increase the water-solubility of iron by 0.05-22.40% depending on the organic concentration in a controlled lab (Batista and Nogueira, 2012; Paris et al., 2011; Paris and Desboeufs, 2013). Other humic-like substances (HULIS) are another mixture of organic molecules that has oxygen point charges which can also water-solubilize iron (Paris and Desboeufs, 2013).

1.3.2 Iron Redox Chemistry

As Fe-containing PM travels through the urban airsheds, it mixes with organic carbon and creates the possibility to undergo photochemistry. Organics that enter the atmosphere go through an oxidation process. During this oxidative event, Fe(III) is reduced to its more water-soluble Fe(II) oxidation state (Pehkonen et al., 1993). During lab procedures when iron is exposed to sunlight and organic substances, iron solubility can increase by 2 -15% (Haynes and Majestic, 2020). A possible reaction for this is photo-Fenton chemistry. In photo-Fenton reactions, Fe(III), water, and UV react to produce the more soluble Fe(II) and hydroxyl radicals (Equation 3).

1.3.3 Acid and Iron Chemistry

Acid mediated iron reduction is hypothesized to increase iron solubility. Iron is more soluble under more acidic conditions (Stumm and Morgan, 1996). As water-soluble

iron is commonly found in correlation with acidic species such as sulfates and nitrates, it is thought that iron could go through a process in which the Fe(III) is reduced to the more water-soluble Fe(II). During this process, acidic species condense onto an iron containing particle, decreasing the pH. This mechanism can result in a particle-pH less than 2 and could occur during atmospheric iron transport (Cwiertny et al., 2008). During transport, particles that contain nitrates and sulfates come into contact with cloud droplets. This process reduces the cloud pH and reacts with the iron in the particles. Then iron is reduced from Fe(III) to Fe(II) and becomes more soluble through this interaction (Oakes et al., 2012b). Currently, there are attempts to model and measure pH of particles in these environments.

1.4 Fenton Chemistry

One route of radical formation is iron in aqueous suspension via the photo-Fenton reaction. In Fenton chemistry, UV light reacts with Fe(III) to produce Fe(II) and hydroxyl radicals. In turn, the hydroxyl radicals oxidize organic compounds.

The mechanism to produce ROS is defined as going through a Fenton-like process. Fenton chemistry was originally explained by equation 1 (Kitis et al., 1999; Nidheesh and Gandhimathi, 2013).

$$Fe^{2+} + H_2O_2 \rightarrow FeOH^{2+} + \quad HO^{\cdot} \qquad \text{(Equation 1)}$$

k = 70 M^{-1} s^{-1} (Rigg et al., 1954)

This action step results in a strong radical oxidizer and then undergoes different propagation steps resulting in an array of oxidized organic products (Lundstedt et al.,

2006; Neyens and Baeyens, 2003a; Nidheesh and Gandhimathi, 2013; Pignatello et al., 2006). In the reporting of iron oxidation states, various studies have found iron in both Fe(II) and/or Fe(III) (Oakes et al., 2012a, 2012b). Fe(III) can produce ROS through a different mechanism and at a faster rate than Fe(II) (Equation 2) (Neyens and Baeyens, 2003a; Pignatello et al., 2006; Walling and Goosen, 1963).

$$Fe^{3+} + H_2O_2 \rightarrow Fe^{2+} + H^+ + HO_2^{\cdot} \quad \text{(Equation 2)}$$

k= 0.001 – 0.01 M^{-1} s^{-1} (Walling and Goosen, 1963)

These pathways are largely used to study the removal of non-ionic species in aqueous environments. This process can be expanded to a photolytic process called photo-Fenton chemistry. Iron produces OH radicals in a liquid solution when introduced to sunlight. Photo-Fenton chemistry results in a powerful oxidizer (Equation 3). The reaction starts with Fe(III) and water, and then with the addition of sunlight the water results in OH radical Fe(II) and a H^+.

$$Fe^{3+} + H_2O \xrightarrow{h\nu} Fe^{2+} + H^+ + \quad HO^{\cdot} \quad \text{(Equation 3)}$$

Photo-Fenton chemistry is known to happen quickly based off the ability to oxidize polycyclic aromatic hydrocarbons (PAHs) in under 5 minutes. (Engwall et al., 1999). Fenton and photo-Fenton chemistry are viable reactions that process organic molecules in the environment and leads to oxidative stress in the body.

1.5 Metals Analysis

In order to conduct experiments and understand iron in the atmosphere there are two types of measurements that are made. Quantification is the process of identifying how much iron is present in the samples. When quantifying iron in the atmosphere, it is typical to report the values as mass per volume of air. The two types of quantification methods are: X-ray fluorescence (XRF) and inductively coupled plasma mass spectrometry (ICP-MS). Iron can present in a variety of different oxidation states and chemical species. In order to speciate iron, X-ray absorption near edge structure (XANES) spectroscopy is used.

1.5.1 Methods of Quantification: X-ray fluorescence (XRF)

XRF is a non-destructive way to quantify metals in PM. The common practice in using XRF is to have a set of standards and are measured for fluorescence. The samples are measured and then compared against standards. From this method nanograms of iron in a sample can be found. While quantification can be done with XRF it is common to use XRF to find the fluorescence of multiple elements and compare the fluorescence ratio between elements. Last, is to use XRF as a quick scan to find elemental spots to target for XANES (Lough et al., 2005; Teixeira et al., 2007).

1.5.2 Methods of Quantification: Inductively Coupled Plasma Mass-Spectrometry

Inductively coupled plasma mass-spectrometry (ICP-MS) is the most sensitive way of quantifying metals. This is the method commonly used to measure iron in PM. One way to quantify metals, is that metals in PM need to be in solution. A digestion process is used to solubilize the elements into an aqueous liquid. The general process

involves a digestion method using concentrated acids and hydrogen peroxide. Then, the sample is put under pressure and exposed to microwave radiation to increase the temperature above the normal boiling point. Finally, the samples are diluted and metal standards are used to quantify metals in parts per billion (ppb) (Cartledge et al., 2015; Kulkarni et al., 2007).

1.5.3 Speciation of Iron: X-ray Absorption Near Edge Structure (XANES)

XANES spectroscopy is a method to identify the species and oxidation number in the solid state. XANES sends a high energy photon into the PM sample and results in the high energy photon ejecting a core shell electron. The ejection of the electron develops a hole in the atom and then outer shell electrons fall to the lower energy levels to occupy the hole. The fluorescence of the electrons falling to the lower energy levels are unique for the oxidation state of iron and the accompanying ligands. In order to identify the oxidation state and ligands, standards of different iron species are compared using a Least-square linear combination fit (LCF). This model uses multiple combinations of standards to best fit the unknown samples spectra. The results give the percentages of each standard that comprises the best fit model developed from the LCF. Therefore, identity of multiple iron species can be found from a single iron particle (Frahm, 1988; Marcus et al., 2008).

1.6 Iron Research

In subsequent chapters, Iron water-solubility is examined. Two experiments were conducted to analyzed iron water-solubility in different environments. The Frist study

examines multiple hypotheses on the iron water-solubilization from car exhaust. The second study compared water-soluble iron in three different environments.

Chapter 2:

Water-soluble iron emitted from vehicle exhaust is linked to primary speciated organic compounds

*As published in Atmosphere Chemistry and Physics (Salazar et al., 2020)

2.1 Abstract

Iron is the most abundant transition element in airborne PM, primarily existing as Fe(II) or Fe(III). Generally, the fraction of water-soluble iron is greater in urban areas compared to areas dominated by crustal emissions. To better understand the origin of water-soluble iron in urban areas, tail-pipe emission samples were collected from 32 vehicles with emission certifications of Tier 0, low emission vehicles (LEV I), tier two low emission vehicles (LEV II), ultralow emission vehicles (ULEV), superultra-low emission vehicles (SULEV), and partial-zero emission vehicles (PZEV). Components quantified included gases, inorganic ions, elemental carbon (EC), organic carbon (OC), total metals and water-soluble metals. Naphthalene and intermediate volatility organic compounds (IVOC) were quantified for a subset of vehicles. The IVOC quantified contained 12 to 18 carbons and were divided into three subgroups: aliphatic, single ring aromatic (SRA), and polar (material not classified as either aliphatic or SRA). Iron solubility in the tested vehicles ranged from 0 – 82% (average = 30%). X-ray absorption near edge structure (XANES) spectroscopy showed that Fe(III) was the primary

oxidation state in 14 of the 16 tested vehicles, confirming that the presence of Fe(II) was not the main driver of water-soluble Fe. Correlation of water-soluble iron to sulfate was insignificant, as was correlation to every chemical component, except to naphthalene and some C12- C18 IVOCs with R^2 values as high as 0.56. A controlled benchtop study confirmed that naphthalene, alone, increases iron solubility from soils by a factor of 5.5 and that oxidized naphthalene species are created in the extract solution. These results suggest that the large driver in water-soluble iron from primary vehicle tail-pipe emissions is related to the organic composition of the PM. We hypothesize that, during the extraction process, specific components of the organic fraction of the PM are oxidized and chelate the iron into water.

2.2 Introduction

Iron has been identified as a limiting nutrient for phytoplankton in approximately half of the world's oceans, with deposition from the atmosphere as the major source (Moore and Abbott, 2002; Sholkovitz et al., 2012). Phytoplankton is one of the controlling factors of fixed nitrogen in many parts of the oceans and, consequently, plays a major role in the ocean's biogeochemical cycles (Baker et al., 2006; Chen and Siefert, 2004; Kraemer, 2004; Shi et al., 2012; Tagliabue et al., 2017). Also, water-soluble iron fractions are linked to the creation of reactive oxygen species (ROS) in lung fluid and in environmental matrices through Fenton chemistry (Hamad et al., 2016). These ROS impart oxidative stress on the respiratory system, contributing to various health effects (Landreman et al., 2008; Park et al., 2006; Verma et al., 2014).

Annually, approximately 55 Tg of iron enters the atmosphere from crustal sources (Luo et al., 2008). Of this, 14-16 Tg are deposited into the ocean, impacting the marine life and influencing the ecosystems (Gao, 2003; Jickells et al., 2005a). Typically, airborne iron from crustal sources ranges from 0.05-2% water-soluble of the total iron (Bonnet, 2004; Sholkovitz et al., 2012). Relative water-soluble iron in urban environments is higher, ranging from 2-50% of the total (Majestic et al., 2007; Sedwick et al., 2007; Sholkovitz et al., 2012). It is sugessted that combustion sources including fossil fuel burning, incinerator use and biomass burning may be a large contributor to the water-soluble iron fraction, contributing 0.66-1.07 Tg a^{-1} of water-soluble iron and this iron has been correlated to anthropogenic sources (Chuang et al., 2005; Luo et al., 2008; Sholkovitz et al., 2009). From these combustion sources, it has been shown that the species of iron differed greatly and had an impact in iron solubility (Fu et al., 2012). Even though total iron emissions from combustion sources are small in comparison to crustal sources, the relative insolubility of crustal iron leads to the possibility that combustion sources contribute 20%-100% of water-soluble iron into the atmosphere (Luo et al., 2008; Sholkovitz et al., 2012).

Previous studies in tunnels and parking structures have reported iron ranging from five to approximately 3,500 ng m^{-3}, revealing that brake wear, tire wear, resuspended road dust, and tail pipe emissions can be important sources of trace elements (Kuang et al., 2017; Lawrence et al., 2013; Li and Xiang, 2013; Lough et al., 2005; Park et al., 2006; Verma et al., 2014). Iron is contained in many fuels which has pre-combusted concentrations ranging from 13-1000 µg L^{-1} (Lee and Von Lehmden, 1973; Santos et al.,

2011; Teixeira et al., 2007). Within the engine, computational models of combustion in engines suggest that iron emissions could also originate from the fuel injector nozzle inside the engine block (Liati et al., 2015).

There are many different factors that may contribute to water-soluble iron and, as a result, several different hypotheses have been developed relating to how iron is solubilized in ambient atmospheres. First, correlation of ambient iron to sulfates in ambient aerosols suggest the possibility of iron solubilization (Desboeufs et al., 1999; Hand et al., 2004; Mackie et al., 2005; Oakes et al., 2012b). However, laboratory studies investigating the heterogeneous chemistry of iron have not shown any change in iron water-solubility, speciation, or oxidation state upon exposure to gaseous SO_2 (Cartledge et al., 2015; Luo et al., 2005; Majestic et al., 2007; Oakes et al., 2012a). A second hypothesis is that particle-bound iron oxidation state may control iron water solubility. Thus far, the limited field studies have been unable to show that iron oxidation state is correlated to iron's resulting water solubility, as the majority of iron found in aerosol particles is in the less soluble Fe(III) oxidation state (Luo et al., 2005; Majestic et al., 2007; Oakes et al., 2012a). A third, broad, iron solubilization hypothesis emphasizes an iron-organic interaction (Baba et al., 2015; Vile et al., 1987). For example, a significant increase in water-soluble iron is observed in the presence of oxalate and formate in ambient aerosols and in cloud droplets (Paris et al., 2011; Zhu et al., 1993). Even when compared to sulfuric acid, oxalic acid results in a greater increase in iron solubility because of the organic iron interaction (Chen and Grassian, 2013). Other studies have suggested that the photolysis of polycyclic aromatic hydrocarbons leads to reduced iron,

which may result in greater iron water solubility (Faiola et al., 2011; Haynes and Majestic, 2020; Haynes et al., 2019; Pehkonen et al., 1993; Zhu et al., 1993). Vehicle exhaust contains many organic species including secondary organic aerosol (SOA) Single-ring aromatic compounds (C6-C9) polycyclic aromatic hydrocarbons PAHs, hopanes, steranes, alkanes, organic acids and intermediate volatility organic compound (IVOCs) which are longer chain organic species (Cheung et al., 2010; Zhao et al., 2016).

In this study, we explore all three hypotheses (bulk ions, iron oxidation state, and organic speciation) in relation to iron solubility. Specifically, we examine the water-soluble iron emitted from 32 light duty gasoline vehicles with certifications of Tier 0, low emission vehicle (LEV I), tier two low emission vehicles (LEV II), ultralow emission vehicles (ULEV), superultra-low emission vehicles (SULEV), and partial-zero emission vehicles (PZEV). The total and water-soluble trace elements are compared to the ions, gaseous compounds, and organic emissions from the same vehicle set. Additionally, we acquired data on the emitted iron oxidation states on the exhaust particles. From this data set, real tail-pipe emission samples were explored to discover how various components of automobile exhaust affect the water solubility of iron.

2.3 Materials and Methods

2.3.1 Sample Collection

Exhaust samples from 32 gasoline vehicles were collected at the California Air Resources Board (CARB) Haagen-Smit laboratory over a six-week period. Standard emission test results from this campaign have been reported previously (Saliba et al., 2017). A description of the dynamometer, emission dilution system, and instrumentation

used in the vehicle set up is provided elsewhere (May et al., 2014; Saliba et al., 2017). Briefly, each vehicle was tested on a dynamometer using the cold-start Unified California (UC) Drive Cycle or the hot start Modal Arterial Cycle 4. Emission samples were collected using a constant volume sampler from which a slipstream of dilute exhaust was drawn at a flow rate of 47 L min^{-1}. Particle phase emissions were collected using three sampling trains operated in parallel off of the end of the constant volume sample (CVS) dilution tunnel. Train 1 contained a Teflon filter (47 mm, Pall-Gelman, Teflo R2PJ047). Train 2 contained two quartz filters (47 mm, Pall-Gelman, Tissuquartz 2500 QAOUP) in series. Train 3 contained an acid-cleaned Teflon filter followed by a quartz filter (47 mm, Teflo, Pall Life Sciences, Ann Arbor, MI) and the flow rate was 0.5 L min-1 through each Tenax tube. The particulate exhaust emissions were then collected on the pre-cleaned Teflon filters. The Teflon filters were stored in a freezer until extraction and analysis was performed. Filter holders were maintained at 47°C during sampling as per the CFR86 protocol.

The vehicles were recruited from private citizens, rental car agencies, or part of the Air Resource Board fleet. The vehicles tested were categorized by model years (1990-2014), vehicle type (passenger car and light-duty trucks), engine technologies (GDI and PFI), emission certification standers (Tier1 to SULEV), make, and model. All vehicles were tested using the same commercial gasoline fuel which had a 10 % ethanol blend and a carbon fraction of 0.82 (Saliba et al., 2017).

Gases (CO, CO_2, CH_4, NO, and NO_2) and total hydrocarbons (THC) were collected into heated Tedlar bags by UC Drive Cycles. Analysis of CO and CO_2 was

measured by nondispersive infrared detectors (IRD-4000), CH_4 by gas chromatography, with detection by a flame ionization detector (FID), NO_x by chemiluminescence (CLD 4000) and THC by FID (Drozd et al., 2016; Saliba et al., 2017). The Teflon filter in Train 1 was analyzed by ion chromatography for water-soluble anions and cations and procedure for these data presented elsewhere (Hickox et al., 2000). Train 2 included two parallel sets of Tenax-TA sorbent tubes (Gerstel) downstream of the Teflon filter. The first set was 2 tubes connected in parallel. One of these tubes was used to collect emissions during the cold start phase of UC (the first five minutes, commonly referred to as bag 1). The other tube was used to sample emissions during the combined hot-running and hot start phases of the UC (bags 1 and 2). The second set of sorbent tubes was connecfiguerwted in series to collect emissions over the entire UC test. The Teflo filter in Train 3 was used for total and water-soluble trace element analysis and particle-bound iron oxidation state and is the focus of this study.

2.3.2 Materials Preparation

All vessel cleaning and analytical preparation for the trace elements was performed under a laminar flow hood with incoming air passing through a high efficiency particulate air (HEPA) filter. All water used was purified to 18.2 MΩ-cm (Milli-Q Thermo-Fisher Nanopore). Fifteen and 50 mL plastic centrifuge vials, Petri dishes (Fisher), Teflon forceps (Fisher), syringe (Fisher), nitro cellulose paper (Fisher), and syringe cases (Life Sciences Products) were prepped by an acid cleaning process. For the plastic centrifuge vials, Petri dishes, Teflon forceps, syringe, and syringe cases this involved 24-hour soaks in a 10% reagent grade nitric acid bath followed by 10% reagent

grade hydrochloric bath then a 3% trace metal grade nitric acid (Fisher) resting bath with MQ rinses before, after and between each step. The nitro cellulose paper was cleaned by soaking in 2% HCl for 24 hours then rinsing with MQ water. Then, 2% HCl and MQ water were pushed through the filter. Teflon beaker liners were cleaned by an acetone rinse, then an overnight bath of 100% high performance liquid chromatography (HPLC)-grade acetonitrile and a final overnight bath of 5% trace-metal grade nitric acid. 0.20 micron syringe filters (Whatman, Marlborough, MA) were prepared with 10% trace-metal grade hydrochloric acid, MQ water and 5% nitric acid rinse.

The 47 mm Teflon filters were cleaned by submerging them in 10% trace metal grade nitric acid and rinsing with MQ water. The filters were then stored in the acid cleaned Petri dishes and sealed with Teflon tape for storage.

2.3.3 Water-Soluble Metals Sample Preparations

Water-soluble elements were extracted for 2 hours from the Teflon filter on a shaker table in 10 mL of MQ water. The water extract was filtered with 2 µm pore size nitro cellulose filters. The Teflon filter and the nitro cellulose filters were saved for total metals digestion. The water-soluble element extract was acidified to 5% trace-metal grade nitric acid and 2.5% trace-metal grade hydrochloric acid to be analyzed by inductively coupled plasma mass spectrometry (ICP-MS, Agilent 7700).

2.3.4 Sample Preparation for Total Elemental Analysis

First ~3% (measured exactly) of the filters were cut and saved for X-ray absorption near edge structure (XANES) spectroscopy, then the water-soluble elements

were extracted and, lastly the polymethylpentene ring was removed from the Teflon filters. The Teflon and the nitro cellulose filters for each sample were placed together into a microwave digestion vessel. To each digestion vessel, 750 µL of concentrated trace metal grade nitric acid, 250 µL of concentrated trace grade hydrochloric acid, 100 µL of concentrated trace grade hydrofluoric acid, and 100 µL of 30% hydrogen peroxide was added. These samples were digested (Ethos EZ, Milestone Inc) according to the following a temperature program: 15-minute ramp to 200 °C, then held at 200 °C for 15 minutes, and a 60-minute cooling period.(Cartledge and Majestic, 2015a) The samples were cooled to room temperature for 1 hour and the solution was diluted to 15 mL with MQ water and analyzed via ICP-MS.

2.3.5 Elemental Analysis

Blank filters and standard reference materials (SRMs) were digested alongside the exhaust samples using the same digestion process described above. Three SRMs were used to address the recoveries of our digestion process: urban particulate matter (1648a, NIST), San Joaquin Soil (2709a, NIST), and Recycled Auto Catalyst (2556, NIST). The recoveries of the SRMs were between 80-120%. The elements analyzed included Na, Mg, Al, K, Ca, Ti, V, Cr, Mn, Fe, Co, Ni, Cu, Zn, As, Se, Rb, Sr, Mo, Rh, Pd, Ag, Cd, Sb, Cs, Ba, Ce, Pt, Pb, U. Indium (~1 ppb) was used as an internal standard and a He collision cell was used to remove isobaric interferences.

2.3.6 XANES Spectroscopy

X-ray absorption near-edge structure (XANES) and micro X-ray fluorescence (μXRF) data for 16 vehicle exhaust samples were collected at the Advanced Light Source Microprobe beamline (10.3.2), Lawrence Berkeley National Laboratory, Berkeley, CA (Marcus et al., 2004). To locate iron spots on the filters, a broad μXRF elemental map of each sample was acquired at 10 keV using 12 μm by 12 μm pixel size and 50 ms dwell time per pixel. μXRF spectra were simultaneously recorded on each pixel of the map. Iron oxidation state and iron-bearing phases were investigated using iron K-edge extended XANES. The spectra were recorded in fluorescence mode by continuously scanning the Si (111) monochromator (Quick XAS mode) from 7011 to 7415 eV. The data were calibrated using an iron foil with first derivative set at 7110.75 eV (Kraft et al., 1996). All data were recorded using a seven-element solid state Ge detector (Canberra, ON). The spectra were deadtime corrected, deglitched, calibrated, pre-edge background subtracted and post-edge normalized using a suite of LabVIEW custom programs available at the beamline (Marcus et al., 2008). To rapidly survey iron oxidation state, a valence scatter plot was generated from normalized XANES data using a custom Matlab code and a large database of iron standards (10.3.2 XAS database) (Marcus et al., 2008). Least-square linear combination fitting (LCF) was subsequently performed in the range 7090 to 7365 eV to confirm iron valence and further identify the major mineral groups present. The best fit was chosen based on 1) minimum normalized sum-square value ($NSS=100\times[\sum(\mu_{exp}-\mu_{fit})^2/\sum(\mu_{exp})^2]$), where the addition of a spectral component to the fit required a 10% or greater improvement in the NSS value, and 2) on the elements

detected in the μXRF spectrum recorded on each XANES spot. The uncertainty on the percentages of species present is estimated to be ±10%.

2.3.7 Organic Speciation

A subset (10) of the 32 samples were quantified for IVOC using electron impact ionization with methods similar to that of Zhao et al., except adapted for GCxGC methods (Zhao et al., 2015, 2016). IVOC material was classified into three categories: aliphatic, single ring aromatic (SRA), and polar (Drozd et al., 2019). Classification within these three classes of compounds was determined by differences in second dimension retention time (polarity space) and by mass spectral characteristics in our GCxGC-MS analysis. All three classes of compounds were quantified by either compound specific calibration using known standards or relating total ion chromatogram (TIC) signals to calibration standards of similar volatility and polarity. In GCxGC, the TIC signal corresponds to a blob, or a region in volatility and polarity retention space. The GC-Image software package was used to create blobs from 2D chromatograms. Compounds were quantified by relating their TIC signal to that of the nearest standard in terms of polarity and volatility. Volatility bins were defined that are evenly spaced with their center elution times corresponding to each *n*-alkane. TIC blobs were quantified using the calibration for the available standard of similar polarity in the same volatility bin.

2.3.8 Emission Factor Calculations

Emissions data are presented as fuel-based emission factors (EF). Emission factors are calculated as the amount of analyte emitted by mass per gram of fuel emitted.

$$\mathrm{EF}_i(kg - fuel^{-1}) = \Delta m_i \frac{x_c(g)}{\Delta \mathrm{CO}_2(g) + \Delta \mathrm{CO}(g) + \Delta \mathrm{THC}(g)}$$

ΔCO_2, ΔCO, and ΔTHC are the background corrected carbon concentration of CO_2, CO, and THC (Drozd et al., 2016; Goldstein et al., 2017), respectively. x_c is the fuel carbon mass fraction of 0.82. Δm_i is the blank subtracted concentrations of species i.

2.3.9 Naphthalene and Iron Benchtop Study

To better understand the production of soluble iron during the water extraction process, a bench-top study was performed using three varying forms of iron with naphthalene. The iron stock solutions/suspensions included: 1) standardized San Joaquin soil (NIST SRM 2709a) containing 25 ppm total iron (soluble + insoluble) iron to determine the effects of crustal iron, 2) iron(II) sulfate to a concentration of 25 ppm to examine the effect of a soluble iron(II) source, and 3) iron(III) sulfate to examine a source of soluble iron(III). In parallel, 100 mg of naphthalene crystals were added to 200 mL of MQ water. For the experiment, 99 mL of the naphthalene suspension and 1 mL of the iron suspension were added to Teflon liners (250 ppb iron total), which were inserted into a jacketed glass beaker temperature controlled to 25 °C. After 16 hr of stirring, 2 ml were filtered (0.2 μm) and acidified to 5% nitric acid. Soluble iron released from the soil both in the presence and absence of naphthalene was analyzed by ICP-MS. Chemical changes in naphthalene in the presence and absence of iron were monitored by HPLC.

2.4. Results and Discussion

2.4.1 Total and Water-Soluble Element Exhaust Concentrations

	Total Elements	Water-Soluble Elements
Trace elements (μg kg-fuel^{-1})		
Na	50 (0, 200)	30 (0, 100)
Mg	40 (0, 200)	8 (0, 60)
Al	100 (0, 2000)	20 (0, 100)
K	20 (0, 100)	20 (0, 100)
Ca	200 (0, 1000)	200 (0, 1000)
Ti	1 (0, 60)	0.2 (0, 2)
V	0.02 (0, 0.7)	0.02 (0, 0.7)
Cr	5 (0.04, 20)	0.6 (0, 4)
Mn	2 (0.02, 10)	1 (0.007, 8)
Fe	80 (0, 400)	20 (0, 200)
Co	0.2 (0, 1)	0.04 (0, 0.7)
Ni	5 (0, 30)	2 (0, 10)
Cu	20 (0, 200)	20 (0, 100)
Zn	60 (0, 300)	40 (0, 300)
As	0.006 (0, 0.03)	0.006 (0, 0.03)
Se	0.3 (0, 2)	0.05 (0, 0.5)
Rb	0.2 (0, 0.5)	0.01 (0, 0.1)
Sr	1 (0.01, 4)	0.6 (0.003, 3)
Mo	5 (0, 20)	3 (0.002, 30)
Rh	0.06 (0, 0.5)	0.007 (0, 0.1)
Pd	0.8 (0, 6)	0.3 (0, 4)
Ag	0.1 (0, 2)	0.03 (0, 0.5)
Cd	0.007 (0, 0.3)	0.009 (0, 0.05)
Sb	0.2 (0, 1)	0.1 (0, 0.9)
Cs	0.005 (0, 0.02)	0.002 (0, 0.02)
Ba	5 (0, 20)	3 (0.06, 20)
Ce	4 (0, 40)	0.4 (0, 2)
Pt	0.04 (0, 0.4)	0.01 (0, 0.2)
Pb	0.4 (0, 7)	0.3 (0, 7)
U	0.002 (0, 0.03)	0.002 (0, 0.03)

Table 2.1: Average of total trace total and water-soluble elements from car exhaust reported in EF (μg kg-fuel^{-1}). These samples represent a range of different makes and models of cars. The values in the parenthesis are the range of the vehicle populualtion.

Emissions of ions, organic species, gaseous species, and EC/OC from these tests have been published previously (Drozd et al., 2016, 2019; Goldstein et al., 2017; Saliba et al., 2017). In order to obtain a better understanding of the factors that influence iron solubility, we compare these with the total elements, trace elements, and iron oxidation state measurements. Generally, the elements with the highest EF are the lighter crustal (n=32) elements Ca, Al, and Fe, with average EF 200, 100, and 80 µg kg-fuel^{-1} (Table 2.1), respectively. Iron has the third highest average EF of all the elements and the highest of all transition elements, ranging from 0 – 200 µg Fe kg-fuel^{-1}. This is followed by three first row transition elements: Zn, Cu, and Ni with the respective average EF of 60, 20, and 5 µg kg-fuel^{-1}. Other notable elements include Rh, Pd and Pt, likely originating from the catalytic convertor, with the respective average EF of 0.05, 0.7, and 0.04 µg kg-fuel^{-1}. Toxic elements include Chromium, Lead, Molybdenum and Antimony with respective EF 5, 0.8, 5 and 0.2 µg kg-fuel^{-1}. A previous study has shown that various elements are enriched in used motor oil such as copper, zinc, manganese, iron and lead which could originate from engine wear (Majestic et al., 2009).

Table 2.1 also shows the EF for the water-soluble fraction of the trace elements. The water-soluble EF for iron ranges from 0-150 µg kg-fuel^{-1}; or 0-82% of the total. At 20 µg kg-fuel^{-1}, average water-soluble iron was the third largest EF of all elements. There were relatively high emissions of a few other water-soluble elements such as Ca with an average EF of 200 µg kg-fuel^{-1} and Zn with tailpipe emissions averaging 40 µg kg-fuel^{-1}.

Only a few studies report tailpipe emissions (i.e., dynamometer testing) of trace elements for diesel and gasoline-powered passenger cars and even fewer which have

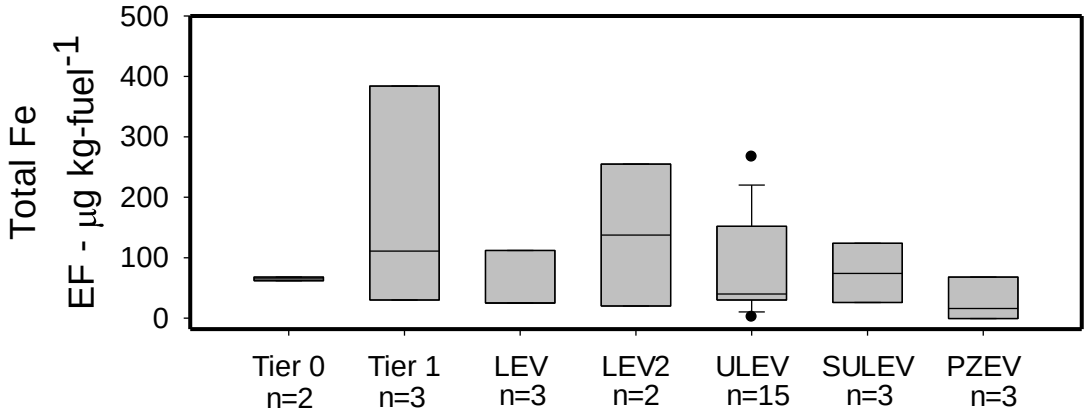

Figure 2.1: Total iron from the 32 vehicles tested reported in EF (µg kg-fuel^{-1}). The center black line represents the median value and the edges of the boxes represent the 25th and 75th percentiles while the whiskers extent are the 10th and 90th percentiles.

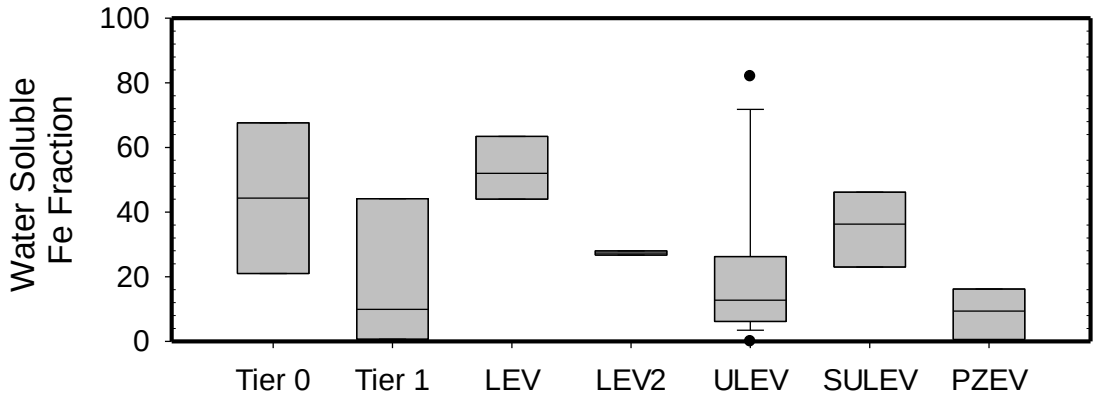

Figure 2.2: Water-soluble iron from the 32 vehicles tested reported in water-soluble iron fraction. The center black line represents the median value and the edges of the boxes represent the 25th and 75th percentiles while the whiskers are the 10th and 90th percentiles.

	This study Gasoline (n = 32)	Gasoline(Schauer et al., 2002) (n=9)	Gasoline(Norbeck et al., 1998) (n=40)	Diesel(Norbeck et al., 1998) (n=19)
Fleet Age	1990-2014	1981-1994	1972-1990	1977-1993
PM components (mg km^{-1})				
OC	1 (0.06, 10)	3.3 ± 0.21	16 ± 32	150 ± 330
EC	10 (0.06, 100)	0.77 ± 0.023	3.5 ± 4.8	160 ± 100
sulfate	0.02 (0.001, 0.1)	0.08 ± 0.16	0.93 ± 1.9	0.77 ± .93
Trace elements (µg km^{-1})				
Ag	0.01 (0, 0.25)	4.5 ± 20	0	0
Al	10 (0, 110)	20 ± 17	19 ± 37	31 ± 75
Ba	0.6 (0, 4.4)	0	0	68 ± 75
Ca	30 (0, 130)	26 ± 8.5	81 ± 120	650 ± 930
Cd	0.00 (0, 0.04)	0	0	0
Co	0.01 (0,0.25)	-	0	0
Cr	0.6 (0.008, 4)	0	0	6.2 ± 12
Cu	3 (0, 27)	0	6.2 ± 6.2	19 ± 31
Fe	10 (0, 62)	8.3 ± 2.3	280 ± 680	830 ± 1000
K	2 (0, 15)	3.0 ± 11.3	0	50 ± 170
Mg	7 (0, 120)	-	25 ± 31	99 ± 200
Mn	0.2 (0.002, 1.3)	0	0	6.2 ± 6.2
Mo	0.5 (0, 3.6)	2.3 ± 6.8	0	6.2 ± 12
Ni	0.6 (0, 5.2)	0	6.2 ± 12	12 ± 18
Pb	0.04 (0, 0.57)	0	25 ± 93	19 ± 62
Sb	0.02 (0, 0.21)	17 ± 39	0	0
Sr	0.1 (0, 0.68)	0.75 ± 2.3	0	0
Zn	7 (0, 37)	14 ± 1.5	110 ± 170	810 ± 1500

Table 2.2: Comparison of exhaust composition in g km^{-1} from different dynamometer studies which included both gasoline and diesel powered light duty vehicles. The values are the mean of the vehicle population and the values in the parenthesis are the minimum and maximum values. This table is in g km^{-1} opposed to g kg-$fuel^{-1}$ in Table 2.1.

reported iron water Table 2.2 compares the average exhaust PM composition and trace elements in distance-based emission factors in this study to literature values for other passenger vehicles, including one diesel and three gasoline exhaust studies. For all elements, the distance-based emission factors were greater in the diesel cohort, relative to the gasoline vehicles. Compared to previous studies, the trace elements emitted from older gasoline passenger vehicles resulted in an order of magnitude higher emissions for all elements, except for aluminum, which only showed a factor of ~2 increase in older vehicles (Table 2.2). Iron shows a large range in the three studies of gasoline vehicles, ranging from 8.3-280 μg km^{-1}, compared to the 0-62 μg km^{-1} measured in this study.

The large ranges in iron solubility of the previous studies led us to explore and compare the newer emission certification standard (Figure 2.1 and 2.2). Total iron did not trend strongly with emission certification standard, although, on average, total iron is less in the Tier 0 and LEV vehicles. Water-soluble iron shows a small average decrease of approximately 5 μg kg-$fuel^{-1}$ between ULEV and SULEV vehicles, and a further average decrease for the PZEV vehicles of 3.9 μg kg-$fuel^{-1}$.

2.4.2. Iron Correlations With Bulk Exhaust Components and Iron Oxidation State

To explore what factors and if any exhaust components are associated with the presence of water-soluble iron, linear regression analyses were used to compare soluble iron to different chemical species in the exhaust. Solubility from the direct exhaust was explored by comparing the EFs of both sulfate and nitrate to iron, and water-soluble iron

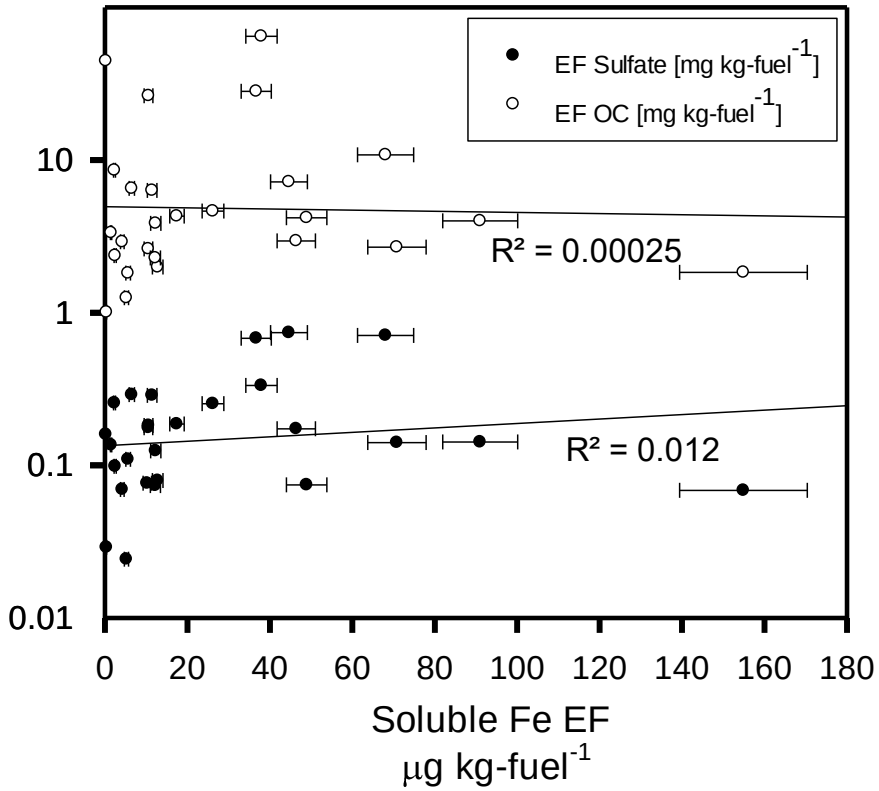

Figure 2.3: Linear correlation plots representing EF in mg kg-fuel-1 for sulfate and organic carbon (OC) in μg kg-fuel^{-1} for water-soluble iron. Correlation lines and R^2 values for all elements are shown.

was not correlated to either of these species (Appendix A1 and Figure 2.3). The EFs for water-soluble iron and CO_2 showed no correlation, suggesting that overall fuel use was not an important factor for water-soluble iron production (Appendix A1). Total iron was correlated to the water-soluble iron indicating the total amount of iron may have an impact on soluble iron (Appendix A2). Finally, to evaluate if water-soluble iron and overall particulate carbon relates, the EFs for elemental carbon (EC) and organic carbon (OC) were compared to that of soluble iron and, again, no correlation was observed (Appendix A1 and Figure 2.3).

As no correlation between water-soluble iron and bulk chemical species was observed (Appendix A1 and Appendix A3), the importance of the particle-bound iron oxidation state was investigated. Since Fe(II) is known to be more soluble than Fe(III), the expectation was that exhaust samples having a large Fe(II) character would have a greater iron solubility, relative to those containing Fe(III) or to Fe(0) (Stumm and Morgan, 1996). Figure 2.3 presents a scatter plot of the iron valence in 16 of the exhaust samples, compared with iron-bearing standards of known valence. This valence plot is generated from iron K-edge XANES data where parameters κ and μ are defined as normalized absorbance values at 7113 eV and 7117.5 eV, respectively. We observe that the exhaust-iron is primarily in the Fe(III) oxidation state, except for two vehicles: sample 11, dominated by Fe(0) and sample 15, containing a combination of Fe(0) and Fe(III) (Appendix A4). Sample 11 is an extreme case, having 0 % iron solubility and highly elevated amount of EC at 305 μg kg-fuel^{-1} (study average = 78 μg kg-Fuel^{-1}). The presence of Fe(0) is consistent with high EC, as both observations suggest a lack of

oxidation during the combustion and emission process. While the valence plot (Figure 2.3) put sample 15 as mostly Fe(II), the LCF actually showed that it was a mixture of Fe(0) and Fe(III). And, this sample contained only 10% water-soluble iron, less than the cohort average. The study-wide solid phase iron oxidation state is primarily Fe(III) or mixed oxidation state (Fe(III) and Fe(0)) (Figure 2.3), averaging about 30% water-soluble iron, well above the crustal background. LCF XANES fitting (Appendix A4) showed Fe(III) oxides and oxyhydroxides as the dominant group, followed by Fe(III) sulfates and iron silicates (Appendix A4). Hematite (α-Fe_2O_3) and maghemite (γ- Fe_2O_3) were the most consistently detected Fe(III) oxides. Iron was detected in all samples, with Zn, Cr and Cu the main other elements detected in nearly all samples (detection of low-Z elements below sulfur or high-Z elements above zinc was not possible in our experimental conditions). Overall, these results strongly suggest that the main driver of water-soluble iron is not associated with the particle-bound iron oxidation state. Further investigation for the LCF XANES fitting showed that 34% of iron speciated was Fe(III)-oxyhydroxides associated with organic material leading to the investigation of organic species which resulted in a correlation to longer chain IVOC and naphthalene (Appendix A6).

2.4.3. Iron Water-Solubility and Speciated Organics

Finally, the relationship between water-soluble iron and speciated organics, specifically naphthalene and IVOCs, was examined. In contrast with all other measured parameters, Figure 2.4 shows relatively strong correlations between water-soluble iron and some of the IVOC species. Figure 2.4 presents the classifications which have the

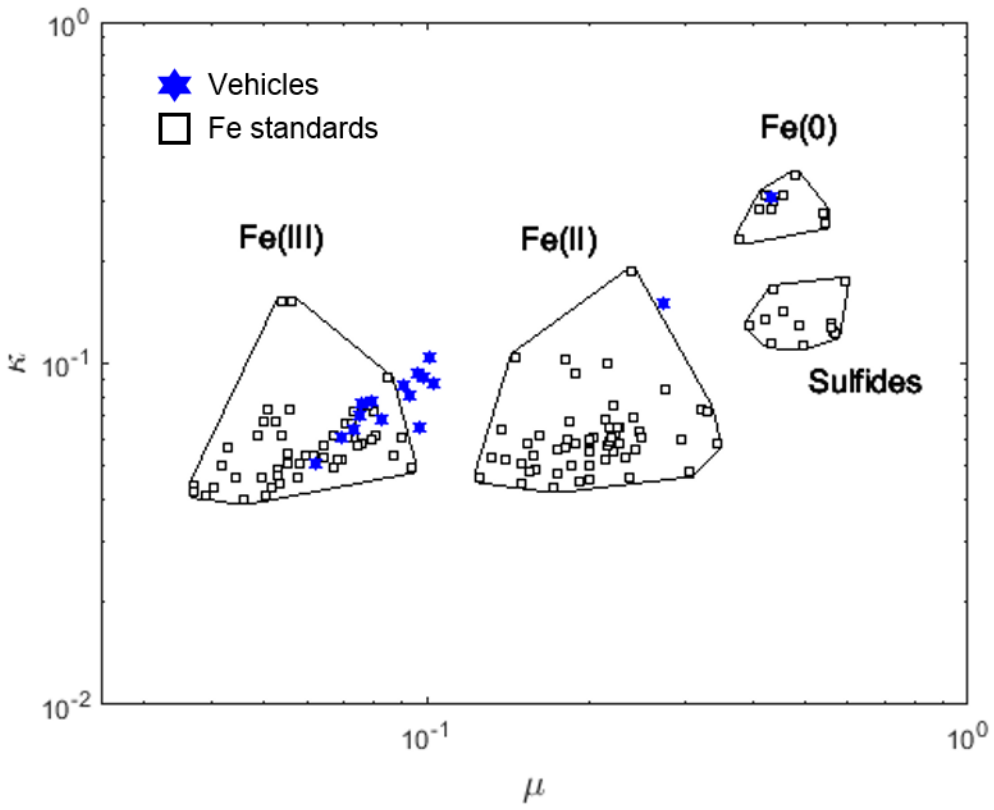

Figure 2.4: Iron valence scatter plot generated from iron K-edge XANES data where κ and μ are normalized absorbance values at 7113 eV and 7117.5 eV respectively. Empty black squares represent Iron standards of known valence while blue-filled stars represent vehicle exhaust samples.

strongest correlation with water-soluble iron. Water-soluble iron relationships with other IVOCs can be found in the supplementary information (Appendix A7). The correlation to water-soluble iron is highest for IVOC-polar species with 16 carbons ($R^2 = 0.56$). The variance of Figure 2.4 could result from the fact that, in addition to the IVOCs, other factors also influence iron water solubility.

As water-soluble iron trends well with naphthalene and polar-IVOCs, but not with bulk EC or OC, it is highly suggestive that iron solubility from the direct emission samples is primarily dependent on interactions with the species of carbon present in the particles during the extraction process. To better understand these interactions, a preliminary laboratory study was conducted to explore both i) the effect of these organic compounds on iron solubility and ii) the effect of soluble iron on the oxidation of organic compounds during the extraction process. Specifically, when naphthalene was added to an insoluble iron source (a soil), iron solubility increased from 0.8 to 4.2 % of the total, or by a factor of ~5.5, showing that the addition of naphthalene, alone, can have a significant effect on iron water solubility and that this effect likely is important during the extraction process.

Lacking oxidized functional groups, naphthalene was not expected to chelate iron or to, otherwise, have the ability to increase iron solubility. Thus, we investigated what presence of soluble iron, HPLC retention time analysis shows the presence of phthalic acid (12.5 minutes), phthalic anhydride (7.5 minutes), and naphthol (15 minutes). The peaks at and below 5 min were not identified but, based on the retention times, these are

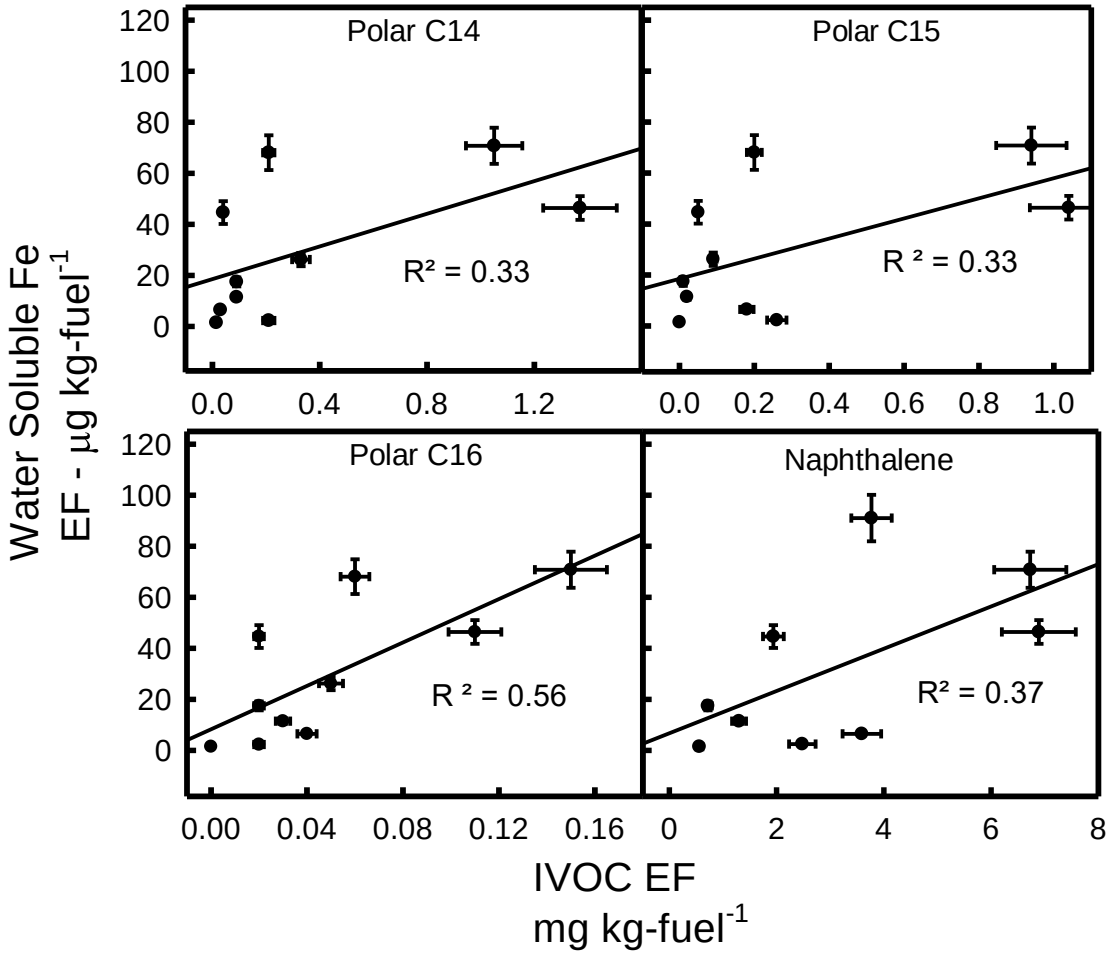

Figure 2.5: Scatter plots of water-soluble iron versus the sum of IVOCs reported in EF (g kg-fuel^{-1}).

thought to be low molecular mass, highly polar organic products and is consistent with other studies (Haynes et al., 2019)

2.4.4 Iron-Carbon Interactions

There are at least two methods in which organic compounds can lead to increased iron solubility: a) reduction of Fe(III) to Fe(II) or b) bringing soluble iron into solution via chelation. The first one is generally achieved by photochemistry (Pehkonen et al.,1993), which is not directly applicable to this study. The second, chelation, generally requires oxidized functional groups as shown in Figure 2.5. The extent of the ability for phthalic acid (a dicarboxylic acid) to chelate iron has not been reported, however, it is known that similar molecular mass organic diacids have significant ability to chelate iron, thus pulling it into solution (Paris and Desboeufs, 2013). Here, we suggest that the observed correlations between IVOC/naphthalene and water-soluble iron can be best explained with Fenton reactions, resulting in propagation of radical reactions (Pehkonen et al., 1993). As shown from the Fe XANES valance plot, the iron is predominately Fe(III) (Figure 2.4). In addition to the Fe(III), it has been shown that H_2O_2 forms in $PM_{2.5}$ water extracts and it been speculated that this formation is from various transition metals and/or quinones found in $PM_{2.5}$ (Wang et al., 2012).

$$Fe^{3+} + H_2O_2 \rightarrow Fe^{2+} + H^+ + HO_2^{\circ} \quad (1)$$

$$HO_2^{\circ} \rightarrow H^+ + O_2^{\circ -} \quad (2)$$

$$H^+ + O_2^{\circ -} + Naphthalene \rightarrow Oxidized\ Naphthalene \quad (3)$$

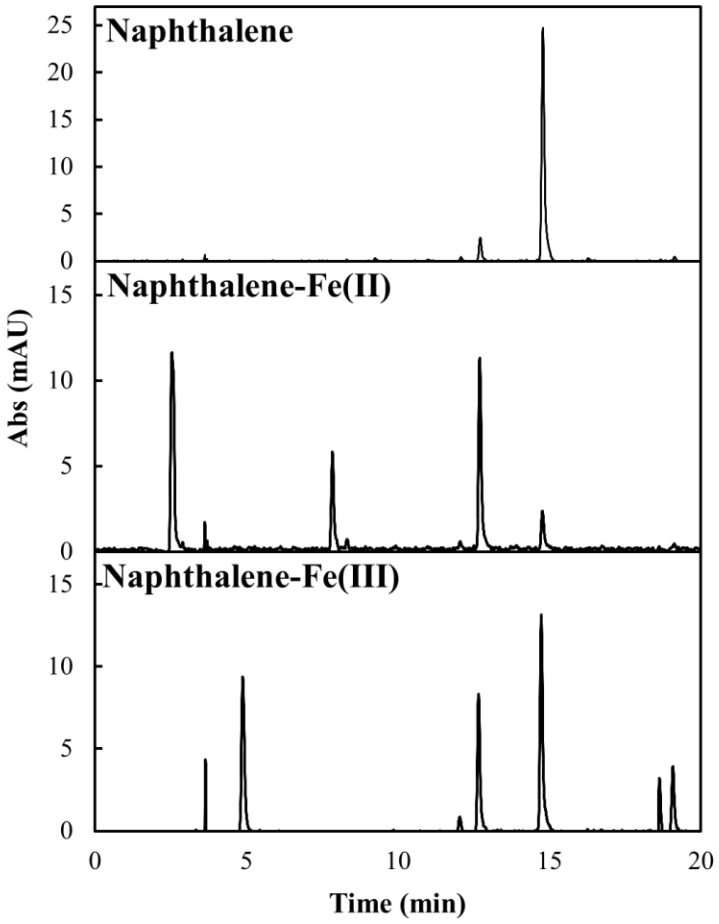

Figure 2.6: HPLC of resulting reaction between naphthalene and water-soluble iron. Phathalic acid at 12.5 minutes, phthalic anyhydride at 7.5 minutes, napthol at 15 minutes and naphthalene at 20 minutes. The column uses a C18 stationary phase on beads with 80Å pore size.

In the presence of H_2O_2, Fe(III) is known to undergo reaction (1) (Neyens and Baeyens, 2003b; Pignatello et al., 2006), resulting in the formation of Fe(II) and HO_2 (Pignatello et al., 2006; Rubio-Clemente et al., 2014), which degrades into superoxide, O_2^-, and H^+ (2). Superoxide has the ability to oxidize organic compounds, particularly aromatic structures (3) (Lair et al., 2008). The resulting structures of these oxidized compounds typically have two oxygen atoms, which could be arranged in various functional groups (Lair et al., 2008; Rubio-Clemente et al., 2014), also observed from the HPLC chromatograms (Figure 2.6). Oxidized single ring aromatic structures have a strong affinity to iron and have the ability chelate iron into aqueous solution (Haynes and Majestic, 2020; Hosseini and Madarshahian, 2009). Based on the laboratory studies of naphthalene and water-soluble iron presented here, naphthalene and/or IVOC oxidation during the extraction process is the most likely path towards increased iron solubility in primary tailpipe emissions. This overall process suggests that Fe(III) is emitted though car exhaust though interaction with water and organics undergoes a Fenton like reaction and converted to Fe(II) and the iron is chelated by the resulting oxidized organics.

2.5 Conclusions

This study shows water-soluble iron is directly formed from vehicle exhaust and not correlated to sulfates. The results show that iron is solubilized in water by specific organic compounds present in automobile exhaust, and that soluble iron is not necessarily dictated by the overall OC content. Thus, the implication is that anthropogenic water-soluble iron is a result of chelation from specific organic compounds, likely their eventual aqueous reaction products. Although the mechanism of these aqueous transformations

were not directly measured in this study, based on Fenton chemistry, the primary compounds are expected to be oxidized versions of naphthalene and/or IVOCs (Ledakowicz et al., 1999). Since these oxidation reactions occur fairly quickly (i.e., during the water extraction), further studies are of interest to better understand how these organic compounds interact with iron as it enters atmospheric waters and, also, the photo-chemical interactions between iron and organics.

2.6 Acknowledgements

The authors thank the excellent and dedicated personnel at the California Air Resources Board, especially at the Haagen–Smit Laboratory. This study was funded by National Science Foundation grant numbers 1342599 and 1549166. This research used resources of the Advanced Light Source, which is a DOE Office of Science User Facility under contract no. DE-AC02-05CH11231. Financial support was provided by the California Air Resources Board (Contract #12-318). The California Air Resources Board also provided substantial in-kind support for vehicle procurement, testing, and emissions characterization.

2.7 Author Contribution

The sample collection scheme was designed by Allen L. Robinson, Allen H. Goldstein and Brian J. Majestic. Samples were collected by Benton T. Cartledge and Greg T. Drozd. Organic speciation was performed by Greg T. Drozd. Trace elements were quantified by Joseph R. Salazar. Iron speciation was performed by Joseph R. Salazar, Rachel York-Marini and Brian J. Majestic, with the interpretation effort led by

Sirine C. Fakra. Bench-top naphthalene experiments were performed by John P. Haynes. Data integration was performed by Joseph R. Salazar. The manuscript was prepared by Joseph R. Salazar and Brian J. Majestic.

Chapter 3: Iron Speciation in $PM_{2.5}$ from Urban, Agriculture, and Mixed Environments in Colorado

3.1 Abstract

Field data is presented from the Platte River Air Pollution and Photochemistry Experiment (PRAPPE), aimed at understanding the interactions between organic carbon and trace elements in atmospheric particulate matter (PM). 24-hr $PM_{2.5}$ samples were collected during the summer (August 2017) and winter (December 2016 - March 2017), at three different sites on the Eastern Colorado plains: an urban, an agricultural, and a mixed site. Downtown Denver had an average total and water-soluble iron air concentration of 181.2 ng m^{-3} and 7.7 ng m^{-3}, respectively. Platteville, the mixed site, had an average of total iron of 76.1 ng m^{-3}, with average water-soluble iron concentration of 9.1 ng m^{-3}. Jackson State Park (rural/agricultural) had the lowest total iron average of 31.5 ng m^{-3} and the lowest water-soluble iron average, 1.3 ng m^{-3}. The iron oxidation state and chemical speciation of 97 samples across all sites and seasons was probed by x-ray absorption near edge structure (XANES) spectroscopy. The majority of the iron measured was almandine ($Fe_3Al_2Si_3O_{12}$) (Denver 21%, Platteville 16%, Jackson 24%), magnetite (Fe_3O_4) (Denver 9%, Platteville 4%, Jackson 5%) and Fe(III)dextran (Denver 5%, Platteville 13%, Jackson 5%), a surrogate for Fe-sugar complexes. No correlation was observed between iron solubility and the iron oxidation state or chemical speciation.

3.2 Introduction

The presence of iron in the ecosystem has major implications on various geochemical cycles (carbon and sulfur), redox environments, and nutrient availability (Le and Ricard, 1999; Mahowald et al., 2005; Wang and Cappellen, 1996). Iron serves as a necessary nutrient for primary producers, such as algae, and acts as a limiting nutrient in roughly half of the world's oceans (Division et al., 2013). In both biological and environmental media, the water-soluble iron fraction has been demonstrated to result in the creation of reactive oxygen species (ROS) (Faiola et al., 2011; Hamad et al., 2016; Park et al., 2006), likely generated through Fenton chemistry (Faiola et al., 2011; Kuang et al., 2017; Park et al., 2006). In biological systems, the production of ROS results in oxidative stress to the respiratory system and is suspected to be related to pulmonary inflammation, DNA damage, and the oxidation of proteins and lipids (Landreman et al., 2008; Park et al., 2006; Verma et al., 2014). Given these related health risks and iron's importance in biogeochemistry, an understanding of what controls atmospheric iron solubility is the primary driver of this study.

Iron is the most abundant transition element in the atmosphere, and results from windblown dust and urban air pollution (Jickells et al., 2005b; Mahowald et al., 2009). Typically, water-soluble iron from crustal sources is less than 1% of the total iron (Paris et al., 2010). This greatly differs from anthropogenic sources where water-soluble iron can range from 5-50% of total iron (Majestic et al., 2007; Petroselli et al., 2018; Salazar et al., 2019; Sedwick et al., 2007; Sholkovitz et al., 2012). The majority of anthropogenic water-soluble iron is estimated to result from combustion sources (Luo et al., 2008). The

resulting iron water-solubility is hypothesized to result from an interaction between organics and iron (III) (Haynes and Majestic, 2020; Paris and Desboeufs, 2013; Salazar et al., 2019).

In addition to giving insight into organic-iron interactions, the iron speciation may be an important predictor of its solubility. Synchrotron-based X-ray absorption near edge structure (XANES) spectroscopy has been used to investigate the Iron oxidation state and chemical speciation (iron's surrounding ligands) in the field samples. Prior reports making use of XANES have attempted to describe the relationship between water-soluble iron and its chemical speciation (Cartledge et al., 2015; Cartledge and Majestic, 2015b; Oakes et al., 2012a; Takahashi et al., 2011). Also, several ambient studies have been performed and Fe(III) has been observed as the principal oxidation state in $PM_{2.5}$, primarily as Fe-Al and Fe-Al-Si complexes, originating from windblown dust and soils (Fittschen et al., 2008; Oakes et al., 2012a).

In the present campaign, we seek to better understand how iron speciation and oxidation state can affect iron water-solubility across geographical areas and seasons. $PM_{2.5}$ was collected from three sites of multiple types: urban, agricultural, and mixed, and in both the winter and the summer. Samples were collected from each site and 97 Fe K-edge XANES spectra in total 31 from Denver (urban), 35 from Platteville (mixed) and 31 Jackson (agricultural) were analyzed along with total and water-soluble iron. The results were examined to understand how any patterns in season and source influence iron speciation, water-solubility, and oxidation state.

3.3 Materials and Methods

3.3.1 Materials Preparation

All vessel cleaning and analytical preparation was performed under a laminar flow hood with incoming air passing through a high efficiency particulate air (HEPA) filter (NuAire, Plymouth, MN). All water used was purified to 18.2 MΩ-cm (Milli-Q Thermo-Fisher Nanopore). An acid cleaning process was used to prepare the following: 15-ml and 50-ml plastic centrifuge vials, Petri dishes (Fisher), Teflon forceps (Fisher), syringes (Fisher), and 47 mm Teflon filters. For the plastic centrifuge vials, Petri dishes, Teflon forceps, syringe, and syringe cases this involved 24-hour soaks in a 10% reagent grade nitric acid bath, followed by 10% reagent grade hydrochloric bath, then a 3% trace metal grade nitric acid (Fisher) resting bath with 18.2 MΩ-cm water rinses before, after and between each step. Syringe filters (0.45-micron) (Whatman, Marlborough, MA) were prepared with 10% trace-metal grade hydrochloric acid, MQ water, and 5% nitric acid rinse. All materials were handled with powder free nitrile gloves (Fisher), double-bagged.

3.3.2 Sample Collection

$PM_{2.5}$ was collected at three sites in Colorado's eastern plains: 1) The Colorado Air Monitoring Program (CAMP) site in downtown Denver, an urban setting, 2) Jackson Lake State Park, a rural and agricultural setting, and 3) Platteville Elementary School in Platteville, CO, a mixed agricultural and urban setting that is geographically situated between the other sites (Figure 3.1).

Figure 3.1: Map of the three sampling site CAMP, Jackson and Platteville. (google maps)

Air was passed through a cyclone (URG-2000-30ENB) at 92 L min^{-1}, resulting in a $PM_{2.5}$ size cut. Each site had two sampling lines. One line collected $PM_{2.5}$ on a water cleaned Teflon filter for ion quantification and water-soluble organic experiments. The other sampling line was further split into two lines: one of the lines was collected onto a pre-baked quartz filter, and the other line was collected onto an acid cleaned Teflon filter. The acid cleaned Teflon filter was used for overall mass determination and trace metal measurements. The total flow was measured for each filter by a flow totalizer (Honeywell BK-G4 Meter).

One campaign was conducted in winter 2016-2017 and one in Summer 2017. Samples were collected in 24-hour intervals (midnight to midnight), automated using a 7-day timer (INTERMATIC Electromechanical Timer, 7-Day, SPDT, 21A) every other day in December 2016, February 2017, and August 2017. Exposed Teflon filters were stored in Petri dishes sealed with Teflon tape, double-bagged, and stored in a freezer (-20 ^{o}C) until analysis.

3.3.3 Water-Soluble Element Preparation

Water-soluble iron was extracted from the Teflon filters for twelve hours on a shaker table in 15 ml of 18.2 MΩ-cm water. The water extract was pre-washed filtered with 0.45 µm pore size polyethersulfone (PES) syringe filters. This filtered water-soluble extract was acidified to 5% trace-metal grade nitric acid and 2.5% trace-metal grade hydrochloric acid and analyzed by inductively coupled plasma mass spectrometry (ICP-MS, Agilent 7700).

3.3.4 Elemental Analysis

The polymethylpentene ring was removed from the Teflon filters and about 4% (measured exactly) of the filter was removed and used for Fe XANES spectroscopy. The remaining Teflon filter for each sample was placed into a microwave digestion vessel. In each digestion vessel, 750 µl of concentrated trace metal grade nitric acid, 250 µl of concentrated trace metal grade hydrochloric acid, 100 µl of concentrated trace metal grade hydrofluoric acid, and 100 µl of 30% hydrogen peroxide were added. The filters with the collected $PM_{2.5}$ were digested (Ethos EZ, Milestone Inc) according to the following temperature program: 15-minute ramp to 200 °C, then held at 200 °C for 25 minutes, and a 60-minute cooling period (Cartledge and Majestic, 2015b). Finally, the solution was removed and diluted to 15 ml with MQ water and analyzed via ICP-MS.

Blank filters and standard reference materials (SRMs) were digested alongside the collected $PM_{2.5}$ using the same digestion process described above. Two SRMs were used to address the recoveries of Iron in the digestion process: urban particulate matter (1648a, NIST) and San Joaquin Soil (2709a, NIST). The recoveries of the SRMs were between 80-120%. Indium (~1 ppb) was used as an internal standard and a He collision cell was used to remove polyatomic interferences.

3.3.5 XANES Spectroscopy

Fe K-edge X-ray absorption near-edge structure (XANES) and X-ray fluorescence (XRF) mapping data for 39 samples were collected at the Advanced Light Source Microprobe beamline (10.3.2), at Lawrence Berkeley National Laboratory,

Berkeley, CA (Marcus et al., 2004). A broad XRF map of each sample was acquired at 10 keV with 20 µm by 20 µm pixel size and 80 ms dwell time per pixel to locate the concentrated iron spots on the filter. Where iron was concentrated, a fine map was collected with 8 µm by 8 µm pixel size and 80 ms dwell time per pixel. From this map, 2-3 iron spots per filter were chosen for Fe K-edge extended XANES analysis (totaling 97 spectra). All data were recorded using a seven-element solid state Ge detector (Canberra, ON) in fluorescence mode by continuously scanning the Si (111) monochromator (Quick XAS mode) in the range of 7010-7415 eV. The spectra were then deadtime corrected, deglitched, calibrated, pre-edge background subtracted and post-edge normalized using a suite of LabVIEW custom programs (Marcus et al., 2008) available at the beamline. Spectra were calibrated using an iron foil with first derivative maximum set at 7110.75 eV (Kraft et al., 1996). Least-square linear combination fitting (LCF) was performed in the range 7090 to 7365 eV to identify oxidation states and iron speciation (Marcus et al., 2008).

3.4 Results

3.4.1 Water-Soluble Iron and Total Iron

Total and water-soluble iron from each region (urban, agricultural, and mixed) differed in averages and from day to day, and the results for all sites are presented in Figure 3.2. Downtown Denver had a summer and winter average of total iron of 181.2 ng m^{-3} (range: 80.9 - 380.5 ng m^{-3}) and an average of water-soluble iron of 7.7 ng m^{-3}, or

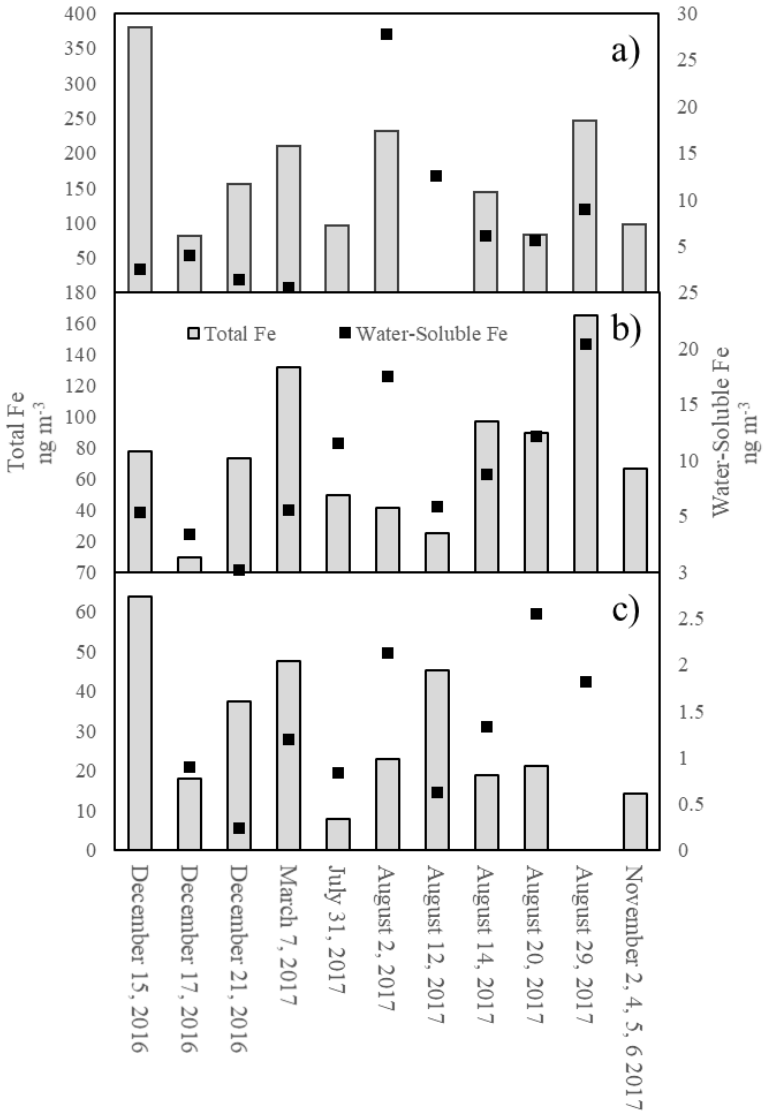

Figure 3.2: Total and water-soluble iron including sampling days from winter and summer. All samples were collected for 24-hours, except for November 2, 4, 5, 6, 2017, which was a 4-day sample. November 2, 4, 5, 6, 2017, was not tested for water-soluble iron. a) Denver. July 31, 2017 water-soluble iron was removed due to operational error in collection. b) Platteville. c) Jackson site.

4.2% of total iron (range: 0.5 – 27.8 ng m^{-3}). Platteville had an average of total iron of 76.1 ng m^{-3} (range: 9.6 – 165.6 ng m^{-3}) and average water-soluble iron of 9.1 ng m^{-3}, or 11.9% of total iron (range: 0.2 – 20.3 ng m^{-3}). Jackson State Park, the agricultural site, had the lowest total iron average of 31.5 ng m^{-3} (range: 7.9 – 63.7 ng m^{-3}) and the lowest water-soluble iron average, 1.3 ng m^{-3}, or 4.1% of total iron (range: 0.2 – 2.5 ng m^{-3}).

The extent of seasonal variations differs for the total and the water-soluble iron. Across all sites, winter had lower water-soluble iron with the average being 2.3 ng m^{-3} (range; 0.17 – 5.6 ng m^{-3}), while summer average of 8.6 ng m^{-3} (range; 0.6 – 27.8 ng m^{-3}). For total iron, however, winter was greater than the summer, on average. The winter average was 107.3 ng m^{-3} (range; 9.6 – 380.5 ng m^{-3}) and the summer average was 86.8 ng m^{-3} (range; 7.9 – 247.2 ng m^{-3}). Across all sites, iron fractional solubility for the winter was 2.1% and summers was 9.9%.

Total iron concentrations were correlated to the presence of multiple elements. Barium and antimony are shown in Figure 3.3. In Denver there was a strong correlation ($r^2 > 0.5$) of iron to barium, antimony, magnesium, aluminum, potassium, calcium, titanium, vanadium, chromium, manganese, nickel, cobalt, and copper. In Platteville, total iron was correlated to barium, magnesium, aluminum, calcium, titanium, chromium, and manganese, but not antimony, potassium, and copper, as in Denver. In Jackson, total iron was strongly correlated to magnesium, aluminum, potassium, calcium, titanium, and manganese, but not to barium, antimony, chromium, nickel, and copper. There were no strong correlations ($r^2 > 0.5$) to water-soluble iron to total elements for the majority of the samples except for iron and potassium at Jackson.

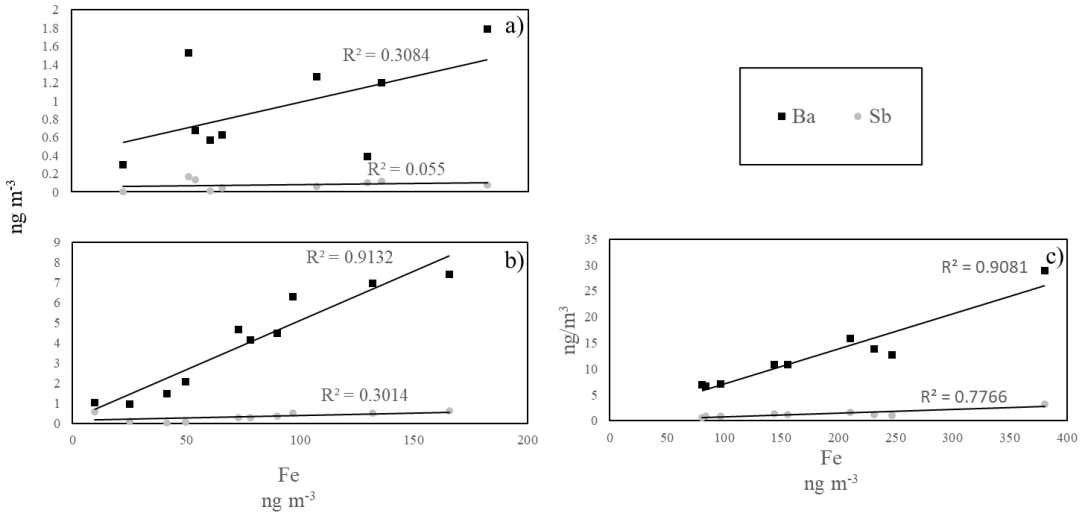

Figure 3.3: Iron vs barium and antimony. Each sample in is nanograms per cubic meter of air. a) Jackson (agricultural site). b) Platteville (mixed site). c) Denver (urban site).

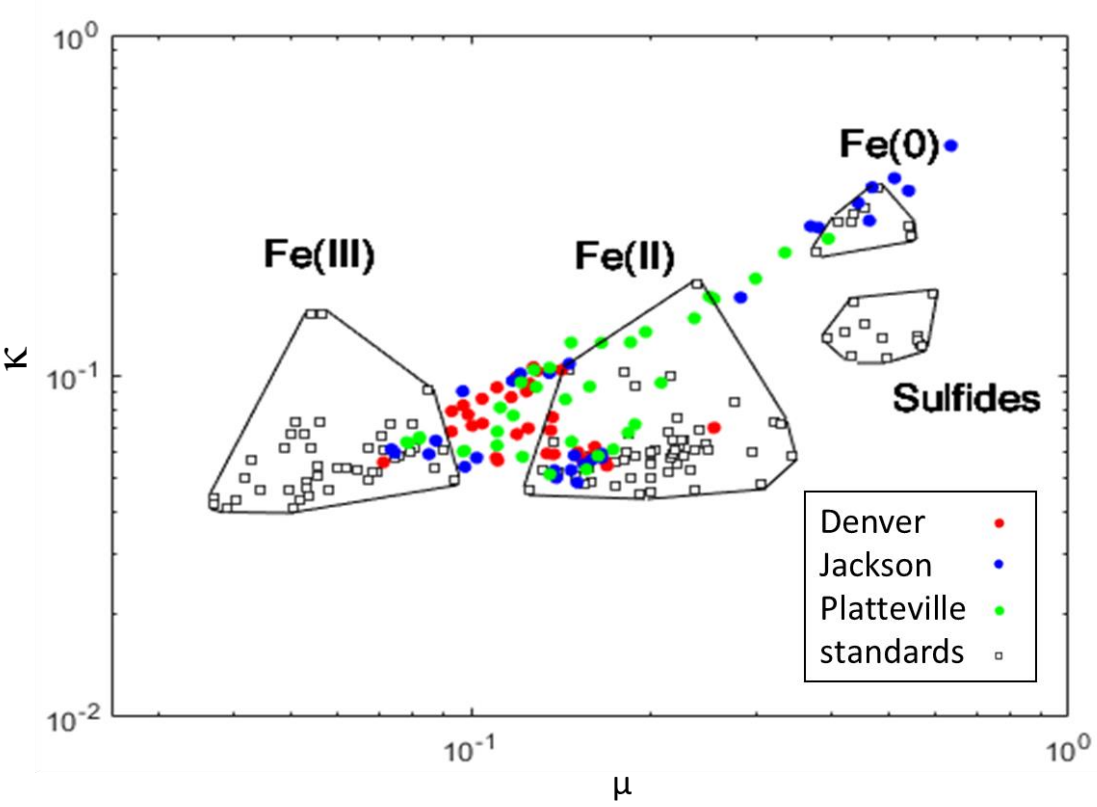

Figure 3.4: Iron valence scatter plot generated from Fe K-edge XANES data where κ and μ are normalized absorbance values at 7113 eV and 7117.5 eV respectively. Open black squares represent iron standards of known valence while the red dotes are the Denver site (urban), blue dote are Jackson (agricultural), and green dotes are Platteville (mixed).

3.4.2 Iron Oxidation States

An initial valence state scatter plot was generated using iron's K edge normalized XANES data to quickly classify particles according to iron oxidation states (Figure 3.4). The oxidation states observed were Fe(0), Fe(II), Fe(III) and mixed [a mixture of both Fe(II) and Fe(III)]. On a relative basis, the Jackson site observed the most Fe(0) and Fe(II) with less of the mixed and Fe(III). The Platteville site showed a large amount of Fe(II) and mixed iron phases. Denver had most samples fall in the mixed region followed by Fe(III) and then Fe(II).

A mixture of multiple iron mineral groups can be found for the iron that falls into the mixed oxidation state region in the valence plot. Using LCF, the fraction of Fe(II) and Fe(III) that are in the mixed area of the valence plot were obtained, adding more detail to the chemical speciation of iron in this region (Figure 3.5). Figure 3.5 shows two example Fe-XANES plots showing the weighted iron standards involved in the LCF of the plots. These percentages were obtained for each by summing the percentages for each oxidation state. Iron with mixed oxidation state were labeled as "mixed oxidation state". The average oxidation states for each iron sample per site: Denver Fe(III) 37%, Denver Fe(II) 39%, Platteville Fe(III) 44%, Platteville Fe(II) 32%, Jackson Fe(III) 27%, and Jackson Fe(II) 34%. Fe(0) was ubiquitous to all three sites, but to varying degrees: Jackson 27%, Platteville 13%, and Denver 3%. Fe(II) and Fe(III) were also compared between winter and summer for all sites. Fe(II) was shown to be 31% of all particles tested in the winter. In the summer, Fe(II) was accounted for 39% of the total iron tested. Fe(III) was found to be 39% in the winter of iron and in the summer Fe(III) shown to be 30% of iron.

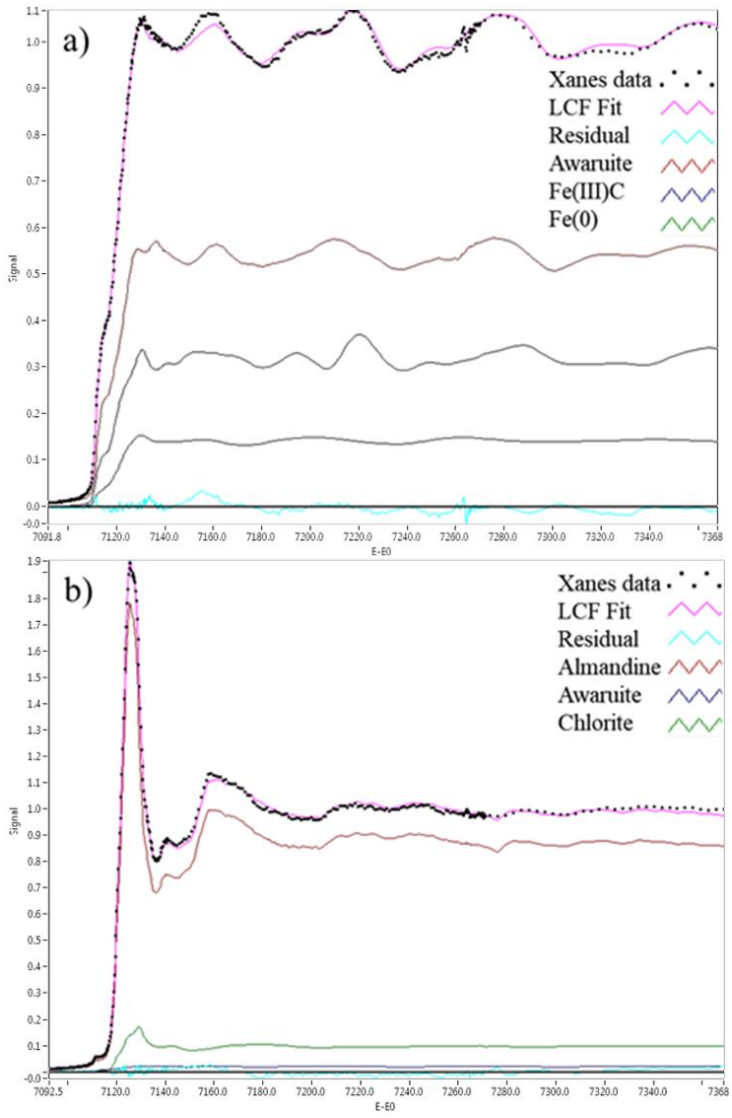

Figure 3.5: Least-square linear combination fitting (LCF) and respective weighted plots of the components or for the LCF of XANES plots. The components used in the fit are mineral standards measured at the ASL beam line 10.3.2. A) Sample collected on December 17th 2016 at Jackson lake state park LCF is comprised of 54.2% awaruite, 14.2% Fe(III) and 31.7 Fe(0). B) Sample collected on August 30th 2017 at Jackson lake state park LCF is comprised of 87.2% almandine trace amount of awaruite and chlorite.

LCF of Iron mineral groups	Denver	Platteville	Jackson
Almandine	21%	16%	24%
Magnetite	9%	4%	5%
Fe(III)dextran	5%	13%	5%
Feroxyhite	5%	3%	0%
Coalingite	5%	4%	4%
Fe biogenic oxide	5%	5%	0%
Hematite	3%	3%	5%
Kaolinite	2%	6%	6%

Table 3.1: Fraction of top eight iron species for each sampling site.

As Fe(II) is generally more water-soluble than Fe(III), the particle-bound oxidation states were compared to the percent water-soluble iron. Fe(II) and water-soluble iron by day showed no significant relationship ($R^2 = 0.03$). Fe(III) was tested against water-soluble iron and no relationship was found between Fe(III) and water-soluble iron ($R^2 = 0.00$). Generally, no relationship between iron solubility and oxidation state was observed for any iron species.

3.4.3 Iron Mineralogy

As no correlation was found between the iron oxidation state and its water-solubility, we probed deeper by investigating how iron speciation (i.e., ligands and immediate chemical environment) may affect the water-solubility. From the XANES spectra and the LCF, the percent of iron species were defined for each iron spot, then averaged together to look at the most common iron species for each site (Table 3.1). The most common iron species for all three sites was the mineral almandine ($Fe_3Al_2Si_3O_{12}$), which is an iron-aluminum-silicate complex. Almandine accounted for 21% of iron particles in Denver, 16% of iron particles in Platteville, and 24% of iron particles in Jackson. The second most common iron species was magnetite (Fe_3O_4) with 9% in Denver, 4% in Platteville, and 5% in Jackson. The third most common iron species was Fe(III)dextran, a surrogate for an iron-organic complex, which accounted for 5% of iron in Denver and Jackson and 13% of iron in Platteville.

3.5 Discussion

3.5.1 Total and Water-Soluble Iron

The Colorado Coarse Rural–Urban Sources and Health (CCRUSH) study found that, in residential neighborhoods in Denver, total iron in $PM_{2.5}$ was 89 ng m^{-3} at Alsup Elementary and 56 ng m^{-3} Edison Elementary (Clements et al., 2014). These locations were in different parts of Denver at distances less than 11 km from the CAMP sampling site. These concentrations were less than the average 181.2 ng m^{-3} measured in this study. In 2014, another study done in the same Denver location as the current study showed an average iron in $PM_{2.5}$ of 190 ng m^{-3} (Clements et al., 2014). This result illustrates the difference in concentrations in downtown versus residential neighborhoods within a major metropolitan area. Water-soluble iron was also measured in Denver in 2012 January to February averaging 29 ng m^{-3} which is more than the 7.7 ng m^{-3} measured in this study. However, those samples were extracted in a 0.5 mM acetate buffer (pH=4.25) compared to the pure 18.2 MΩ-cm water used here, and the acetate buffer is known to give a higher iron solubility compared to pure water (Cartledge and Majestic, 2015b; Majestic et al., 2006).

Iron water-solubility and oxidation state were examined for summer and winter. There was no change for iron oxidation state in winter and summer. Iron water-solubility was 3.8x higher in the summer (8.6 ng m^{-3}) then in the winter (2.3 ng m^{-3}). Water-soluble iron was not correlated to either particle-bound Fe(II) or Fe(III). This evidence indicates that iron oxidation stated is not a factor in iron solubility.

Barium and antimony are known to be tracers for brake dust, as they are emitted by ceramic brake pads (Lough et al., 2005; Majestic et al., 2009). Total iron in Denver is correlated to barium ($R^2 = 0.91$) and antimony ($R^2 = 0.78$) (Figure 3.2c) implying that the

iron in Denver is related to vehicular activity (brake dust or associated emissions) (Lough et al., 2005). Platteville had a strong correlation to barium ($R^2 = 0.93$) and a slightly to antimony ($R^2 = 0.30$). The resulting correlation could be either the lack of a large amount of antimony or another source of iron in $PM_{2.5}$ in Platteville (Figure 3.2b). Total iron in Jackson showed no correlation to barium ($R^2 = 0.308$) or antimony ($R^2 = 0.055$) (Figure 3.2a), suggesting that iron was not derived from vehicles. The total barium and antimony did not correlate to water-soluble iron. The lack of correlation of barium and antimony could be the result of the majority of iron resulting from brake wear and not from car exhaust.

3.5.2 Mineralogy

A surprisingly high fraction of the Iron found in Jackson (27 %) and Platteville (13 %) is in the native Fe(0) oxidation state. In solution, Fe(0) produces the most ROS compared with Fe(II) and Fe(III) (Phenrat et al., 2009). To our knowledge, this is the first study to measure native iron in the atmosphere in any significant amount.

Fe(II) aluminosilicates were found to be the most common form of iron at all three sites. Because of the association with aluminum and silicate, this shows that at least 20% of iron found in $PM_{2.5}$ in eastern Colorado is from crustal sources. Fe(II) aluminum silicate complexes have been previously found in other geographical areas (Oakes et al., 2012a; Petroselli et al., 2018). Petroselli et al. collected a $PM_{2.5}$ sample near a steel plant in Terni, Italy and measured Fe(III) as the predominate species in this sample. Oakes et al. collected 4 samples in both rural and urban sites and, similar to the results presented

here, found a large amount of Fe-aluminosilicates in all sites and did not show a variation in iron speciation from the two sites, an effect attributed to low sample size. Here, we had a larger sample size and observed no seasonal variation with respect to Fe-aluminosilicates, which helps to confirm the results from Oakes et al.

Magnetite, a mixed Fe(II,III) oxide has been found to originate from diesel vehicles and is present in crustal sources (Abdul-Razzaq and Gautam, 2001; Oakes et al., 2012a; Petroselli et al., 2018). Here we identified magnetite in 9% of iron tested in Denver, 5% in Platteville, and 4% in Jackson (Table 3.1). The increase of magnetite in combination with the correlation of iron to barium and antimony strongly suggest that it can originate from vehicular activity in Denver. There is less evidence for magnetite being related diesel vehicles in Platteville and Jackson resulting from showing lower percentages of magnetite and a smaller correlation to break wear elements.

Fe(III)dextran is an iron-sugar complex. Fe(III)dextran is used as an surrogate for iron complexed to oxidized organic species. Water-soluble Iron has been hypothesized to primarily result from biomass burning, whose emissions contain sugars like levoglucosan, mannosan, and galactosan (Scaramboni et al., 2015). Concentration of sugars from biomass burning can range from 6 ng m^{-3} to 12.5 µg m^{-3} (Scaramboni et al., 2015; Theodosi et al., 2018), and they are highly water-soluble (Barbaro et al., 2019; Simoneit et al., 2004). Water-solubilization of iron by theses sugar complexes in biomass burning fumes could be a large contributor to total water-soluble iron. However, since these organic biomass sugar compounds were not measured in this study, this could not be directly tested here.

3.6 Conclusion

Iron was tested from three different environments in the eastern plains of Colorado. The most common mineral found was almandine, which accounted for 20% of total iron tested. The large prevalence of the Si-Fe complexes suggests a large contribution from natural, crustal sources, even within urban areas. Fe(III)dextran, an organic iron complex and magnetite were also abundant. Iron oxidation states were compared seasonally, where no change in oxidation state was observed, however, an increase in iron water-solubility was present in the summer. Finally, water-soluble iron was compared to Fe(II) and Fe(III), and results indicated there is no relationship between iron oxidation state and water-soluble iron.

3.7 Acknowledgements

The authors thank the Colorado Department of Public Health and Environment for the use of the air monitoring facility. This study was funded by National Science Foundation grant number 1549166. This research used resources of the Advanced Light Source, which is a DOE Office of Science User Facility under contract no. DE-AC02-05CH11231.

Chapter 4: Summary and Further

This dissertation describes iron's solubilization, characterization, and oxidation state in urban environments. Iron was introduced and the importance described and how it relates to the environment and heath. Iron was then characterized from car exhaust. Finally, iron in urban environments was analyzed and compared to agricultural environments. This dissertation described a novel process of iron and organic interacting to solubilize iron. Next, iron was defined coming from multiple sources and different types of iron were identified.

Chapter one introduced previous research and understanding of PM and iron. Iron is a leading cause of multiple health and environmental effects; therefor, research is invested in understanding the process of iron water-solubilization. Different hypotheses described iron water-solubility including, an acid-based reduction process and an organic iron interaction. Methods of iron quantification were explained it better understood how iron is analyzed and chapter one described how iron's oxidation states are found and speciated though multiple methods.

Chapter two examined car exhaust and how it influences water-soluble iron. Here, it was discovered that iron originating from car exhaust resulted in an average of 30% water-soluble iron. Water-soluble iron from car exhaust was not correlated to sulfates or nitrates, suggesting these ions were not the cause of water-solubilizing iron. While this

isn't the first study to show a lack of correlation to acidic species, it adds to the body of work that thoroughly examines acid-iron interactions (Cartledge et al., 2015; Cwiertny et al., 2008; Fu et al., 2012, 2014). Organic carbon, elemental carbon, and CO_2 was not correlated to the amount of water-soluble iron, and the lack of correlation showed that total car exhaust was not a factor in solubilizing iron. XANES was used to examine iron samples showing that the primary oxidation state was Fe(III), rather than the more water-soluble Fe(II). Fe(III) as the primary oxidation state is consistent with findings from urban PM XANES experiments (d'Acapito et al., 2014; Majestic et al., 2007; Oakes et al., 2012b; Petroselli et al., 2018). This XANES study gave an understanding of one of the many sources in which, iron might come from. Further work could be done to speciate iron from break and tire wear as this adds to iron found in PM (Majestic et al., 2009). The XANES experiments did find a large amount of organic iron complexes and agrees with the growing body of evidence that organic molecules are solubilizing iron (Upadhyay et al., 2011). This led to a correlation study to identify the organic species that results in water-soluble iron. Water-soluble iron was correlated to 204 organic species and developed an understanding that water-soluble iron resulted from specific organic molecules. The only organics that were strongly correlated ($R^2 < 0.5$) to water-soluble iron are IVOCs and naphthalene. The study presented in chapter 2 is the first of its kind to correlate iron to IVOCs and naphthalene directly from car exhaust. This unique correlation developed the hypothesis iron becomes water-soluble as a result of IVOC or naphthalene. Further investigation led to a bench top study testing iron and Naphthalene solubility and showed that naphthalene increased iron water-solubility by 5.5 times. The

increase in iron water-solubility from naphthalene further verified the presented hypothesis. It would be beneficial in future work to test IVOCs in a controlled setting to understand how IVOCs interact with iron. In summary, chapter 2 showed that water-soluble iron from car exhaust was not correlated to any acidic species as previously and then showed that it was correlated to IVOC and Naphthalene developing a new fundamental understanding of water-soluble iron. From this understanding of iron, further work could be done to investigate the occurrence of iron interacting with IVOCs or naphthalene in urban PM. Since IVOCs are shown to water-solubilize iron, the next possible research would be to understand if secondary volatile organic carbon (SVOCs) interact with an iron water-solubilization prosses in the atmosphere. Understanding iron and IVOC interactions could be beneficial to describing and modeling the sources of water-soluble iron deposits into the ocean. ROS and water-soluble iron have been correlated thus, understanding the ROS production of the combination of IVOCs and iron might provide insightful information on the resulting health effects.

PRAPPE is a project aimed at understanding iron contained in PM from different environments. This chapter adds to the growing work of atmospheric iron speciation and oxidation states found by XANES. The majority of iron found in Colorado was in the Fe(III) oxidation state as well as quantities of Fe(II) and Fe(0) were found. Fe(III) has been verified as being the most common form of iron in the atmosphere (d'Acapito et al., 2014; Majestic et al., 2007; Oakes et al., 2012b; Petroselli et al., 2018). Here we confirmed Fe(III) was the most prevalent oxidation state. Fe(0) was also found and is unique to this study. Most of the iron was identified to be a Fe-Al-Si compounds and this

is recognized to originate from windblown dust. Fe-Al-Si compounds have been found in large abundance in Atlanta, GA and Saharan dust and now in Denver (Oakes et al., 2012b; Petroselli et al., 2018). Here it was found that the iron oxides were the second largest contributor to iron. While there have been some studies showing iron oxides resulting from diesel vehicle exhaust, it would be valuable to explore more sources of iron oxides in PM. Third most prevalent iron speciation was an iron sugar complex. The iron sugar complexes could be involved in water-solubilizing iron and future work can be done to investigate iron's water-solubility as it relates to sugar complexes resulting from biomass burning. There was no correlation between iron water-solubility and iron oxidation state. adding to the growing body of work showing that iron water-solubility dose not depends on the oxidation of iron. Iron's oxidation state was found from three different environments and it is the first of its kind to use XANES. In addition, this study was the first of its kind to do a large iron oxidation state analysis across season and environments. Here we identified that a large source of iron comes from crustal dust, but additional work could be done in order to identify the sources of anthropogenic iron and water-soluble iron.

This dissertation has described the speciation of iron from car exhaust and describe iron contained in $PM_{2.5}$. Three hypotheses were examined, and it was discovered that specific organic carbon water-solubilized iron. The iron-organic interaction has shown an insight into water-soluble iron's chemical state in the environment and further research could be done to understand the implications it has on biogeochemical cycles. This understanding of the organic-iron interaction should be further explored in the ROS

production in PM thus, leading to a better understanding of health effects of water-soluble iron. The information contained here has added to the understanding of the water-solubilization of iron and shows evidenced of iron-organic interactions.

References

Abdul-Razzaq, W. and Gautam, M.: Discovery of magnetite in the exhausted material from a diesel engine, Appl. Phys. Lett., 78(14), 2018–2019, doi:10.1063/1.1358357, 2001.

Auffan, M., Achouak, W., Rose, J., Roncato, M.-A., Chaneac, C., Waite, D. T., Wiesner, M. R., Masion, A., Bottero, J.-Y. and Woicik, J. C.: Relation between the Redox State of Iron-Based Nanoparticles and Their Cytotoxicity toward Escherichia coli, Environ. Sci. Technol., 42(17), 6730–6735, 2008.

Baba, Y., Yatagai, T., Harada, T. and Kawase, Y.: Hydroxyl radical generation in the photo-fenton process: Effects of carboxylic acids on iron redox cycling, Chem. Eng. J., 277, 229–241, doi:10.1016/j.cej.2015.04.103, 2015.

Baker, A. R., Jickells, T. D., Witt, M. and Linge, K. L.: Trends in the solubility of iron, aluminium, manganese and phosphorus in aerosol collected over the Atlantic Ocean, Mar. Chem., 98(1), 43–58, doi:10.1016/j.marchem.2005.06.004, 2006.

Barbaro, E., Feltracco, M., Cesari, D., Padoan, S., Zangrando, R., Contini, D., Barbante, C. and Gambaro, A.: Characterization ofthewater soluble fraction in ultrafine, fine, and coarse atmospheric aerosol, Sci. Total Environ., 658, 1423–1439, doi:10.1016/j.scitotenv.2018.12.298, 2019.

Batista, A. P. S. and Nogueira, R. F. P.: Parameters affecting sulfonamide photo-Fenton degradation - Iron complexation and substituent group, J. Photochem. Photobiol. A Chem., 232, 8–13, doi:10.1016/j.jphotochem.2012.01.016, 2012.

Bell, M. L., Dominici, F., Ebisu, K., Zeger, S. L. and Samet, J. M.: Spatial and Temporal Variation in PM 2 . 5 Chemical Composition in the United States for Health Effects Studies, , 115(7), 989–995, doi:10.1289/ehp.9621, 2007.

Bonnet, S.: Dissolution of atmospheric iron in seawater, Geophys. Res. Lett., 31(3), L03303, doi:10.1029/2003GL018423, 2004.

Cartledge, B. T. and Majestic, B. J.: Metal concentrations and soluble iron speciation, Atmos. Pollut. Res., (6), 495–505, 2015a.

Cartledge, B. T. and Majestic, B. J.: Metal concentrations and soluble iron speciation in fine particulate matter from light rail activity in the Denver-Metropolitan area, Atmos. Pollut. Res., 6(3), 495–502, doi:10.5094/APR.2015.055, 2015b.

Cartledge, B. T., Marcotte, A. R., Herckes, P., Anbar, A. D. and Majestic, B. J.: The Impact of Particle Size, Relative Humidity, and Sulfur Dioxide on Iron Solubility in Simulated Atmospheric Marine Aerosols, Environ. Sci. Technol., 49(12), 7179–7187, doi:10.1021/acs.est.5b02452, 2015.

Chen, Y. and Siefert, R. L.: Seasonal and spatial distributions and dry deposition fluxes of atmospheric total and labile iron over the tropical and subtropical North Atlantic Ocean, J. Geophys. Res. D Atmos., 109(9), doi:10.1029/2003JD003958, 2004.

Cheung, K. L., Ntziachristos, L., Tzamkiozis, T., Schauer, J. J., Samaras, Z., Moore, K. F. and Sioutas, C.: Emissions of particulate trace elements, metals and organic species from gasoline, diesel, and biodiesel passenger vehicles and their relation to oxidative potential, Aerosol Sci. Technol., 44(7), 500–513, doi:10.1080/02786821003758294,

2010.

Chow, J. C. and Watson, J. G.: Review of PM 2 . 5 and PM 10 Apportionment for Fossil Fuel Combustion and Other Sources by the Chemical Mass Balance Receptor Model, , 51(8), 809–847, doi:10.1021/ef0101715, 2002.

Chuang, P. Y., Duvall, R. M., Shafer, M. M. and Schauer, J. J.: The origin of water soluble particulate iron in the Asian atmospheric outflow, Geophys. Res. Lett., 32(7), 1–4, doi:10.1029/2004GL021946, 2005.

Clements, N., Eav, J., Xie, M., Hannigan, M. P., Miller, S. L., Navidi, W., Peel, J. L., Schauer, J. J., Shafer, M. M. and Milford, J. B.: Concentrations and source insights for trace elements in fine and coarse particulate matter, Atmos. Environ., 89, 373–381, doi:10.1016/j.atmosenv.2014.01.011, 2014.

Coale, K. H., Johnson, K. S., Fitzwater, S. E., Gordon, R. M., Tanner, S., Chavezt, F. P., Ferioli, L., Sakamoto, C., Rogers, P., Millerot, F., Steinbergt, P., Ii, P. N., Cooper, D., Cochlan, W. P., Landry, M. R., Constantinou, J., Rollwagen, G., Trasvina, A. and Kudela, R.: A massive phytoplankton bloom induced by an ecosystem-scale iron fertilization experiment in the equatorial Pacific Ocean, , 383(334), 1996.

Cwiertny, D. M., Baltrusaitis, J., Hunter, G. J., Laskin, A., Scherer, M. M. and Grassian, V. H.: Characterization and acid-mobilization study of iron-containing mineral dust source materials, , 113, 1–18, doi:10.1029/2007JD009332, 2008.

d’Acapito, F., Mazziotti Tagliani, S., Di Benedetto, F. and Gianfagna, A.: Local order and valence state of Fe in urban suspended particulate matter, Atmos. Environ., 99, 582–

586, doi:10.1016/j.atmosenv.2014.10.028, 2014.

Desboeufs, K. V, Losno, R., Vimeux, F. and Cholbi, S.: The pH-dependent dissolution of wind-transported Saharan dust, J. Geophys. Res., 104(D17), 21,287-21,299, 1999.

Division, G. D., Hole, W., Hole, W., Division, G. D. and Science, E.: Marine Ecosystem Dynamics and Biogeochemical Cycling in the Community Earth System Model [CESM1 (BGC)]: Comparison of the 1990s with the 2090s under the RCP4 . 5 and, , 1, 9291–9312, doi:10.1175/JCLI-D-12-00566.1, 2013.

Dockery, D. W., Pope, A., Xu, X., Spengler, J. D., Ware, J. H., Fay, M. E., Ferris, B. G. and Speizer, F. E.: An Association between Air Pollution and Mortality in Six U.S. Cities, new Engl. Joural Madicine, 329(24), 1753–1759, doi:10.1056/NEJM199312093292401, 1993.

Drozd, G. T., Zhao, Y., Saliba, G., Frodin, B., Maddox, C., Weber, R. J., Chang, M. C. O., Maldonado, H., Sardar, S., Robinson, A. L. and Goldstein, A. H.: Time Resolved Measurements of Speciated Tailpipe Emissions from Motor Vehicles: Trends with Emission Control Technology, Cold Start Effects, and Speciation, Environ. Sci. Technol., 50(24), 13592–13599, doi:10.1021/acs.est.6b04513, 2016.

Drozd, G. T., Zhao, Y., Saliba, G., Frodie, B., Maddox, C., Chang, M.-C. O., Maldonado, H., Sardar, S., Weber, R. J., Robinson, A. L. and Goldstein, A. H.: Detailed Speciation of Intermediate Volatility and Semivolatile Organic Compound Emissions from Gasoline Vehicles: Effects of Cold-Starts and Implications for Secondary Organic Aerosol Formation., Environ. Sci. Technol., 53(3), 1706–1714, 2019.

Engwall, M. A., Pignatello, J. J. and Grasso, D.: Degradation and Detoxification of the Wood Preservatives Creosote and Pentachlorophenol in Water by the Photo-Fenton Reaction, , 33(5), 1999.

Faiola, C., Johansen, A. M., Rybka, S., Nieber, A., Thomas, C., Bryner, S., Johnston, J., Engelhard, M., Nachimuthu, P. and Owens, K. S.: Ultrafine particulate ferrous iron and anthracene associations with mitochondrial dysfunction, Aerosol Sci. Technol., 45(9), 1109–1122, doi:10.1080/02786826.2011.581255, 2011.

Finlayson-Pitts, B. J. and Pitts, J. N.: Chemistry of the Upper and Lower Atmosphere., 2000.

Fiordelisi, A., Piscitelli, P., Trimarco, B., Coscioni, E., Iaccarino, G. and Sorriento, D.: The mechanisms of air pollution and particulate matter in cardiovascular diseases, Heart Fail. Rev., 22(3), 337–347, doi:10.1007/s10741-017-9606-7, 2017.

Fittschen, U. E. A., Meirer, F., Streli, C., Wobrauschek, P., Thiele, J., Falkenberg, G. and Pepponi, G.: Characterization of atmospheric aerosols using Synchroton radiation total re fl ection X-ray fl uorescence and Fe K-edge total re fl ection X-ray fl uorescence-X-ray absorption near-edge structure, Spectrochim. Acta Part B At. Spectrosc., 63(12), 1489–1495, doi:10.1016/j.sab.2008.10.016, 2008.

Frahm, R.: Quick scanning exafs: First experiments, Nucl. Inst. Methods Phys. Res. A, 270(2–3), 578–581, doi:10.1016/0168-9002(88)90732-2, 1988.

Fu, H., Lin, J., Shang, G., Dong, W., Grassian, V. H., Carmichael, G. R., Li, Y. and Chen, J.: Solubility of Iron from Combustion Source Particles in Acidic Media Linked to

Iron Speciation, Environ. Sci. Technol., 46, 11119−11127, doi:dx.doi.org/10.1021/es302558m, 2012.

Fu, H. B., Shang, G. F., Lin, J., Hu, Y. J., Hu, Q. Q., Guo, L., Zhang, Y. C. and Chen, J. M.: Fractional iron solubility of aerosol particles enhanced by biomass burning and ship emission in Shanghai, East China, Sci. Total Environ., 481(1), 377–391, doi:10.1016/j.scitotenv.2014.01.118, 2014.

Fu, P., Guo, X., Man, F., Cheung, H., Kin, K. and Yung, L.: Science of the Total Environment The association between PM 2 . 5 exposure and neurological disorders : A systematic review and meta-analysis, Sci. Total Environ., 655, 1240–1248, doi:10.1016/j.scitotenv.2018.11.218, 2019.

Gao, Y.: Aeolian iron input to the ocean through precipitation scavenging: A modeling perspective and its implication for natural iron fertilization in the ocean, J. Geophys. Res., 108(D7), 4221, doi:10.1029/2002JD002420, 2003.

Goldstein, A., Robinson, A., Kroll, J., Drozd, G., Zhao, Y., Saliba, G., Saleh, R. and Presto, A.: Investigating Semi-Volatile Organic Compound Emissions from Light-Duty Vehicles., 2017.

Hamad, S. H., Schauer, J. J., Antkiewicz, D. S., Shafer, M. M. and Kadhim, A. K. H.: ROS production and gene expression in alveolar macrophages exposed to PM2.5 from Baghdad, Iraq: Seasonal trends and impact of chemical composition, Sci. Total Environ., 543, 739–745, doi:10.1016/j.scitotenv.2015.11.065, 2016.

Hand, J. L., Mahowald, N. M., Chen, Y., Siefert, R. L., Luo, C., Subramaniam, A. and

Fung, I.: Estimates of atmospheric-processed soluble iron from observations and a global mineral aerosol model: Biogeochemical implications, J. Geophys. Res. D Atmos., 109(17), 1–21, doi:10.1029/2004JD004574, 2004.

Haynes, J. and Majestic, B.: Role of polycyclic aromatic hydrocarbons on the photo-catalyzed solubilization of simulated soil-bound atmospheric iron, Atmos. Pollut. Res., 11(3), 583–589, doi:https://doi.org/10.1016/j.apr.2019.12.007, 2020.

Haynes, J. P., Miller, K. E. and Majestic, B. J.: Investigation into Photoinduced Auto-Oxidation of Polycyclic Aromatic Hydrocarbons Resulting in Brown Carbon Production, Environ. Sci. Technol., 53(3), 682–691, doi:10.1021/acs.est.8b05704, 2019.

Hei: Understanding the Health Effects of Components of the Particulate Matter Mix: Progress and Next Steps, , (April), 1–20, 2002.

Hickox, W. H., Werner, B. and Gaffney, P.: Air Resources Board, , (Mld), 1–6 [online] Available from: http://www.arb.ca.gov/ei/see/memo_ag_emission_factors.pdf, 2000.

Hosseini, M. S. and Madarshahian, S.: Investigation of charge transfer complex formation between Fe(III) and 2,6-Dihydroxy benzoic acid and its applications for spectrophotometric determination of iron in aqueous media, E-Journal Chem., 6(4), 985–992, doi:10.1155/2009/417303, 2009.

Hta, A. T. O., Suno, H. I. T., Agi, H. I. K., Anai, Y. U. K., Omura, M. A. N., Hang, R. E. Z., Erashima, S. H. T. and Mai, N. O. I.: Chemical compositions and XANES speciations of Fe , Mn and Zn from aerosols collected in China and Japan during dust events, , 40, 363–376, 2006.

Iii, C. A. P., Dockery, D. W., Iii, C. A. P., Iii, C. A. P., Dockery, D. W. and Dockery, D. W.: Health Effects of Fine Particulate Air Pollution : Lines that Connect Health Effects of Fine Particulate Air Pollution : Lines that Connect, , 2247, doi:10.1080/10473289.2006.10464485, 2012.

Ito, A.: Atmospheric Processing of Combustion Aerosols as a Source of Bioavailable Iron, , doi:10.1021/acs.estlett.5b00007, 2015.

Jickells, T. D., An, Z. S., Andersen, K. K., Baker, a R., Bergametti, G., Brooks, N., Cao, J. J., Boyd, P. W., Duce, R. a, Hunter, K. a, Kawahata, H., Kubilay, N., LaRoche, J., Liss, P. S., Mahowald, N., Prospero, J. M., Ridgwell, a J., Tegen, I. and Torres, R.: Global iron connections between desert dust, ocean biogeochemistry, and climate., Science, 308(5718), 67–71, doi:10.1126/science.1105959, 2005a.

Jickells, Z. S. A., Andersen, K. K., Baker, A. R., Bergametti, G., Brooks, N., Cao, J. J., Boyd, P. W., Duce, R. A., Hunter, K. A., Kawahata, H., Kubilay, N., LaRoche, J., Liss, P. S., Mahowald, N., Prospero, J. M., Ridgewell, A. J., Tegen, I. and Torres, R.: Global iron concentrations between desert dust, ocean biogeochemistry, and climate, Science (80-.)., 308(April), 67–71, 2005b.

Karagulian, F., Belis, C. A., Francisco, C., Dora, C., Prüss-ustün, A. M., Bonjour, S., Adair-rohani, H. and Amann, M.: Contributions to cities' ambient particulate matter (PM): A systematic review of local source contributions at global level, Atmos. Environ., 120, 475–483, doi:10.1016/j.atmosenv.2015.08.087, 2015.

Kelly, F. J.: Oxidative stress: its role in air pollution and adverse health effects, Occup.

Environ. Med., 60(8), 612–616, doi:10.1136/oem.60.8.612, 2003.

Kim, S., Dutton, S. J., Sheppard, L., Hannigan, M. P., Miller, S. L., Milford, J. B., Peel, J. L. and Vedal, S.: The short-term association of selected components of fine particulate matter and mortality in the Denver Aerosol Sources and Health (DASH) study, Environ. Heal., 5–7, doi:10.1186/s12940-015-0037-4, 2015.

Kitis, M., Adams, C. D. and Daigger, G. T.: The Effects of Fenton's Reagent Pretreatment on the Biodegradability of Nonionic Surfactants, , 33(11), 2561–2568, 1999.

Kraemer, S. M.: Iron oxide dissolution and solubility in the presence of siderophores, Aquat. Sci., 66(1), 3–18, doi:10.1007/s00027-003-0690-5, 2004.

Kraft, S., Stümpel, J. and Becker, P.: High resolution x-ray absorption spectroscopy with absolute energy calibration for the determination of absorption edge energies, Rev. Sci. Instrum., 67(6), 681–687, doi:https://doi.org/10.1063/1.1146657, 1996.

Kuang, X. M., Scott, J. A., da Rocha, G. O., Betha, R., Price, D. J., Russell, L. M., Cocker, D. R. and Paulson, S. E.: Hydroxyl radical formation and soluble trace metal content in particulate matter from renewable diesel and ultra low sulfur diesel in at-sea operations of a research vessel, Aerosol Sci. Technol., 51(2), 147–158, doi:10.1080/02786826.2016.1271938, 2017.

Kulkarni, P., Chellam, S., Flanagan, J. B. and Jayanty, R. K. M.: Microwave digestion-ICP-MS for elemental analysis in ambient airborne fine particulate matter: Rare earth elements and validation using a filter borne fine particle certified reference material,

Anal. Chim. Acta, 599(2), 170–176, doi:10.1016/j.aca.2007.08.014, 2007.

Lair, A., Ferronato, C., Chovelon, J. M. and Herrmann, J. M.: Naphthalene degradation in water by heterogeneous photocatalysis: An investigation of the influence of inorganic anions, J. Photochem. Photobiol. A Chem., 193(2–3), 193–203, doi:10.1016/j.jphotochem.2007.06.025, 2008.

Landreman, A. P., Shafer, M. M., Hemming, J. C., Hannigan, M. P. and Schauer, J. J.: A Macrophage-Based Method for the Assessment of the Reactive Oxygen Species (ROS) Activity of Atmospheric Particulate Matter (PM) and Application to Routine (Daily-24 h) Aerosol Monitoring Studies, Aerosol Sci. Technol., 42(11), 946–957, doi:10.1080/02786820802363819, 2008.

Lawrence, S., Sokhi, R., Ravindra, K., Mao, H., Prain, H. D. and Bull, I. D.: Source apportionment of traffic emissions of particulate matter using tunnel measurements, Atmos. Environ., 77, 548–557, doi:10.1016/j.atmosenv.2013.03.040, 2013.

Le, C. and Ricard, Y.: Long-term fluxes and budget of ferric iron : implication for the redox states of the Earth's mantle and atmosphere, , 165, 197–211, 1999.

Ledakowicz, S., Miller, J. S. and Olejnik, D.: Oxidation of PAHs in water solutions by ultraviolet radiation combined with hydrogen peroxide, Int. J. Photoenergy, 1(1), 1–6, doi:10.1155/S1110662X99000100, 1999.

Li, N., Champion, W. M., Imam, J., Sidhu, D., Salazar, J. R., Majestic, B. J. and Montoya, L. D.: Evaluation of cellular effects of fine particulate matter from combustion of solid fuels used for indoor heating on the Navajo Nation using a stratified oxidative

stress response model, Atmos. Environ., 182(March), 87–96, doi:10.1016/j.atmosenv.2018.03.031, 2018.

Li, Y. and Xiang, R.: Particulate pollution in an underground car park in Wuhan, China, Particuology, 11(1), 94–98, doi:10.1016/j.partic.2012.06.010, 2013.

Liati, A., Pandurangi, S. S., Boulouchos, K., Schreiber, D. and Arroyo Rojas Dasilva, Y.: Metal nanoparticles in diesel exhaust derived by in-cylinder melting of detached engine fragments, Atmos. Environ., 101, 34–40, doi:10.1016/j.atmosenv.2014.11.014, 2015.

Lippmann, M., Frampton, M., Schwartz, J., Dockery, D., Schlesinger, R., Koutrakis, P., Froines, J., Nel, A., Finkelstein, J., Godleski, J., Kaufman, J., Koenig, J., Larson, T., Luchtel, D., Liu, L. S., Oberdörster, G., Peters, A., Sarnat, J., Sioutas, C., Suh, H., Sullivan, J., Utell, M., Wichmann, E. and Zelikoff, J.: The U . S . Environmental Protection Agency Particulate Matter Health Effects Research Centers Program : A Midcourse Report of Status , Progress , and Plans, , (8), 1074–1092, doi:10.1289/ehp.5750, 2003.

Lough, G. C., Schauer, J. J., Park, J. S., Shafer, M. M., Deminter, J. T. and Weinstein, J. P.: Emissions of metals associated with motor vehicle roadways, Environ. Sci. Technol., 39(3), 826–836, doi:10.1021/es048715f, 2005.

Lundstedt, S., Persson, Y. and Öberg, L.: Transformation of PAHs during ethanol-Fenton treatment of an aged gasworks' soil, Chemosphere, 65(8), 1288–1294, doi:10.1016/j.chemosphere.2006.04.031, 2006.

Luo, C., Mahowald, N. M., Meskhidze, N., Chen, Y., Siefert, R. L., Baker, A. R. and

Johansen, A. M.: Estimation of iron solubility from observations and a global aerosol model, J. Geophys. Res. Atmos., 110(23), 1–23, doi:10.1029/2005JD006059, 2005.

Luo, C., Mahowald, N., Bond, T., Chuang, P. Y., Artaxo, P., Siefert, R., Chen, Y. and Schauer, J.: Combustion iron distribution and deposition, Global Biogeochem. Cycles, 22(GB1012), doi:10.1029/2007GB002964, 2008.

Mackie, D. S., Boyd, P. W., Hunter, K. A. and McTainsh, G. H.: Simulating the cloud processing of iron in Australian dust: pH and dust concentration, Geophys. Res. Lett., 32(6), 1–4, doi:10.1029/2004GL022122, 2005.

Mahowald, N. M., Baker, A. R., Bergametti, G., Brooks, N., Duce, R. A., Jickells, T. D., Kubilay, N., Prospero, J. M. and Tegen, I.: Atmospheric global dust cycle and iron inputs to the ocean, Global Biogeochem. Cycles, 19(4), doi:10.1029/2004GB002402, 2005.

Mahowald, N. M., Engelstaedter, S., Luo, C., Sealy, A., Artaxo, P., Benitez-Nelson, C., Bonnet, S., Chen, Y., Chuang, P. Y., Cohen, D. D., Dulac, F., Herut, B., Johansen, A. M., Kubilay, N., Losno, R., Maenhaut, W., Paytan, A., Prospero, J. M., Shank, L. M. and Siefert, R. L.: Atmospheric iron deposition: global distribution, variability, and human perturbations., Ann. Rev. Mar. Sci., 245–278, doi:10.1146/annurev.marine.010908.163727, 2009.

Majestic, B. J., Schauer, J. J., Shafer, M. M., Turner, J. R., Fine, P. M., Singh, M. and Sioutas, C.: Development of a wet-chemical method for the speciation of iron in atmospheric aerosols, Environ. Sci. Technol., 40(7), 2346–2351, doi:10.1021/es052023p, 2006.

Majestic, B. J., Schauer, J. J. and Shafer, M. M.: Application of synchrotron radiation for measurement of iron red-ox speciation in atmospherically processed aerosols, Atmos. Chem. Phys. Atmos. Chem. Phys., 7(Iii), 2475–2487, doi:10.5194/acpd-7-1357-2007, 2007.

Majestic, B. J., Anbar, A. D. and Herckes, P.: Elemental and iron isotopic composition of aerosols collected in a parking structure, Sci. Total Environ., 407(18), 5104–5109, doi:10.1016/j.scitotenv.2009.05.053, 2009.

Marcus, M. A., Macdowell, A. A., Celestre, R., Manceau, A., Miller, T., Padmore, H. A. and Sublett, R. E.: Beamline 10.3.2 at ALS: a hard X-ray microprobe for environmental and materials sciences, J. Synchrotron Radiat., 11, 239–247, doi:10.1107/S0909049504005837, 2004.

Marcus, M. A., Westphal, A. J. and Fakra, S. C.: Classification of Fe-bearing species from K-edge XANES data using two-parameter correlation plots, J. Synchrotron Radiat., 15(5), 463–468, doi:10.1107/S0909049508018293, 2008.

May, A. A., Nguyen, N. T., Presto, A. A., Gordon, T. D., Lipsky, E. M., Karve, M., Gutierrez, A., Robertson, W. H., Zhang, M., Brandow, C., Chang, O., Chen, S., Cicero-Fernandez, P., Dinkins, L., Fuentes, M., Huang, S. M., Ling, R., Long, J., Maddox, C., Massetti, J., McCauley, E., Miguel, A., Na, K., Ong, R., Pang, Y., Rieger, P., Sax, T., Truong, T., Vo, T., Chattopadhyay, S., Maldonado, H., Maricq, M. M. and Robinson, A. L.: Gas- and particle-phase primary emissions from in-use, on-road gasoline and diesel vehicles, Atmos. Environ., 88, 247–260, doi:10.1016/j.atmosenv.2014.01.046, 2014.

Moore, J. K. and Abbott, M. R.: Surface chlorophyll concentrations in relation to the Antarctic Polar Front: Seasonal and spatial patterns from satellite observations, J. Mar. Syst., 37(1–3), 69–86, doi:10.1016/S0924-7963(02)00196-3, 2002.

Neyens, E. and Baeyens, J.: A review of classic Fenton's peroxidation as an advanced oxidation technique, J. Hazard. Mater., B98, 33–50, doi:10.1016/S0043-1354(02)00461-X, 2003a.

Neyens, E. and Baeyens, J.: A review of classic Fenton's peroxidation as an advanced oxidation technique, J. Hazard. Mater., 98(1–3), 33–50, doi:10.1016/S0304-3894(02)00282-0, 2003b.

Nidheesh, P. V. and Gandhimathi, R.: Degradation of dyes from aqueous solution by Fenton processes : a review, , 2099–2132, doi:10.1007/s11356-012-1385-z, 2013.

Norbeck, J. M., Durbin, T. D. and Truex, T. J.: Measurement of primary particulate matter emissions from light-duty motor vehicles, Riverside., 1998.

Oakes, M., Weber, R. J., Lai, B., Russell, A. and Ingall, E. D.: Characterization of iron speciation in urban and rural single particles using XANES spectroscopy and micro X-ray fluorescence measurements: Investigating the relationship between speciation and fractional iron solubility, Atmos. Chem. Phys., 12(2), 745–756, doi:10.5194/acp-12-745-2012, 2012a.

Oakes, M., Ingall, E. D., Lai, B., Shafer, M. M., Hays, M. D., Liu, Z. G., Russell, A. G. and Weber, R. J.: Iron solubility related to particle sulfur content in source emission and ambient fine particles, Environ. Sci. Technol., 46(12), 6637–6644,

doi:10.1021/es300701c, 2012b.

Paris, R. and Desboeufs, K. V.: Effect of atmospheric organic complexation on iron-bearing dust solubility, Atmos. Chem. Phys., 13(9), 4895–4905, doi:10.5194/acp-13-4895-2013, 2013.

Paris, R., Desboeufs, K. V., Formenti, P., Nava, S. and Chou, C.: Chemical characterisation of iron in dust and biomass burning aerosols during AMMA-SOP0/DABEX: Implication for iron solubility, Atmos. Chem. Phys., 10(9), 4273–4282, doi:10.5194/acp-10-4273-2010, 2010.

Paris, R., Desboeufs, K. V. and Journet, E.: Variability of dust iron solubility in atmospheric waters: Investigation of the role of oxalate organic complexation, Atmos. Environ., 45(36), 6510–6517, doi:10.1016/j.atmosenv.2011.08.068, 2011.

Park, S., Nam, H., Chung, N., Park, J.-D. and Lim, Y.: The role of iron in reactive oxygen species generation from diesel exhaust particles, Toxicol. Vitr., 20(6), 851–857, doi:10.1016/j.tiv.2005.12.004, 2006.

Pehkonen, S. O., Siefert, R., Erel, Y., Webb, S. and Hoffmann, M. R.: Photoreduction of Iron Oxyhydroxides in the Presence of Important Atmospheric Organic Compounds, Environ. Sci. Technol., 27(10), 2056–2062, doi:10.1021/es00047a010, 1993.

Petroselli, C., Moroni, B., Crocchianti, S., Selvaggi, R., Vivani, R., Soggia, F., Grotti, M., Acapito, F. and Cappelletti, D.: Iron Speciation of Natural and Anthropogenic Dust by Spectroscopic and Chemical Methods, Atmosphere (Basel)., 10(8), doi:10.3390/atmos10010008, 2018.

Phenrat, T., Long, T., Gregory, L. and Veronesi, B.: Partial Oxidation (“ Aging ”) and Surface Modification Decrease the Toxicity of Nanosized Zerovalent Iron, Environ. Sci. Technol., 42, 195–200, 2009.

Pignatello, J. J., Oliveros, E. and MacKay, A.: Advanced oxidation processes for organic contaminant destruction based on the fenton reaction and related chemistry, Crit. Rev. Environ. Sci. Technol., 36(1), 1–84, doi:10.1080/10643380500326564, 2006.

Prahalad, A. K., Inmon, J., Dailey, L. A., Madden, M. C., Ghio, A. J. and Gallagher, J. E.: Air Pollution Particles Mediated Oxidative DNA Base Damage in a Cell Free System and in Human Airway Epithelial Cells in Relation to Particulate Metal Content and Bioreactivity, , 879–887, doi:10.1021/tx010022e, 2001.

Rigg, T., Taylor, W. and Weiss, J.: The Rate Constant of the Reaction between Hydrogen Peroxide and Ferrous Ions, , 575(22), doi:10.1063/1.1740127, 1954.

Rubio-Clemente, A., Torres-Palma, R. A. and Peñuela, G. A.: Removal of polycyclic aromatic hydrocarbons in aqueous environment by chemical treatments: A review, Sci. Total Environ., 478, 201–225, doi:10.1016/j.scitotenv.2013.12.126, 2014.

Salazar, J. R., Cartledge, B. T., Haynes, J. P., York-Marini, R., L, A. R., Drozd, G. T., Goldstein, A. H., Fakra, S. C. and Majestic, B. J.: Water-soluble iron correlation to primary speciated organics in low-emitting vehicle exhaust, , doi:https://doi.org/10.5194/acp-2019-386, 2019.

Salazar, J. R., Cartledge, B. T., Haynes, J. P., York-marini, R., Robinson, A. L., Drozd, G. T., Goldstein, A. H., Fakra, S. C. and Majestic, B. J.: Water-soluble iron emitted from

vehicle exhaust is linked to primary speciated organic compounds, , 1849–1860, 2020.

Saliba, G., Saleh, R., Zhao, Y., Presto, A. A., Lambe, A. T., Frodin, B., Sardar, S., Maldonado, H., Maddox, C., May, A. A., Drozd, G. T., Goldstein, A. H., Russell, L. M., Hagen, F. and Robinson, A. L.: Comparison of Gasoline Direct-Injection (GDI) and Port Fuel Injection (PFI) Vehicle Emissions: Emission Certification Standards, Cold-Start, Secondary Organic Aerosol Formation Potential, and Potential Climate Impacts, Environ. Sci. Technol., 51(11), 6542–6552, doi:10.1021/acs.est.6b06509, 2017.

Santos, D. S. S., Korn, M. G. A., Guida, M. A. B., Santos, G. L. dos, Lemos, V. A. and Teixeira, L. S. G.: Determination of copper, iron, lead and zinc in gasoline by sequential multi-element flame atomic absorption spectrometry after solid phase extraction, J. Braz. Chem. Soc., 22(3), 552–557 [online] Available from: http://www.scielo.br/pdf/jbchs/v22n3/v22n3a20.pdf%0Ahttp://www.scielo.br/scielo.php?script=sci_arttext&pid=S0103-50532011000300020&lng=en&nrm=iso&tlng=en, 2011.

Scaramboni, C., Urban, R. C., Lima-souza, M., Nogueira, R. F. P., Cardoso, A. A., Allen, A. G. and Campos, M. L. A. M.: Total sugars in atmospheric aerosols : An alternative tracer for biomass burning, Atmos. Environ., 100, 185–192, doi:10.1016/j.atmosenv.2014.11.003, 2015.

Schauer, J. J., Kleeman, M. J., Cass, G. R. and Simoneit, B. R. T.: Measurement of emissions from air pollution sources. 5. C1-C32 organic compounds from gasoline-powered motor vehicles., Environ. Sci. Technol., 36(6), 1169–1180, doi:10.1021/es0108077, 2002.

Sedwick, P. N., Sholkovitz, E. R. and Church, T. M.: Impact of anthropogenic combustion emissions on the fractional solubility of aerosol iron: Evidence from the Sargasso Sea, Geochemistry, Geophys. Geosystems, 8(10), doi:10.1029/2007GC001586, 2007.

See, S. W., Wang, Y. H. and Balasubramanian, R.: Contrasting reactive oxygen species and transition metal concentrations in combustion aerosols, , 103, 317–324, doi:10.1016/j.envres.2006.08.012, 2007.

Shi, Z., Krom, M. D., Jickells, T. D., Bonneville, S., Carslaw, K. S., Mihalopoulos, N., Baker, A. R. and Benning, L. G.: Impacts on iron solubility in the mineral dust by processes in the source region and the atmosphere: A review, Aeolian Res., 5, 21–42, doi:10.1016/j.aeolia.2012.03.001, 2012.

Sholkovitz, E. R., Sedwick, P. N. and Church, T. M.: Influence of anthropogenic combustion emissions on the deposition of soluble aerosol iron to the ocean: Empirical estimates for island sites in the North Atlantic, Geochim. Cosmochim. Acta, 73(14), 3981–4003, doi:10.1016/j.gca.2009.04.029, 2009.

Sholkovitz, E. R., Sedwick, P. N., Church, T. M., Baker, A. R. and Powell, C. F.: Fractional solubility of aerosol iron: Synthesis of a global-scale data set, Geochim. Cosmochim. Acta, 89, 173–189, doi:10.1016/j.gca.2012.04.022, 2012.

Simoneit, B. R. T., Kobayashi, M., Kawamura, K., Rushdi, A. I., Rogge, W. F. and Didyk, B. M.: Sugars s Dominant Water-Soluble Organic Compounds in Soils and Characterization as Tracers in Atmospheric Particulate Matter, , 5939–5949,

doi:10.1021/es0403099, 2004.

Stumm, W. and Morgan, J. J.: Aquatic Chemistry: Chemical Equilibria and Rates in Natural Waterse, 3rd ed., Wiley-Interscience., 1996.

Tagliabue, A., Bowie, A. R., Philip, W., Buck, K. N., Johnson, K. S. and Saito, M. A.: The integral role of iron in ocean biogeochemistry, Nat. Publ. Gr., 543(7643), 51–59, doi:10.1038/nature21058, 2017.

Takahashi, Y., Higashi, M., Furukawa, T. and Mitsunobu, S.: and Physics Change of iron species and iron solubility in Asian dust during the long-range transport from western China to Japan, , 11237–11252, doi:10.5194/acp-11-11237-2011, 2011.

Teixeira, L. S. G., Rocha, R. B. S., Sobrinho, E. V., Guimarães, P. R. B., Pontes, L. A. M. and Teixeira, J. S. R.: Simultaneous determination of copper and iron in automotive gasoline by X-ray fluorescence after pre-concentration on cellulose paper, Talanta, 72(3), 1073–1076, doi:10.1016/j.talanta.2006.12.042, 2007.

Theodosi, C., Panagiotopoulos, C., Nouara, A., Zarmpas, P., Nicolaou, P. and Violaki, K.: Progress in Oceanography Sugars in atmospheric aerosols over the Eastern Mediterranean, Prog. Oceanogr., 163(July 2016), 70–81, doi:10.1016/j.pocean.2017.09.001, 2018.

Upadhyay, N., Majestic, B. J. and Herckes, P.: Solubility and speciation of atmospheric iron in buffer systems simulating cloud conditions, Atmos. Environ., 45(10), 1858–1866, doi:10.1016/j.atmosenv.2011.01.010, 2011.

Valavanidis, A., Salika, A. and Theodoropoulou, A.: Generation of hydroxyl radicals by urban suspended particulate air matter . The role of iron ions, , 34, 2379–2386, 2000.

Vedal, S., Hannigan, M. P., Dutton, S. J., Miller, S. L., Milford, J. B., Rabinovitch, N., Kim, S. and Sheppard, L.: The Denver Aerosol Sources and Health (DASH) study : Overview and early findings, Atmos. Environ., 43(9), 1666–1673, doi:10.1016/j.atmosenv.2008.12.017, 2009.

Verma, V., Fang, T., Guo, H., King, L., Bates, J. T., Peltier, R. E., Edgerton, E., Russell, A. G. and Weber, R. J.: Reactive oxygen species associated with water-soluble PM2.5 in the southeastern United States: Spatiotemporal trends and source apportionment, Atmos. Chem. Phys., 14(23), 12915–12930, doi:10.5194/acp-14-12915-2014, 2014.

Vile, G. F., Winterbourn, C. C. and Sutton, H. C.: Radical-driven fenton reactions: Studies with paraquat, adriamycin, and anthraquinone 6-sulfonate and citrate, ATP, ADP, and pyrophosphate iron chelates, Arch. Biochem. Biophys., 259(2), 616–626, doi:10.1016/0003-9861(87)90528-5, 1987.

Walling, C. and Goosen, A.: Mechanism of the Ferric Ion Catalyzed Decomposition of Hydrogen Peroxide . Effect of Organic Substrates, , 595(12), 2987–2991, doi:10.1021/ja00790a042, 1963.

Wang, Y. and Cappellen, P. V. A. N.: A multicomponent reactive transport model of early diagenesis : Application to redox cycling in coastal marine sediments, , 60(16), 2993–3014, 1996.

Wang, Y., Arellanes, C. and Paulson, S. E.: Hydrogen peroxide associated with ambient

fine-mode, diesel, and biodiesel aerosol particles in Southern California, Aerosol Sci. Technol., 46(4), 394–402, doi:10.1080/02786826.2011.633582, 2012.

Xie, M., Hannigan, M. P., Dutton, S. J., Milford, J. B., Hemann, J. G., Miller, S. L., Schauer, J. J., Peel, J. L. and Vedal, S.: Positive matrix factorization of PM2.5: Comparison and implications of using different speciation data sets, Environ. Sci. Technol., 46(21), 11962–11970, doi:10.1021/es302358g, 2012.

Zhao, Y., Nguyen, N. T., Presto, A. A., Hennigan, C. J., May, A. A. and Robinson, A. L.: Intermediate Volatility Organic Compound Emissions from On-Road Diesel Vehicles: Chemical Composition, Emission Factors, and Estimated Secondary Organic Aerosol Production, Env. Sci. Tech., 49, 11516–11526, doi:10.1021/acs.est.5b02841, 2015.

Zhao, Y., Nguyen, N. T., Presto, A. A., Hennigan, C. J., May, A. A. and Robinson, A. L.: Intermediate Volatility Organic Compound Emissions from On-Road Gasoline Vehicles and Small Off-Road Gasoline Engines., Environ. Sci. Technol., 50, 4554–4563, doi:10.1021/acs.est.5b06247, 2016.

Zhu, X., Prospero, J. M., Savoie, D. L., Millero, F. J., Zika, R. G. and Saltzman, E. S.: Photoreduction of iron(III) in marine mineral aerosol solutions, J. Geophys. Res. Atmos., 98(D5), 9039–9046, doi:10.1029/93JD00202, 1993.

Appendix A

Figure A1: Linear correlation plots representing EF in mg kg-fuel^{-1} for sulfate, organic carbon (OC), CO_2 and EF in µg kg-fuel^{-1} for water-souluble iron. Correlation lines and R^2 values for all elements are shown.

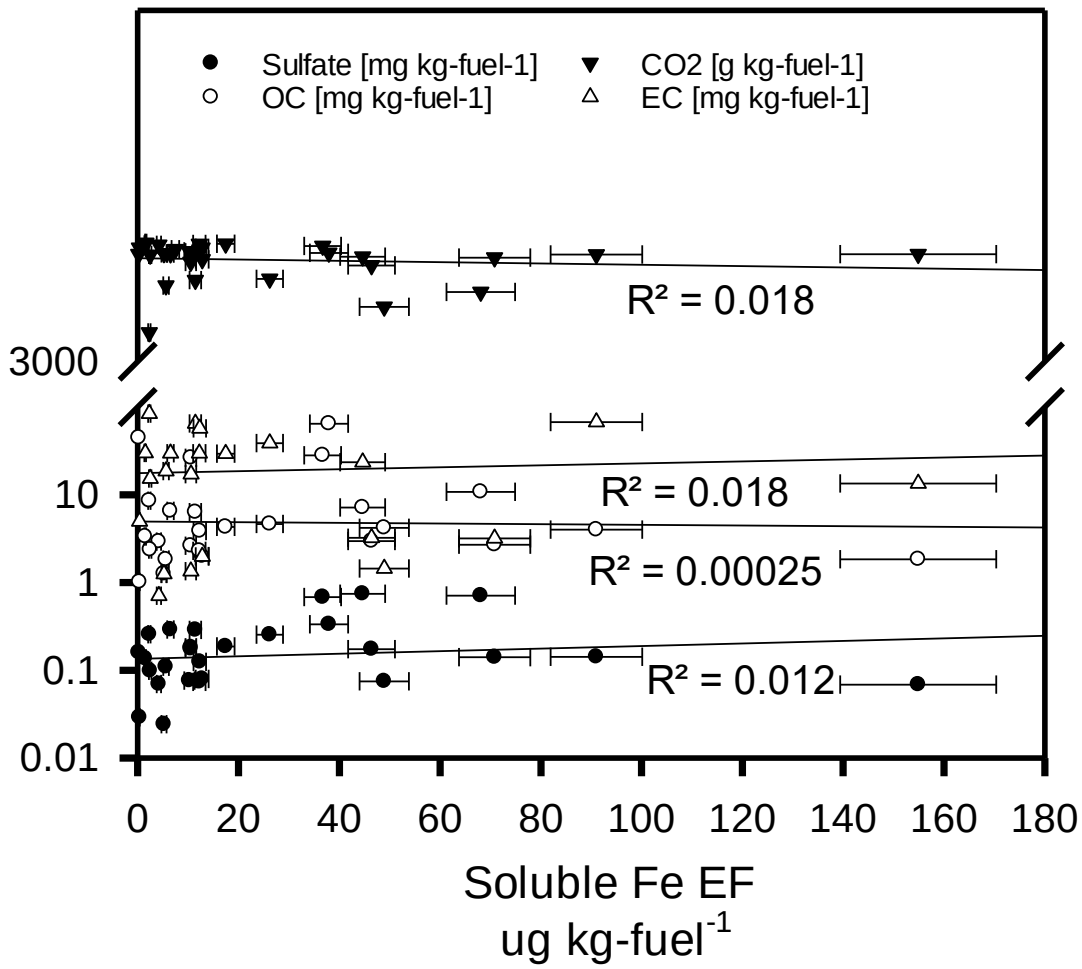

Figure A2: Linear correlation plots representing EF in µg kg-fuel^{-1} for water-souluble iron and total iron. Correlation lines and R^2 shown.

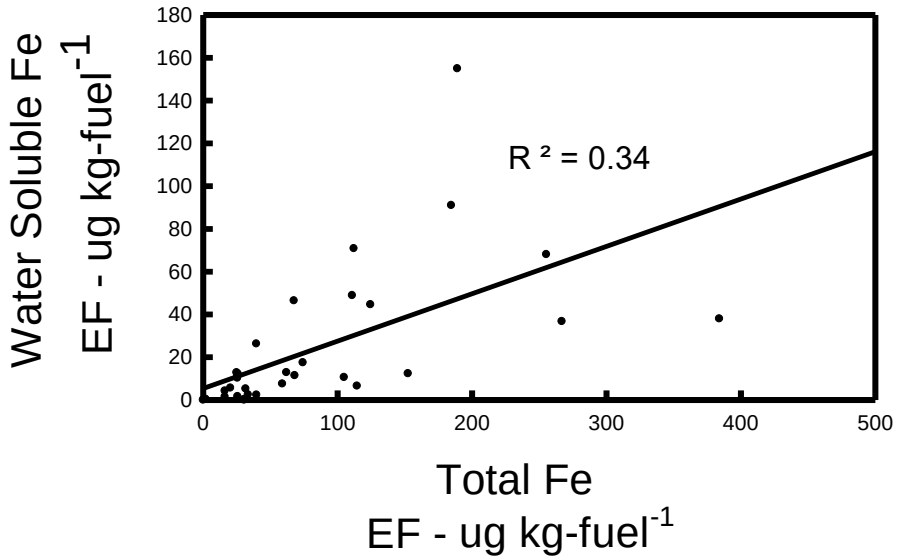

Figure A3: Water-soluble irons correlation to organic species. (M = methyl, E = Ethyl, CY = Cyclo)

Organic Name	Relationship to water-soluble iron (R^2)
(1-ME)benzene	0.06
(1-Mpropyl)benzene	0.04
(2-Mpropyl)benzene	0.00
1,2,3,4-tetraMbenzene	0.04
1,2,3,5-tetraMbenzene	0.04
1,2,3-triMbenzene	0.05
1,2,4,5-tetraMbenzene	0.06
1,2,4-triMCYpentane	0.03
1,2,4-triMbenzene	0.07
1,2-butadiene	0.04
1,2-diEbenzene	0.03
1,2-diM-3-Ebenzene	0.03
1,2-diM-4-Ebenzene	0.06
1,2-propadiene	0.01
1,3,5-triMCYhexane	0.07
1,3,5-triMbenzene	0.09
1,3-CYpentadiene	0.00
1,3-butadiene	0.03
1,3-butadiyne	0.00
1,3-di-npropylbenzene	0.02
1,3-diEbenzene	0.08
1,3-diM-2-Ebenzene	0.00
1,3-diM-4-Ebenzene	0.05
1,3-diM-5-Ebenzen e	0.05
1,4-diEbenzene	0.03
1,4-diM-2-Ebenzene	0.07
1-(diME)-2-Mbenzene	0.00
1-(diME)-3,5-diMbenzene	0.03
1-E-2-npropylbenzene	0.03
1-E-tertbutylether	0.00
1-M-2-(1-ME)benzene	0.04
1-M-2-Ebenzene	0.05
1-M-2-n-butylbenzene	0.10
1-M-2-n-propylbenzene	0.05
1-M-3-(1-ME)benz ene	0.04

1-M-3-Ebenzene	0.08
1-M-3-n-propylbenzene	0.05
1-M-4-(1-ME)benzene	0.03
1-M-4-ECYhexane	0.38
1-M-4-Ebenzene	0.07
1-M-4-n-propylbenzene	0.05
1-MCYpentene	0.00
1-buten-3-yne	0.15
1-butene	0.07
1-butyne	0.00
1-heptene	0.00
1-hexene	0.01
1-nonene	0.03
1-octene	0.00
1-pentene	0.04
1-propyne	0.00
1a,2a,3b-triMCYpentane	0.07
2,2,3-triMbutane	0.15
2,2,4-triMheptane	0.03
2,2,4-triMhexane	0.04
2,2,4-triMpentane	0.00
2,2,5-triMheptane	0.05
2,2,5-triMhexane	0.01
2,2-diM-octane	0.02
2,2-diMhexane	0.00
2,2-diMpentane	0.02
2,2-diMpropane	0.00
2,3,3-triMpentane	0.00
2,3,4-triMpentane	0.04
2,3,5-triMhexane	0.04
2,3-diM-1-butene	0.06
2,3-diM-2-pentene	0.01
2,3-diM-octane	0.00
2,3-diMbutane	0.02
2,3-diMheptane	0.01
2,3-diMhexane	0.08
2,3-diMpentane	0.03
2,4,4-triM-1-pentene	0.01
2,4,4-triM-2-pentene	0.31
2,4,4-triMhexane	0.07

2,4-diM-1-pentene	0.01
2,4-diM-2-pentene	0.00
2,4-diM-octane	0.01
2,4-diMheptane	0.07
2,4-diMhexane	0.04
2,4-diMpentane	0.04
2,5-diM-octane	0.05
2,5-diMhexane	0.04
2,6-diM-octane	0.00
2,6-diMheptane	0.01
2-M-1,3-butadiene	0.16
2-M-1-butene	0.11
2-M-1-pentene	0.12
2-M-2-butene	0.20
2-M-2-hexene	0.05
2-M-2-pentene	0.12
2-M-indan	0.05
2-M-octane	0.00
2-M-t-3-hexene	0.06
2-Mbutane	0.01
2-Mheptane	0.04
2-Mhexane	0.04
2-Mnonane	0.05
2-Mpentane	0.03
2-Mpropene	0.06
2-butyne	0.00
3,3-diM-1-butene	0.00
3,3-diM-octane	0.05
3,3-diMhexane	0.58
3,3-diMpentane	0.01
3,4-diM-1-pentene	0.03
3,4-diMhexane	0.03
3,5-diMheptane	0.06
3-E-2-pentene	0.05
3-Epentane	0.04
3-M-1-butene	0.06
3-M-1-hexene	0.00
3-M-1-pentene	0.01
3-M-c-2-hexene	0.25
3-M-c-2-pentene	0.00

3-Moctane	0.05
3-M-t-2-pentene	0.55
3-M-t-3-hexene	0.01
3-MCYpentene	0.02
3-Mheptane	0.03
3-Mhexane	0.04
3-Mpentane	0.02
4-M-1-pentene	0.01
4-M-c-2-pentene	0.00
4-M-indan	0.03
4-M-octane	0.06
4-M-t-2-hexene	0.01
4-M-t-2-pentene	0.05
4-Mheptane	0.04
5-M-indan	0.08
CYhexane	0.00
CYhexene	0.04
CYpentane	0.02
CYpentene	0.18
ECYhexane	0.10
ECYpentane	0.05
Ebenzene	0.09
Ethane	0.00
M-tertbutyl-ether	0.00
MCYhexane	0.02
MCYpentane	0.03
MEketone	0.00
Methane	0.00
Mpropane	0.00
acetaldehyde	0.03
acetone	0.06
acrolein	0.02
benzaldehyde	0.02
benzene	0.09
butyraldehyde	0.03
c-1,2-diMCYhexane	0.19
c-1,3-diMCYhexane	0.04
c-1,3-diMCYpentane	0.03
c-1-M-3-ECYpentane	0.00
c-2-butene	0.10

c-2-heptene	0.01
c-2-hexene	0.10
c-2-octene	0.02
c-2-pentene	0.04
c-3-hexene	0.16
crotonaldehdye	0.00
ethanol	0.06
ethene	0.07
ethyne	0.01
formaldehyde	0.04
hexanal	0.00
indan	0.10
m-tolualdehyde	0.01
m-xylene	0.07
methacrolein	0.03
methanol	0.00
n-butane	0.00
n-decane	0.02
n-dodecane	0.02
n-heptane	0.05
n-hexane	0.03
n-nonane	0.04
n-octane	0.04
n-pentane	0.01
n-pentylbenzene	0.03
n-propylbenzene	0.05
n-undecane	0.04
o-xylene	0.07
p-xylene	0.07
propane	0.01
propene	0.06
propionaldehyde	0.08
styrene	0.04
t-1,2-diMCYpentane	0.04
t-1,3-diMCYhexane	0.04
t-1,3-diMCYpentane	0.05
t-1,3-pentadiene	0.00
t-1,4-diMCYhexane	0.04
t-1-M-3-ECYpentane	0.05
t-2-butene	0.07
t-2-heptene	0.06

t-2-hexene	0.03
t-2-octene	0.08
t-2-pentene	0.04
t-3-heptene	0.10
t-3-hexene	0.02
t-4-octene	0.48
toluene	0.08
valeraldehyde	0.04

Figure A4: Results of Least-square linear combination fitting (LCF) of Fe K-edge XANES. Spectra were fitted in the range 7090 to 7365 eV.

Sample	%	Component 1	%	Component 2	%	Component 3	Sum	*NSS* x10^{-4}
1	50	Biogenic FeIII oxyhy	32	Maghemite	18	NKT-1g basalt glass	100	0.74
2	59	FeIII sulfate	31	Biogenic Fe(III) oxyhy	10	Almandine	100	1.28
4	63	Hematite	14	Pigeonite	23	Roedderite	100	1.2
5	26	Coalingite	61	Hematite	13	Maghemite	100	1.06
6	49	FeIII dextran	14	Kaolinite	37	Lepidocrocite	100	0.7
7	19	FeIII sulfate	20	FeIII dextran	61	Ferrihydrite_2L	100	0.49
8	41	FeIII dextran	59	Maghemite	NA	NA	100	2.27
9	10	Almandine	83	FeIII sulfate	7	Roedderite	100	1.48
10	10	Almandine	84	Ferrihydrite_2L	6	FeSi	100	0.73
11	37	Awaruite	17	Fe3C	46	Fe3Si	100	2.07
12	25	FeIII phosphate hydrate	20	FeIII dextran	55	Ferrihydrite_2L	100	0.69
13	76	Hematite	24	Coalingite	NA	NA	100	1.59
14	56	FeIII sulfate	26	FeIII pyrophosphate	18	Goethite	100	0.94
15	28	Fe3C	33	Fe3Si	39	Aegirine	100	1.35
16	67	FeIII dextran	14	Goethite	19	Jarosite	100	1.13
17	7	Almandine	62	FeIII Kaolinite	31	Maghemite	100	1.32

Notes: Normalized sum-square value (NSS=$100\times[\sum(\mu_{exp}-\mu_{fit})^2/\sum(\mu_{exp})^2]$). Error on the percentages of species is estimated to be ±10%. Biogenic FeIII oxyhy is biogenic Fe(III) oxyhydroxide*

* Toner, B., Santelli, C. M., Marcus, M. A., Wirth, R., Chan, C. S., McCollum, T., Bach, W., Edwards, K. J. (2009) "Biogenic iron oxyhydroxide formation at mid-ocean ridge hydrothermal vents: Juan de Fuca Ridge" Geochimica et Cosmochimica Acta 73,388-403

Figure A5: Classification of Fe-bearing standards found by LCF in pseudo-mineral groups

Biogenic Fe(III) oxyhy	Fe(III) oxy+org
Maghemite	Fe(III) oxide
Basalt glass NKT-1	Fe(II) silicate
Fe(III) sulfate	Fe(III) sulfate
Almandine	Fe(II) silicate
Hematite	Fe(III) oxide
Pigeonite	Fe(II) silicate
Roedderite	Fe(II) silicate
Coalingite	Fe(III) carbonate
Fe(III) dextran	Fe(III) oxy+org
Kaolinite	Fe(III) silicate
Lepidocrocite	Fe(III) oxy+org
Ferrihydrite2L	Fe(III) oxy+org
FeSi	Native
Awaruite	Native
Fe3C	Native
Fe3Si	Native
Fe(III) pyrophosphate	Fe(III) phosphate
Goethite	Fe(III) oxy+org
Aegirine	Fe(III) silicate
Jarosite	Fe(III) sulfate

Note: “Org”: Fe(III)-organics

Figure A6: Percentage distribution of the pseudo-mineral groups

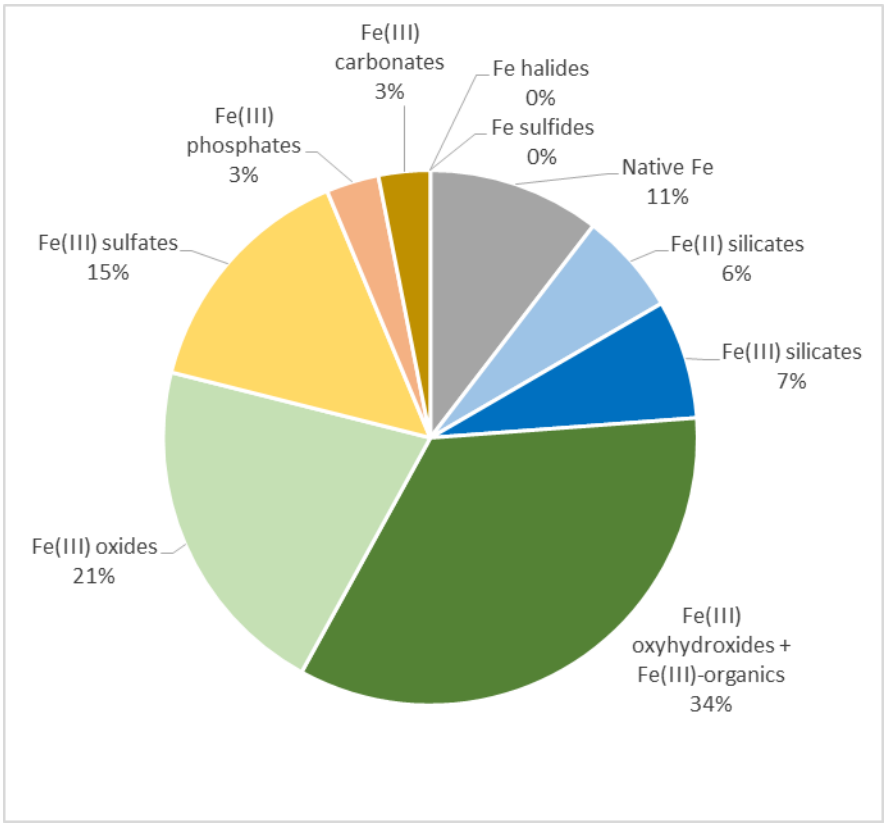

Figure A7: R^2 Values of different carbon species and their correlation to water-soluble iron.

CARBON NUMBER	ALKANE	SINGLE RING AROMATIC	POLAR
12	0.04	0.00	0.25
13	0.06	0.03	0.17
14	0.23	0.37	0.33
15	0.37	0.13	0.33
16	0.37	0.13	0.56
17	0.23	0.26	0.28
18	0.05	0.23	0.10

Figure A8: Linear correlation plots representing EF in µg kg-fuel^{-1} for water-souluble iron and vehical miles read from the vehical odometer. Correlation lines and R^2 shown.

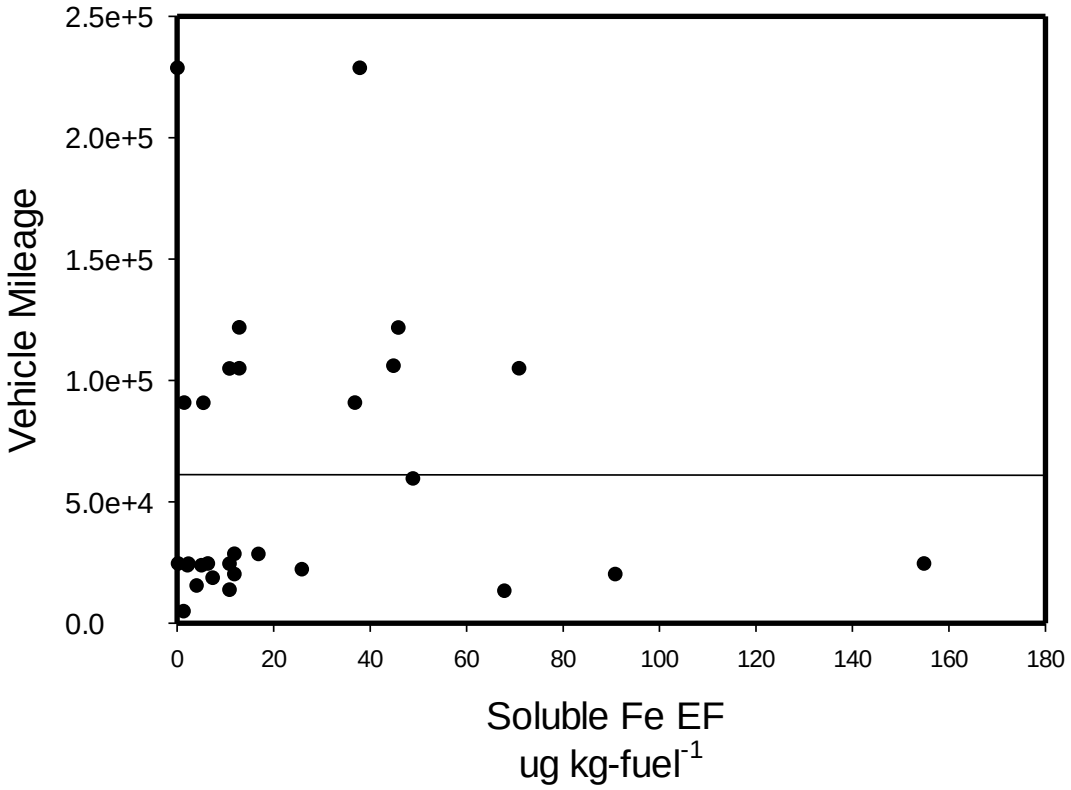

Figure A9: Table of total element for each Sample ID

Sample ID	Total Elements (µg kg-fuel^{-1}) Na	Mg	Al	K	Ca	Ca	Ti	V
1038820	23.61	4.88	11.32	-4.28	106.52	147.35	-4.21	0.72
1038821	135.33	104.47	-0.47	123.32	525.47	601.04	-1.95	-0.06
1038822	61.59	42.07	37.30	23.99	202.34	298.35	0.48	0.02
1038823	11.48	-0.83	59.28	-5.11	132.67	162.71	-2.10	0.11
1038824	62.53	7.37	30.82	63.25	243.81	286.07	4.16	-0.01
1038825	208.72	88.44	337.84	140.84	1084.76	1284.17	57.79	0.20
1038827	17.61	21.19	-3.10	4.72	270.49	71.11	-3.11	-0.07
1038862	40.76	2.77	36.03	22.01	188.50	226.65	-0.98	-0.02
1038864	52.20	48.12	-0.66	5.13	347.22	430.88	-1.57	-0.03
1038867	-8.91	1.24	42.52	3.03	147.96	248.93	-2.07	-0.06
1038883	2.14	2.79	-7.87	18.72	127.06	85.97	-1.44	0.00
1038884	243.82	69.65	327.27	24.15	708.25	803.37	7.07	-0.12
1038889	134.76	33.76	294.47	13.73	669.43	620.58	11.05	0.00
1038891	159.10	711.86	104.53	32.46	419.55	350.17	-3.71	0.01
1038901	347.60	236.77	28.37	15.29	92.45	146.81	-2.26	0.05
1038917	27.23	10.85	70.80	32.98	243.47	232.09	2.23	0.04
1038918	6.50	-3.04	13.69	-7.97	2.98	2.95	0.36	0.02
1038920	20.54	10.56	41.34	-10.98	13.91	21.32	-4.10	0.01
1038945	9.14	4.07	118.77	-5.49	213.11	151.56	0.54	-0.08
1038947	60.56	9.38	118.75	-8.49	137.01	159.58	-1.39	-0.09
1038952	47.78	57.76	23.38	39.26	365.70	313.26	-0.58	0.02
1038980	-31.58	7.76	-20.16	9.29	61.16	73.46	-4.79	-0.02

Figure A10: Table of total element for each Sample ID

Sample ID	Total Elements (µg kg-fuel^{-1})								
	Cr	**Mn**	**Fe**	**Co**	**Ni**	**Cu**	**Zn**	**As**	**Se**
1038820	5.73	0.68	58.89	1.12	12.12	1.67	-73.50	0.02	1.68
1038821	0.29	1.27	20.29	0.00	-0.23	2.85	271.29	0.01	-0.16
1038822	8.29	3.80	184.63	0.11	1.22	152.97	92.29	0.02	-0.25
1038823	2.67	7.04	39.71	0.01	4.43	4.91	-27.56	0.01	-0.09
1038824	4.54	1.76	104.84	0.01	1.58	11.74	50.51	0.00	-0.07
1038825	4.93	10.48	255.43	0.35	13.21	148.52	175.61	0.00	1.60
1038827	2.52	0.89	39.60	-0.01	0.35	4.36	8.60	0.00	-0.06
1038862	3.44	1.39	74.17	-0.03	1.66	3.58	44.04	0.00	-0.04
1038864	4.92	2.09	124.49	-0.01	0.28	4.43	128.32	0.03	0.57
1038867	7.44	1.76	68.12	-0.01	20.48	14.74	19.22	0.00	-0.35
1038883	2.21	0.75	16.18	-0.02	0.92	0.31	35.09	0.00	-0.29
1038884	24.80	7.17	384.00	0.50	31.80	114.43	164.41	0.00	0.34
1038889	19.85	6.56	266.92	1.25	16.83	136.32	119.65	0.01	-0.19
1038891	0.05	1.08	112.09	0.03	2.75	9.77	-20.25	0.00	-0.33
1038901	2.64	0.84	67.56	0.04	0.56	7.24	-35.28	0.00	-0.28
1038917	8.16	1.58	189.13	0.11	4.80	8.54	180.88	0.01	-0.21
1038918	1.56	0.20	33.39	-0.03	0.61	3.66	-47.71	0.00	-0.03
1038920	0.50	0.21	16.17	-0.05	1.99	1.33	-58.88	0.00	0.14
1038945	7.55	1.89	114.48	0.04	4.99	13.28	-6.80	0.00	-0.20
1038947	19.33	4.09	152.40	0.20	13.60	89.53	-32.29	0.00	-0.38
1038952	1.43	0.61	25.84	-0.01	1.17	3.08	344.40	0.02	0.04
1038980	1.75	0.61	25.45	0.83	1.33	0.23	0.35	0.00	-0.51

Figure A11: Table of total element for each Sample ID

	Total Elements (µg kg-fuel^{-1})								
Sample ID	**Rb**	**Sr**	**Mo**	**Rh**	**Pd**	**Ag**	**Cd**	**Sb**	**Cs**
1038820	-0.01	1.99	1.54	0.04	0.81	0.02	-0.10	1.02	0.01
1038821	0.09	1.42	0.74	0.01	0.38	0.02	0.30	-0.01	0.01
1038822	0.03	1.79	4.35	0.05	1.37	0.60	0.28	0.18	0.02
1038823	-0.02	0.59	2.59	0.11	1.88	0.18	-0.06	0.01	0.00
1038824	0.01	1.28	1.42	0.03	0.23	0.07	0.08	0.01	0.01
1038825	0.51	3.98	31.62	0.09	0.78	0.30	-0.03	0.62	0.02
1038827	-0.04	0.28	1.62	0.03	-0.10	0.08	0.19	-0.05	0.01
1038862	-0.03	0.49	3.50	0.13	4.84	0.00	-0.06	0.03	0.00
1038864	0.02	2.15	16.34	0.52	6.11	0.01	0.14	0.14	0.00
1038867	-0.03	1.06	4.22	0.07	1.04	-0.01	-0.04	-0.04	0.01
1038883	0.00	0.22	1.30	0.00	0.03	0.01	-0.03	0.09	0.00
1038884	0.02	2.86	22.49	0.18	2.87	1.59	-0.01	1.02	0.00
1038889	0.00	3.43	14.17	0.13	2.08	0.86	-0.01	1.08	0.00
1038891	0.13	0.57	3.19	0.01	-0.02	0.00	-0.07	0.40	0.01
1038901	0.06	0.13	1.25	0.00	-0.07	0.00	-0.02	0.17	0.01
1038917	0.00	0.87	1.36	0.01	-0.04	0.01	0.24	0.00	0.00
1038918	-0.02	0.35	0.41	0.00	0.02	-0.01	-0.06	0.01	0.00
1038920	-0.04	0.11	2.29	0.00	0.18	0.00	-0.06	0.35	0.00
1038945	-0.01	3.14	3.82	0.15	0.39	0.08	-0.03	0.04	0.00
1038947		1.62	5.88	0.03	1.24	0.02	-0.10	0.51	0.00
1038952		0.42	0.32	0.03	0.57	0.00	-0.07	0.10	0.01
1038980		0.17	1.67	0.00	-0.12	0.33	-0.15	0.22	0.02

Figure A12: Table of total element for each Sample ID

	Total Elements (µg kg-fuel^{-1})				
Sample ID	**Ba**	**Ce**	**Pt**	**Pb**	**U**
1038820	2.90	2.07	-0.01	0.35	0.00
1038821	3.25	0.53	0.00	0.69	0.00
1038822	5.94	4.18	0.01	0.83	0.00
1038823	2.65	2.01	0.01	-0.26	0.00
1038824	7.36	2.83	0.00	0.47	0.00
1038825	13.43	5.54	0.08	7.47	0.03
1038827	5.66	1.80	0.00	0.40	0.00
1038862	4.59	5.65	-0.01	0.14	0.00
1038864	4.63	5.19	0.36	0.15	0.00
1038867	5.33	2.36	0.00	0.26	0.00
1038883	2.78	0.44	-0.01	-0.03	0.00
1038884	22.55	17.51	0.22	0.93	0.00
1038889	22.29	10.46	0.09	0.86	0.01
1038891	4.31	0.22	0.00	-0.15	0.00
1038901	2.67	-0.03	-0.01	0.24	0.00
1038917	6.22	0.70	0.00	0.39	0.00
1038918	3.36	0.63	-0.01	-0.29	0.00
1038920	1.06	0.09	-0.01	-0.51	0.00
1038945	6.56	15.67	0.02	0.14	0.00
1038947	4.02	3.63	0.06	-0.02	0.00
1038952	2.44	0.48	-0.01	1.49	0.03
1038980	2.55	-0.15	-0.01	-0.04	0.00

Figure A13: Table of Soluble element for each Sample ID

Sample ID	Soluble Elements (µg kg-fuel^{-1}) Na	Mg	Al	K	Ca	Ca	Ti	V	Cr
1038820	14.78	7.02	0.96	-2.22	181.35	151.87	-0.30	0.72	0.59
1038821	125.87	20.51	-0.64	108.92	542.45	570.51	-0.06	-0.06	0.22
1038822	28.07	3.90	6.81	17.55	133.37	216.86	0.64	0.02	1.64
1038823	-6.51	0.06	7.60	-3.73	23.70	49.14	-0.15	0.11	-0.09
1038824	49.29	4.87	6.26	48.42	173.27	183.48	0.16	-0.01	0.39
1038825	141.24	60.83	59.05	53.80	962.45	1104.56	1.05	0.20	0.81
1038827	6.43	14.22	5.82	0.48	70.00	16.80	-0.03	-0.07	0.93
1038862	23.95	1.24	12.12	14.73	119.01	159.04	-0.16	-0.02	0.28
1038864	20.02	41.07	3.98	0.67	307.55	357.97	1.75	-0.03	0.36
1038867	-9.52	1.09	9.81	2.90	132.81	136.99	-0.04	-0.06	0.26
1038883	7.88	0.13	-4.85	14.22	81.95	49.25	0.27	0.00	0.33
1038884	50.06	10.97	72.94	14.87	314.60	346.70	0.18	-0.12	0.74
1038889	36.83	14.71	136.05	14.91	442.20	433.83	0.42	0.00	0.86
1038891	-41.34	8.18	27.86	28.68	294.64	273.43	0.07	0.01	1.16
1038901	-25.04	5.30	27.16	16.59	109.43	144.34	0.58	0.05	2.40
1038917	33.12	6.95	72.61	33.93	238.88	214.56	1.66	0.04	4.19
1038918	6.28	-1.60	4.09	-7.04	2.74	-1.24	0.25	0.02	-0.13
1038920	16.87	10.05	21.75	-9.24	-23.14	6.57	-0.29	0.01	-0.03
1038945	-3.20	1.59	24.22	-4.56	93.93	56.35	0.18	-0.08	0.09
1038947	2.25	2.17	33.62	-6.73	94.42	80.90	-0.22	-0.09	1.17
1038952	-36.69	6.51	15.24	19.46	177.75	159.31	0.23	0.02	1.50
1038980	-6.99	3.24	-8.85	11.66	148.02	104.65	-0.03	-0.02	0.73

Figure A14: Table of Soluble element for each Sample ID

Sample ID	Soluble Elements (µg kg-fuel^{-1}) Mn	Fe	Co	Ni	Cu	Zn	As	Se	Rb
1038820	0.56	7.47	0.36	10.66	2.28	-6.71	0.02	-0.06	0.01
1038821	1.04	5.61	-0.03	0.07	-0.05	267.76	0.01	0.06	0.06
1038822	3.10	91.03	0.04	0.81	137.05	72.18	0.02	0.09	0.00
1038823	3.81	2.30	-0.03	1.26	1.47	-9.76	0.01	-0.04	0.00
1038824	0.95	10.56	-0.02	0.78	5.87	46.52	0.00	0.11	0.03
1038825	8.14	68.07	0.18	6.74	127.39	193.62	0.00	0.31	0.12
1038827	0.62	26.20	-0.05	0.13	5.18	32.14	0.00	0.31	-0.01
1038862	0.87	17.46	-0.04	0.28	2.59	27.57	0.00	-0.04	0.01
1038864	1.56	44.63	-0.08	0.04	4.94	113.63	0.03	0.04	0.01
1038867	1.20	11.43	-0.04	0.43	1.88	18.25	0.00	-0.05	-0.01
1038883	0.47	4.20	-0.06	0.21	0.85	13.94	0.00	-0.04	0.02
1038884	2.91	37.93	0.22	9.27	42.42	75.00	0.00	-0.04	0.00
1038889	4.45	36.68	0.69	7.04	89.75	110.47	0.01	-0.03	0.01
1038891	0.73	70.80	0.00	1.42	4.75	20.33	0.00	-0.04	0.03
1038901	0.55	46.40	0.01	0.24	7.94	6.34	0.00	-0.04	0.06
1038917	1.17	154.89	0.03	2.74	7.89	147.07	0.01	-0.03	0.03
1038918	0.06	2.46	-0.05	-0.05	1.83	-18.78	0.00	-0.03	-0.01
1038920	0.04	1.48	-0.07	0.62	0.47	-12.81	0.00	0.47	0.01
1038945	0.67	6.49	-0.02	1.07	5.48	0.29	0.00	-0.03	-0.01
1038947	1.76	12.31	-0.02	1.91	73.20	8.94	0.00	-0.05	-0.01
1038952	0.20	12.21	-0.03	0.17	3.62	139.72	0.02	0.28	0.04
1038980	0.31	10.25	0.38	0.02	1.34	20.21	0.00	-0.07	-0.01

Figure A15: Table of Soluble element for each Sample ID

Sample ID	Soluble Elements (µg kg-fuel^{-1}) Sr	Mo	Rh	Pd	Ag	Cd	Sb	Cs	Ba
1038820	1.71	0.87	0.00	0.23	0.02	0.01	0.94	0.01	2.03
1038821	1.25	0.59	0.00	0.28	0.02	0.00	0.02	0.00	2.85
1038822	1.42	3.23	0.01	0.99	0.46	0.01	0.11	0.00	4.62
1038823	0.29	1.22	0.00	0.11	0.00	0.01	0.01	0.00	1.89
1038824	0.80	0.66	0.00	0.01	0.04	0.00	0.00	0.00	3.27
1038825	2.68	27.72	0.01	0.18	0.11	0.04	0.18	0.02	9.56
1038827	0.13	1.24	0.00	0.00	0.08	0.01	0.00	0.00	5.08
1038862	0.46	2.18	0.05	2.25	0.01	-0.01	-0.02	0.00	3.39
1038864	1.58	12.72	0.11	3.93	0.02	-0.02	0.03	0.00	4.08
1038867	0.91	2.84	0.01	0.39	-0.01	0.00	-0.01	0.00	4.52
1038883	0.15	0.87	0.00	0.08	0.00	0.01	0.07	0.00	2.08
1038884	1.12	6.00	0.00	0.12	0.06	0.03	0.41	0.00	9.26
1038889	2.38	6.56	0.00	0.20	0.08	0.05	0.51	0.00	16.93
1038891	0.46	2.69	0.00	0.06	0.01	0.01	0.36	0.00	4.04
1038901	0.13	0.87	0.00	0.00	0.00	0.05	0.01	0.01	2.52
1038917	0.73	0.71	0.00	0.01	0.01	0.01	0.01	0.00	5.43
1038918	0.18	0.06	0.00	0.00	0.00	-0.01	-0.01	0.00	1.47
1038920	0.05	1.07	0.00	0.05	0.00	0.04	0.09	0.00	0.60
1038945	1.47	1.46	0.00	0.01	0.04	0.01	0.00	0.00	3.40
1038947	0.37	2.63	0.00	0.02	0.00	0.00	0.06	0.00	2.82
1038952	0.27	0.23	0.01	0.17	0.00	0.00	-0.01	0.01	1.45
1038980	0.11	0.60	0.00	0.00	-0.01	-0.01	-0.02	0.00	2.22

Figure A16: Table of Soluble element for each Sample ID

Sample ID	Soluble Elements (µg kg-fuel^{-1}) Ce	Pt	Pb	U
1038820	0.23	0.00	0.71	0.00
1038821	0.13	0.00	0.64	0.00
1038822	0.76	0.01	0.52	0.00
1038823	0.14	0.00	-0.10	0.00
1038824	0.11	0.00	0.19	0.00
1038825	1.89	0.01	7.01	0.02
1038827	0.29	0.00	0.29	0.00
1038862	0.56	0.00	0.06	0.00
1038864	0.60	0.11	0.00	0.00
1038867	0.21	0.00	0.08	0.00
1038883	0.24	0.00	0.06	0.00
1038884	0.66	0.00	0.21	0.00
1038889	1.55	0.00	0.37	0.00
1038891	0.19	0.01	0.12	0.00
1038901	0.07	0.00	0.50	0.00
1038917	0.13	0.00	0.19	0.00
1038918	0.03	0.00	-0.12	0.00
1038920	0.00	0.00	-0.18	0.00
1038945	0.87	0.00	0.00	0.00
1038947	0.19	0.00	-0.07	0.00
1038952	0.05	0.00	0.60	0.03
1038980	-0.02	0.00	0.08	0.00

Appendix B

Figure B1: Table of $PM_{2.5}$ Soluble elements and total elements for each date during PRAPPE sampling

Dates collected	$PM_{2.5}$ (ug/m^3) PM	Soluble Elements (ng/m^3) Na	Mg	Al	K	Ca
NOV 2, 4, 5, 6 2017	7.33					
NOV 27, 29, 30, 31 2017	4.16					
12/11/2016	-0.93					
12/13/2016	2.37	18.65	3.05	6.02	11.35	14.75
12/15/2016	7.02	18.44	7.71	2.38	27.58	34.93
12/17/2016	1.81	29.30	4.82	2.47	34.08	11.03
12/21/2016	-131.73	28.22	3.16	0.14	4.17	6.67
12/23/2016	102.25	108.37	6.04	1.08	44.61	23.98
2/24/2017	1.67	4.46	3.56	0.51	5.72	7.30
2/26/2017	6.39	6.79	3.21	0.94	23.03	9.49
2/28/2017	7.23	32.37	8.54	1.71	40.42	21.40
3/2/2017	1.08	5.76	3.44	0.48	7.15	10.58
3/7/2017	8.09	21.51	14.13	1.83	57.63	57.27
7/31/2017	4.97	13.83	5.32	5.33	-78.85	34.28
8/2/2017	5.68	14.92	10.22	5.15	33.06	58.60
8/6/2017	4.15	-1.62	-0.02	0.10	16.69	-1.95
8/8/2017	7.06	2.40	1.78	1.34	40.74	9.33
8/10/2017	5.59	-3.90	0.77	0.64	9.99	1.83
8/12/2017	4.81	5.81	2.01	1.01	13.01	8.28
8/14/2017	4.11	13.74	5.54	2.27	-86.14	37.43
8/18/2017	6.62	13.32	7.90	2.70	27.87	44.80
8/20/2017	9.96	25.25	11.26	3.16	32.66	60.26
8/22/2017	12.75	16.66	10.30	4.60	38.82	63.92
8/24/2017	5.32	55.98	15.27	2.59	21.89	100.95
8/26/2017	4.35	27.52	12.88	4.38	33.49	73.47
8/29/2017	12.39	5.48	105.89	18.41	110.30	776.86

Figure B2: Table of $PM_{2.5}$ Soluble elements and total elements for each date during PRAPPE sampling

	Soluble Elements (ng m^{-3})							
Dates collected	**Sc**	**Ti**	**V**	**Cr**	**Mn**	**Fe**	**Co**	**Ni**
NOV 2, 4, 5, 6 2017								
NOV 27, 29, 30, 31 2017								
12/11/2016								
12/13/2016	0.00	0.01	0.00	0.02	0.34	4.61	0.01	0.02
12/15/2016	0.00	0.02	0.02	0.03	0.97	5.34	0.01	0.02
12/17/2016	0.00	0.00	0.03	0.03	0.34	3.35	0.00	0.02
12/21/2016	0.00	0.00	0.00	0.00	0.13	0.17	0.00	0.00
12/23/2016	0.00	0.02	0.01	0.04	0.57	2.99	0.01	0.02
2/24/2017	0.00	0.01	0.01	0.01	0.21	1.08	0.00	0.01
2/26/2017	0.00	0.01	0.01	0.03	0.24	5.94	0.00	0.01
2/28/2017	0.00	0.02	0.02	0.04	0.65	8.92	0.02	0.03
3/2/2017	0.00	0.01	0.01	0.00	0.27	1.84	0.00	0.01
3/7/2017	0.00	0.02	0.03	0.06	1.23	5.57	0.02	0.03
7/31/2017	-0.01	0.04	0.01	0.03	0.68	11.48	0.00	0.05
8/2/2017	-0.01	0.12	0.03	0.06	1.24	17.51	0.01	0.04
8/6/2017	-0.02	0.00	0.00	0.04	0.04	0.14	0.00	0.02
8/8/2017	0.00	0.05	0.00	0.06	0.45	12.65	0.00	0.02
8/10/2017	-0.05	0.06	0.00	0.11	0.27	8.37	0.00	0.01
8/12/2017	-0.02	0.03	0.02	0.04	0.29	5.87	0.00	0.01
8/14/2017	-0.01	0.02	0.02	0.00	0.60	8.73	0.00	0.03
8/18/2017	-0.02	0.05	0.01	0.03	0.88	9.61	0.01	0.02
8/20/2017	-0.02	0.05	0.02	0.03	1.20	12.12	0.01	0.02
8/22/2017	-0.03	0.07	0.04	0.04	1.23	12.31	0.01	0.03
8/24/2017	-0.02	0.03	0.02	0.03	1.01	6.12	0.02	0.03
8/26/2017	-0.02	0.06	0.04	0.03	1.45	11.84	0.01	0.04
8/29/2017	121.40	135.50	0.05	0.04	2.23	20.37	0.02	0.07

Figure B3: Table of $PM_{2.5}$ Soluble elements and total elements for each date during PRAPPE sampling

	Soluble Elements (ng m^{-3})							
Dates collected	**Cu**	**Zn**	**As**	**Se**	**Rb**	**Sr**	**Mo**	**Rh**
NOV 2, 4, 5, 6 2017								
NOV 27, 29, 30, 31 2017								
12/11/2016								
12/13/2016	0.59	5.88	0.08	0.14	0.02	0.16	0.07	0.00
12/15/2016	0.66	8.90	0.14	0.13	0.03	0.36	0.18	0.00
12/17/2016	4.50	12.95	0.24	0.06	0.04	0.21	0.14	0.00
12/21/2016	0.15	1.36	0.02	0.04	0.00	0.07	0.03	0.00
12/23/2016	1.18	9.69	0.16	0.37	0.03	0.31	0.19	0.00
2/24/2017	0.13	2.00	0.01	0.09	0.01	0.07	0.01	0.00
2/26/2017	0.56	10.49	0.22	0.17	0.01	0.12	0.07	0.00
2/28/2017	0.64	10.60	0.21	0.39	0.04	0.29	0.10	0.00
3/2/2017	0.39	7.70	0.06	0.08	0.01	0.13	0.04	0.00
3/7/2017	0.81	13.82	0.12	0.23	0.04	0.58	0.14	0.00
7/31/2017	-9.38	4.29	0.07	-2.43	0.02	0.24	0.01	-422.15
8/2/2017	0.39	3.84	0.14	0.46	0.04	0.42	0.03	0.00
8/6/2017	0.23	0.73	0.03	0.11	0.00	0.01	0.00	0.00
8/8/2017	0.36	4.46	0.14	0.73	0.03	0.10	0.02	0.00
8/10/2017	0.21	6.82	0.12	0.70	0.01	0.06	0.01	0.00
8/12/2017	0.29	3.06	0.20	0.60	0.01	0.11	0.01	0.00
8/14/2017	-8.75	5.66	0.09	-2.57	0.01	0.29	0.03	-419.82
8/18/2017	0.55	3.87	0.10	0.50	0.02	0.35	0.03	0.00
8/20/2017	0.74	5.66	0.15	0.50	0.04	0.49	0.03	0.00
8/22/2017	0.54	5.43	0.11	0.73	0.04	0.41	0.02	0.00
8/24/2017	0.82	11.03	0.10	0.52	0.02	0.44	0.04	0.00
8/26/2017	1.04	10.23	0.16	0.51	0.03	0.58	0.04	0.00
8/29/2017	1.09	8.11	0.13	0.75	0.06	0.77	0.05	0.00

Figure B4: Table of $PM_{2.5}$ Soluble elements and total elements for each date during PRAPPE sampling

	Soluble Elements (ng m^{-3})							
Dates collected	**Pd**	**Ag**	**Cd**	**Sn**	**Sb**	**Cs**	**Ba**	**La**
NOV 2, 4, 5, 6 2017								
NOV 27, 29, 30, 31 2017								
12/11/2016								
12/13/2016	0.00	0.00	0.02	0.04	0.09	0.00	2.30	0.00
12/15/2016	0.00	0.00	0.02	0.02	0.17	0.00	3.36	0.00
12/17/2016	0.00	0.00	0.05	0.01	1.56	0.00	1.62	0.00
12/21/2016	0.00	0.00	0.00	0.01	0.04	0.00	0.87	0.00
12/23/2016	0.00	0.00	0.02	0.32	0.27	0.00	5.72	0.00
2/24/2017	0.00	0.00	0.01	0.07	0.03	0.00	0.55	0.00
2/26/2017	0.00	0.00	0.01	0.03	0.08	0.00	1.78	0.00
2/28/2017	0.00	0.00	0.02	0.07	0.16	0.00	2.96	0.00
3/2/2017	0.00	0.00	0.01	0.00	0.14	0.00	2.18	0.00
3/7/2017	0.00	0.00	0.03	0.04	0.23	0.00	4.41	0.00
7/31/2017	0.81	-24.96	-1.58	0.08	-17.49	-106.74	1.45	0.00
8/2/2017	-1.69	0.00	0.02	0.21	0.10	0.00	2.19	0.01
8/6/2017	-2.61	0.00	0.00	0.01	0.01	0.00	0.13	0.00
8/8/2017	0.74	0.00	0.03	0.11	0.11	0.00	1.35	0.00
8/10/2017	-4.68	-0.01	0.00	0.00	0.05	0.00	1.11	0.00
8/12/2017	-1.91	0.00	0.02	0.18	0.08	0.00	0.78	0.00
8/14/2017	1.56	-29.10	-0.26	0.18	-17.25	-106.15	3.26	0.00
8/18/2017	-1.73	0.00	0.02	0.22	0.11	0.00	2.54	0.00
8/20/2017	-0.92	0.00	0.03	0.26	0.18	0.00	2.45	0.00
8/22/2017	0.69	0.00	0.02	0.05	0.11	0.00	2.11	0.01
8/24/2017	-2.75	0.00	0.01	0.89	0.18	0.00	3.53	0.00
8/26/2017	-2.27	0.00	0.02	0.22	0.19	0.01	3.86	0.00
8/29/2017	-2.33	0.00	0.03	0.56	0.32	0.00	4.49	0.01

Figure B5: Table of $PM_{2.5}$ Soluble elements and total elements for each date during PRAPPE sampling

	Soluble Elements (ng m^{-3})							
Dates collected	**Ce**	**Nd**	**Sm**	**Pt**	**Tl**	**Pb**	**Th**	**U**
NOV 2, 4, 5, 6 2017								
NOV 27, 29, 30, 31 2017								
12/11/2016								
12/13/2016	0.00		0.00	0.00	0.02	0.15	0.00	0.00
12/15/2016	0.00		0.00	0.00	0.01	0.08	0.00	0.00
12/17/2016	0.00		0.00	0.00	0.01	0.30	0.00	0.00
12/21/2016	0.00		0.00	0.00	0.00	0.00	0.00	0.00
12/23/2016	0.00		0.00	0.00	0.00	0.08	0.00	0.00
2/24/2017	0.00		0.00	0.00	0.00	0.02	0.00	0.00
2/26/2017	0.00		0.00	0.00	0.00	0.10	0.00	0.00
2/28/2017	0.00		0.00	0.00	0.00	0.14	0.00	0.00
3/2/2017	0.00		0.00	0.00	0.00	0.01	0.00	0.00
3/7/2017	0.00		0.00	0.00	0.00	0.03	0.00	0.00
7/31/2017	0.01	-1.20	0.00	0.00	0.01	0.06	0.00	0.00
8/2/2017	0.02	0.01	0.00	0.00	-0.01	0.09	0.00	-0.07
8/6/2017	0.00	0.00	0.00	0.00	-0.01	0.00	0.00	-0.13
8/8/2017	0.00	0.00	0.00	0.00	-0.01	0.16	0.00	-0.05
8/10/2017	0.00	0.00	0.00	0.00	-0.03	0.04	0.00	-0.27
8/12/2017	0.00	0.00	0.00	0.00	-0.01	0.15	0.00	-0.09
8/14/2017	0.00	-1.19	0.00	0.00	0.01	0.04	0.00	0.00
8/18/2017	0.01	0.00	0.00	0.00	-0.01	0.05	0.00	-0.12
8/20/2017	0.01	0.00	0.00	0.00	-0.01	0.07	0.00	-0.12
8/22/2017	0.02	0.01	0.00	0.00	-0.01	0.14	0.00	-0.13
8/24/2017	0.01	0.00	0.00	0.00	-0.01	0.08	0.00	-0.13
8/26/2017	0.01	0.01	0.00	0.00	-0.01	0.06	0.00	-0.12
8/29/2017	0.02	0.01	0.00	0.00	-0.01	0.11	0.01	-0.13

Figure B6: Table of $PM_{2.5}$ Soluble elements and total elements for each date during PRAPPE sampling

	Total Elements (ng m^{-3})						
Dates collected	**Na**	**Mg**	**Al**	**K**	**Ca**	**Sc**	**Ti**
NOV 2, 4, 5, 6 2017	18.48	7.99	51.11	41.84	46.49	0.01	2.68
NOV 27, 29, 30, 31 2017	36.98	22.75	145.62	91.61	101.52	0.02	6.42
12/11/2016	1.59	1.83	7.78	4.36	0.00	0.01	0.33
12/13/2016	23.27	11.01	14.77	17.46	12.26	0.00	1.30
12/15/2016	26.77	8.44	54.25	56.62	29.25	0.01	3.98
12/17/2016	14.82	6.25	13.96	21.41	7.22	0.00	0.85
12/21/2016	51.30	12.83	30.50	27.16	23.39	0.01	2.24
12/23/2016	58.33	18.08	38.36	62.79	25.69	0.01	3.14
2/24/2017	4.41	3.65	16.10	11.05	6.61	0.00	0.89
2/26/2017	12.79	5.42	12.53	29.84	6.68	0.00	1.03
2/28/2017	19.61	9.72	31.85	48.65	17.66	0.00	1.77
3/2/2017	2.85	1.52	2.98	4.93	0.50	0.02	0.52
3/7/2017	40.25	26.10	110.45	103.91	57.47	0.02	5.98
7/31/2017	29.84	8.23	50.01	40.57	26.26	0.01	3.03
8/2/2017	14.89	7.50	38.45	33.19	30.62	0.01	2.49
8/6/2017	18.79	6.77	20.77	48.85	24.87	0.01	1.11
8/8/2017	7.70	3.61	13.92	50.67	23.08	0.00	0.92
8/10/2017	3.60	3.24	11.91	17.58	45.46	0.01	0.74
8/12/2017	12.34	4.26	18.74	22.55	17.84	0.01	1.35
8/14/2017	35.93	11.44	50.53	46.82	48.26	0.01	3.65
8/18/2017	38.01	13.56	73.36	66.97	58.56	0.02	5.13
8/20/2017	34.74	21.37	108.70	74.23	66.88	0.02	5.03
8/22/2017	35.82	21.73	123.52	83.86	59.72	0.02	5.43
8/24/2017	28.76	15.01	91.59	53.49	47.15	0.02	5.18
8/26/2017	13.82	3.43	7.35	14.98	20.60	0.00	0.66
8/29/2017	59.56	39.24	220.87	145.93	118.64	0.04	10.21

Figure B7: Table of $PM_{2.5}$ Soluble elements and total elements for each date during PRAPPE sampling

	Total Elements (ng m^{-3})							
Dates collected	**V**	**Cr**	**Mn**	**Fe**	**Co**	**Ni**	**Cu**	**Zn**
NOV 2, 4, 5, 6 2017	0.11	0.14	1.33	66.42	0.02	0.07	0.94	5.34
NOV 27, 29, 30, 31 2017	0.22	0.31	2.70	145.02	0.04	0.14	4.56	7.86
12/11/2016	0.00	0.16	0.21	10.05	0.00	0.01	2.89	3.23
12/13/2016	0.01	0.26	0.74	44.16	0.01	0.10	0.95	4.95
12/15/2016	0.07	0.24	1.74	78.04	0.02	0.09	1.35	8.92
12/17/2016	0.00	0.07	0.38	9.62	0.01	0.04	2.27	7.06
12/21/2016	0.03	0.27	1.15	72.94	0.02	0.07	1.61	12.67
12/23/2016	0.05	0.44	1.94	106.69	0.02	0.18	3.84	14.77
2/24/2017	0.00	0.06	0.37	16.14	0.00	0.06	0.30	1.68
2/26/2017	0.00	0.15	0.46	33.42	0.01	0.02	0.89	6.84
2/28/2017	0.03	0.18	1.17	59.19	0.01	0.06	1.19	7.54
3/2/2017	0.00	0.04	0.19	15.49	0.00	0.00	0.36	1.54
3/7/2017	0.14	0.57	2.62	131.88	0.03	0.13	2.20	10.91
7/31/2017	0.04	0.17	0.99	49.72	0.02	0.05	0.46	2.18
8/2/2017	0.06	0.12	0.92	41.41	0.02	0.04	0.29	1.30
8/6/2017	0.00	0.08	0.65	27.04	0.01	-0.01	0.46	4.85
8/8/2017	0.00	0.09	0.69	26.13	0.01	0.00	0.50	3.46
8/10/2017	0.00	0.08	0.37	18.55	0.01	0.09	0.24	3.54
8/12/2017	0.01	0.09	0.51	25.08	0.01	0.01	0.39	1.94
8/14/2017	0.10	0.30	1.46	96.78	0.02	0.11	1.85	6.63
8/18/2017	0.11	0.23	1.80	92.27	0.03	0.05	1.05	4.60
8/20/2017	0.12	0.24	1.75	89.90	0.02	1.21	1.23	4.15
8/22/2017	0.14	0.22	1.79	90.37	0.02	0.07	0.77	3.81
8/24/2017	0.13	0.26	2.04	107.41	0.03	0.07	1.26	3.89
8/26/2017	0.00	0.02	0.19	6.33	0.00	0.02	0.13	0.93
8/29/2017	0.26	0.34	3.30	165.61	0.05	0.11	1.50	5.62

Figure B8: Table of $PM_{2.5}$ Soluble elements and total elements for each date during PRAPPE sampling

	Total Elements (ng m^{-3})							
Dates collected	**As**	**Se**	**Rb**	**Sr**	**Mo**	**Rh**	**Pd**	**Ag**
NOV 2, 4, 5, 6 2017	0.15	0.36	0.13	0.57	0.07	0.00	0.26	0.00
NOV 27, 29, 30, 31 2017	0.15	0.18	0.31	1.33	0.14	0.00	0.25	0.00
12/11/2016	0.06	0.18	0.01	0.03	0.06	0.00	0.00	0.00
12/13/2016	0.09	0.18	0.04	0.19	0.11	0.00	0.00	0.00
12/15/2016	0.18	0.30	0.16	0.49	0.24	0.00	0.00	0.00
12/17/2016	0.19	0.12	0.03	0.14	0.12	0.00	0.00	0.00
12/21/2016	0.09	0.24	0.08	0.34	0.17	0.00	0.00	0.00
12/23/2016	0.25	0.54	0.10	0.53	0.36	0.00	0.00	0.01
2/24/2017	0.02	0.17	0.04	0.08	0.02	0.00	0.00	0.00
2/26/2017	0.30	0.35	0.05	0.14	0.11	0.00	0.00	0.00
2/28/2017	0.24	0.50	0.10	0.28	0.14	0.00	0.00	0.00
3/2/2017	0.04	0.11	0.01	0.04	0.03	0.00	0.00	0.00
3/7/2017	0.15	0.42	0.27	0.82	0.22	0.00	0.00	0.00
7/31/2017	0.09	0.63	0.12	0.36	0.03	0.00	0.07	0.00
8/2/2017	0.09	0.28	0.10	0.32	0.01	0.00	0.01	0.00
8/6/2017	0.27	1.20	0.07	0.20	0.01	0.00	0.20	0.01
8/8/2017	0.16	0.95	0.05	0.15	0.02	0.00	0.13	0.01
8/10/2017	0.13	0.88	0.04	0.11	-0.02	0.00	0.95	0.01
8/12/2017	0.26	0.87	0.05	0.15	0.00	0.00	0.11	0.01
8/14/2017	0.23	0.78	0.13	0.54	0.10	0.00	1.57	0.01
8/18/2017	0.18	0.93	0.21	0.57	0.08	0.00	0.44	0.01
8/20/2017	0.26	0.87	0.24	0.67	0.05	0.00	-0.01	0.14
8/22/2017	0.18	0.99	0.24	0.60	0.03	0.00	0.20	0.01
8/24/2017	0.13	0.80	0.20	0.61	0.06	0.00	0.15	0.01
8/26/2017	0.20	0.42	0.02	0.08	-0.01	0.00	0.53	0.01
8/29/2017	0.19	0.88	0.49	1.11	0.08	0.00	0.15	0.01

Figure B9: Table of $PM_{2.5}$ Soluble elements and total elements for each date during PRAPPE sampling

	Total Elements (ng m^{-3})							
Dates collected	**Cd**	**Sn**	**Sb**	**Cs**	**Ba**	**La**	**Ce**	**Nd**
NOV 2, 4, 5, 6 2017	0.02	0.44	0.20	0.00	2.20	0.05	0.07	0.02
NOV 27, 29, 30, 31 2017	0.03	0.40	0.37	0.01	6.87	0.18	0.25	0.09
12/11/2016	0.01	0.31	0.07	0.00	0.56	0.01	0.01	
12/13/2016	0.02	0.63	0.20	0.00	2.96	0.02	0.06	
12/15/2016	0.03	0.20	0.31	0.01	4.15	0.07	0.11	
12/17/2016	0.04	0.06	0.60	0.00	1.02	0.02	0.02	
12/21/2016	0.01	0.51	0.29	0.00	4.68	0.16	0.11	
12/23/2016	0.05	4.17	0.73	0.00	9.88	0.37	0.16	
2/24/2017	0.01	0.77	0.05	0.00	0.78	0.01	0.02	
2/26/2017	0.02	0.53	0.16	0.00	2.54	0.04	0.03	
2/28/2017	0.02	0.87	0.27	0.00	2.84	0.04	0.06	
3/2/2017	0.00	0.09	0.09	0.00	0.96	0.00	0.01	
3/7/2017	0.05	0.71	0.53	0.01	6.97	0.16	0.21	
7/31/2017	0.00	0.35	0.09	0.01	2.08	0.05	0.08	0.03
8/2/2017	0.01	0.38	0.05	0.00	1.49	0.03	0.07	0.03
8/6/2017	0.03	1.27	0.13	0.00	1.51	0.02	0.04	0.01
8/8/2017	0.03	0.33	0.13	0.00	1.47	0.04	0.03	0.01
8/10/2017	0.01	0.03	0.03	0.00	0.89	0.01	0.02	0.01
8/12/2017	0.02	0.72	0.11	0.00	0.98	0.02	0.03	0.01
8/14/2017	0.03	1.58	0.53	0.01	6.30	0.10	0.11	0.03
8/18/2017	0.04	1.55	0.23	0.01	4.32	0.06	0.13	0.04
8/20/2017	0.05	1.84	0.35	0.01	4.50	0.14	0.17	0.07
8/22/2017	0.03	0.25	0.16	0.01	3.50	0.10	0.17	0.07
8/24/2017	0.02	4.56	0.29	0.01	4.90	0.10	0.17	0.06
8/26/2017	0.01	0.10	0.01	0.00	0.21	0.01	0.01	0.00
8/29/2017	0.04	1.89	0.63	0.02	7.43	0.22	0.36	0.14

Figure B10: Table of $PM_{2.5}$ Soluble elements and total elements for each date during PRAPPE sampling

	Total Elements (ng m^{-3})					
Dates collected	**Sm**	**Pt**	**Tl**	**Pb**	**Th**	**U**
NOV 2, 4, 5, 6 2017	0.00	0.00	0.00	0.32	0.01	0.01
NOV 27, 29, 30, 31 2017	0.02	0.00	0.00	0.48	0.03	0.01
12/11/2016	0.00	0.00	0.02	0.19	0.00	0.00
12/13/2016	0.00	0.00	0.01	0.47	0.00	0.00
12/15/2016	0.01	0.00	0.00	0.51	0.01	0.01
12/17/2016	0.00	0.00	0.00	0.59	0.00	0.00
12/21/2016	0.00	0.00	0.00	0.49	0.01	0.00
12/23/2016	0.00	0.00	0.00	1.28	0.01	0.00
2/24/2017	0.00	0.00	0.00	0.06	0.00	0.00
2/26/2017	0.00	0.00	0.00	0.34	0.00	0.00
2/28/2017	0.00	0.00	0.00	0.60	0.01	0.00
3/2/2017	0.00	0.00	0.00	0.02	0.00	0.00
3/7/2017	0.01	0.00	0.00	0.65	0.03	0.01
7/31/2017	0.01	0.00	-0.01	0.20	0.01	0.01
8/2/2017	0.00	0.00	-0.01	0.14	0.01	0.01
8/6/2017	0.00	0.00	-0.01	0.42	0.00	0.01
8/8/2017	0.00	0.00	-0.01	0.28	0.00	0.01
8/10/2017	0.00	0.00	-0.02	0.07	0.00	0.01
8/12/2017	0.00	0.00	-0.01	0.29	0.00	0.01
8/14/2017	0.01	0.00	-0.01	0.47	0.01	0.01
8/18/2017	0.01	0.00	0.01	0.41	0.02	0.02
8/20/2017	0.01	0.00	0.00	0.49	0.03	0.01
8/22/2017	0.01	0.00	-0.01	0.49	0.03	0.01
8/24/2017	0.01	0.00	-0.01	0.35	0.02	0.09
8/26/2017	0.00	0.00	-0.01	0.06	0.00	0.01
8/29/2017	0.03	0.00	-0.01	0.57	0.06	0.02